Sensing Methods for Soft Robotics

by

Wyatt Felt

A dissertation submitted in partial fulfillment
of the requirements for the degree of
Doctor of Philosophy
(Mechanical Engineering)
in The University of Michigan
2017

Doctoral Committee:

Assistant Professor C. David Remy, Chair
Professor Diann Brei
Professor Sridhar Kota
Associate Professor Heath Hofmann

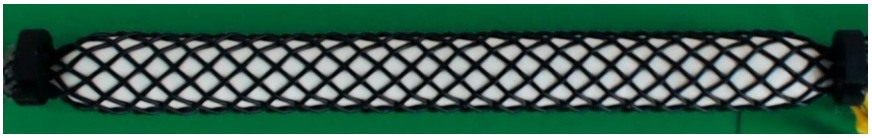

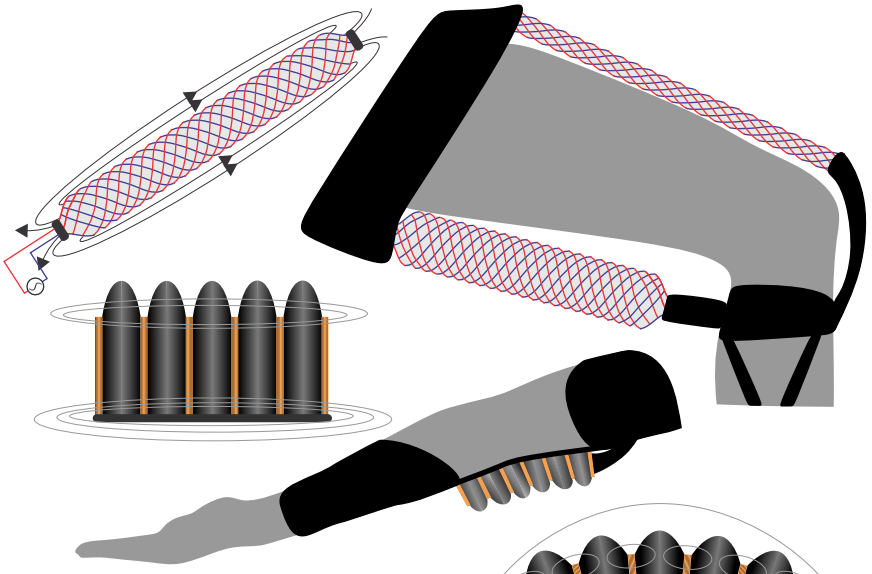

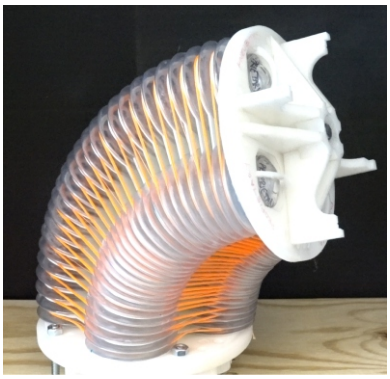

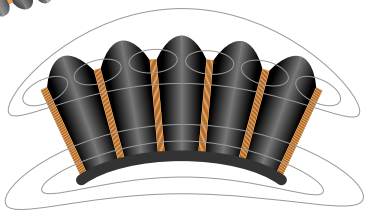

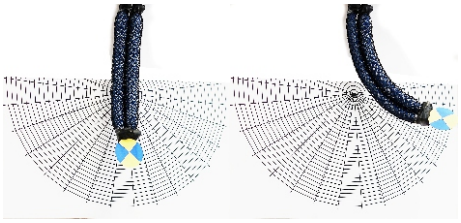

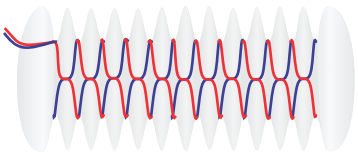

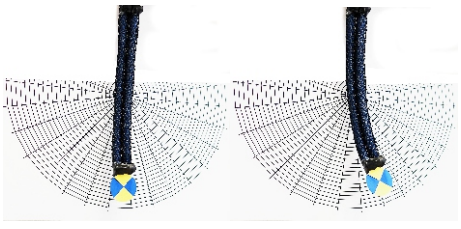

Wyatt Felt

wfelt@umich.edu

ORCID iD: 0000-0003-3968-1889

For Nephi, the builder

ACKNOWLEDGEMENTS

Thanks go to my advisor and mentor Prof. C. David Remy for taking a chance on a quirky kid with weird ideas. Thanks for your keen insight, your skeptical thinking, and the many, many hours of support that you provided for this work.

Thanks to my wife, Rebecca, for her wisdom and her immeasurable support.

Thanks to my undergraduate assistants Khai Yi Chin, Kevin Green, Michelle Suen and Juliet Lawton.

Thanks to Joshua Bishop-Moser and Daniel Bruder for their thoughtful reviews of the FREE kinematic model and Audrey Sedal for helping me understand constitutive models for FREEs.

Thanks to my collaborators at Pneubotics who guided, assisted in, and provided material support to the bellows work: Maria Telleria, Thomas F. Allen, Gabriel Hein, Jonathan B. Pompa, Kevin Albert and Henry Tonoyan.

Thanks to the National Science Foundation who supported me in this work with a Graduate Research Fellowship.

This work is based on the following peer-reviewed publications [1]–[7]. Some passages of these sources have been quoted verbatim in this work. The technology described in this dissertation is the subject of a pending patent application [8].

Funding for this project was provided by NIH (GRANT: 1-R01-EB019834-2014 Wearable eMbots to Induce Recovery of Function).

Toyota Research Institute ("TRI") provided funds to assist the authors with their research but this article solely reflects the opinions and conclusions of its authors and not TRI or any other Toyota entity.

This material is based upon work supported by the National Science Foundation Graduate Research Fellowship under Grant No. DGE 1256260. Any opinion, findings, and conclusions or recommendations expressed in this material are those of the author(s) and do not necessarily reflect the views of the National Science Foundation.

TABLE OF CONTENTS

LIST OF FIGURES

Figure

LIST OF TABLES

Table

ABSTRACT

Soft robots exhibit complex behaviors that emerge from deliberate compliance in the actuators and structure. This compliance allows soft robots to passively conform to the constraints of their environment and to the objects they are manipulating. Many soft robots are actuated by the flexible expansion of hermetically sealed volumes. Systems based on these principles are lightweight, flexible and have low reflected inertia. This makes them inherently safe in physical human robot interaction. Moreover, the sealed actuators and flexible joints are well-suited to work in harsh environments where external contaminates could breach the dynamic seals of rotating or sliding shafts.

Accurate motion control remains a highly challenging task for soft robotic systems. Precise models of the actuation dynamics and environmental interactions are often unavailable. This renders open-loop control impossible, while closed-loop control suffers from a lack of suitable feedback. Conventional motion sensors, such as linear or rotary encoders, are difficult to adapt to robots that lack discrete mechanical joints. The rigid nature of these sensors runs contrary to the aspirational benefits of soft systems. Other proposed soft sensor solutions are still in their infancy and have only recently been used for motion-control of soft robots.

This dissertation explores the design and use of inductance-based sensors for the estimation and control of soft robotic systems. These sensors are low-cost, lightweight, easy-to-fabricate and well-suited for the conditions that soft systems can best exploit. The inquiry of this dissertation is conducted both theoretically and experimentally for Fiber-Reinforced Elastomeric Enclosures (including McKibben muscles) and bellows

actuators. The sensing of each actuator type is explored through models, design analyses and experimental evaluations. The results demonstrate that inductance-based sensing is a promising technology for these otherwise difficult-to-measure actuators. By combining sensing and actuation into a single component, the ideas presented in this work provide a simple, compact and lightweight way to create and control motion in soft robotic systems. This will enable soft systems that can interactively engage with their environment and their human counterparts.

CHAPTER I

Introduction

1.1 Motivation

Despite the animal-like intelligence of robots today, most robots are anything but animal-like. As a society, we have created machines to perform tasks that would be impossible, difficult or tedious for humans. Traveling at great speeds or handling immense materials requires machines that are distinctly different than us. We need machines to generate and withstand high forces. We need tireless factory machines that move rapidly and precisely. These machines are the foundation of traditional robotics. Robots like these can be controlled to create accurate and repeatable motion. This predictability is valuable when the environment is equally predictable. A robot welding car frames, for example, depends on precise information about the location of the frame. This same robot, however, could cause serious damage if its surroundings did not match its internal maps.

In a sense, the environment of the robot must mirror the same "rigidity" that the robot possesses–a well-defined, consistent and measurable shape. These hard and unyielding machines stand in stark contrast to the "soft" nature of biological systems. Biological systems thrive in diverse and varied environments, but traditional robots depend on uniform and predictable surroundings. For robots to thrive in biological environments, we need a new paradigm for robot design and control.

Just as rigid robots thrive in "rigid" environments, soft robots excel in "soft" environments. Compared to traditional robots, the structure of soft robots is much closer to that of biology. Soft robots are designed with deliberate compliance that allows them to passively conform to external constraints. This allows soft robots to mimic some of the "embodied intelligence" exhibited by animals and bypass much of the complex reasoning required in traditional robots.

The passive compliance of soft robots can be contrasted to the intense sensing and central planning in traditional robotics. Rather than planning immutable actions with a purportedly perfect map of the world, soft robots allow the world to shape their behavior. For example, to pick up a tomato, a traditional robot end-effector would anticipate the exact shape and size of the tomato, whereas a soft end-effector could conform to the tomato as it grasped [9]. To provide movement assistance to the human body, a traditional robot might use rigid links where a soft robot would use a flexible, garment-like structure [10], [11]. In some sense, the body of the soft robot has the desired behavior "encoded" in its structural properties. This "morphological computation" allows soft robots to perform tasks in unknown environments without the intensity of sensing and processing required of a traditional robot [12]. The compliant nature of soft robots makes them a valuable tool for exploration and manipulation in natural environments as well as human-robot interaction.

Compared to traditional robots, soft robots represent a fundamentally different kind of machine. Soft robots can be built from lightweight and flexible materials. This makes soft robots much more resilient to the shock of physical impacts than heavy, traditional robots. This resilience comes in part from the distributed stress and increased contact time that a soft body provides [13]. When a collision occurs, soft robots can passively deform and absorb collision energy [14]. Moreover, soft systems can have significantly lower reflected inertia, making them safe for operation alongside humans [15].

On their own, soft robots can perform tasks that traditional robots would find all but impossible. For instance, soft robotic end-effectors can handle delicate materials and difficult-to-grasp materials that that have typically been reserved for humans. Robotics Business Review designated an emerging, soft robot gripper as a "game-changer" for the industry [16]. Outside of the factory, these grippers could be used, for example, to harvest delicate produce [9] or sea life [17] that would be damaged by traditional end-effectors.

Soft robotic mechanisms can operate without rigid frames or sliding surfaces. This makes them useful in harsh environments where external contaminates could breach the dynamic seals of rotating or sliding shafts. For example, in desert environments where sand would clog and wear traditional bearings, soft mechanisms can move without concern. These soft mechanisms could also be used on survey robots or solar positioners [18].

The fundamental differences between soft and rigid robots pose both opportunities and challenges. On the one hand, soft robots can perform tasks that would be all-but-impossible for the best rigid robots of today. On the other hand, nearly all the science of robotics has focused on robots with kinematic chains of rigid links [19]. The field of soft robotics has recently seen a great deal of growth across the globe. The European Commission has funded the OCTOPUS [20], RoboSoft [21] and Soft Manipulation (SoMa) [22] projects. The Wyss Institute of Harvard University has created the "Soft Robotics Toolkit" to collect and distribute expertise [23]. Companies like Soft Robotics Inc. [9] and Otherlab [24] are working to exploit commercial applications for this developing technology. Despite this growth and interest, major challenges remain. The actuators, sensors, modeling and control techniques of soft robotics all lag significantly behind traditional robotics.

One of the most difficult challenges in soft robotics is the inability to either predict or sense the motion of soft robots. This constraint imposes limits on the applications

of these systems. Without the ability to sense their own motion, soft robots are often limited to open-loop control sequences [25]–[27] or manual teleoperation [28]. This is apparent in the rules of the 2016 "Soft Robotics Grand Challenge." All of the tasks in the challenge permited robot operators to directly observe and remotely control their robots [29].

One would hope that, with sufficiently sophisticated models, soft robots could be controlled in an open-loop fashion. Unfortunately, the models for predicting soft robot motion are often quite complex and may only be accurate for a small portion of the working envelope [19], [30]. Even if the models were improved, they rely on knowledge of external forces and constraints. Without information about these external effects, the models cannot predict the robot motion. For example, a continuum manipulator can only move predictably when the forces on it are known and constant (e.g. gravity). Once the manipulator grasps an object of unknown weight, the state of the manipulator cannot be accurately modeled. Given the unknown, environmental constraints that can be imposed on soft robotic systems, closed-loop controllers are required to drive their motion [14].

For closed-loop control to be a viable option, the motion of the robot must be measured. Unfortunately, the nature of soft robots makes their motion difficult to measure with traditional sensors [14]. Like traditional robot actuators, traditional sensors are designed to work with discrete mechanical joints. This makes traditional sensors poorly suited to work with the deformable structures found in soft robotics. An ideal soft robotic sensing system would be flexible, lightweight and would not constrain the robot motion in undesired ways.

1.2 State of the Art

Traditional robots rely on discrete mechanical joints. These joints are typically attached to rigid members and driven by stiff, non-back-drivable actuators. This rigid

structure allows the kinematics of the robot to be easily modeled, sensed and controlled. Unfortunately, the rigidity also makes the robots cumbersome and vulnerable to impacts.

One of the first ways that robots were "softened" was by lowering the mechanical impedance of the actuated joints. One technique for softening stiff actuators such as hydraulic cylinders and geared electric motors is the use of series elastic elements. By placing a spring between the actuator and the world, these Series Elastic Actuators more easily conform to constraints imposed by the world [31]. It is no coincidence that the researchers who invented this technique, Gill Pratt and Matt Williamson, were working on legged robots [32]. They needed a system that could generate stable forces and withstand the impacts imposed by rapid locomotion.

While Series Elastic Actuators provide a popular way to soften traditional robots (the original paper [31] has over 1400 citations), the overall robot structure is still rigid. Robots using this technology rely on machined, metal components and precision encoders. The motion of these robots is limited by the constraints of the mechanical joints. The forces created by the joints can conform to external constraints, but the motion of the robot is still rigidly defined by its joints. Soft robots conform to the environment by removing discrete joints entirely.

The versatility of a traditional robot is often quantified by the number of its degrees of freedom. In general, this number can be increased by increasing the number of joints on the robot [30]. Additional joints, however, add cost and complexity to robots. Soft robots, made from elastomeric structures, can exhibit infinite degrees of freedom. The flexibility of these robots allows their kinematics to conform to their environment without the mechanical complexity of numerous discrete joints.

The flexible structures of soft robots may open up degrees of freedom, but they require nontraditional actuation strategies. Traditional actuators are designed to work with discrete mechanical joints. Soft robots often use tendons, electroactive polymers,

shape-memory alloys or fluids to actuate [30]. Even as other technologies develop, fluids have remained a popular choice [33]. Fluids are easy to embed within elastomers and flow naturally when exposed to external constraints. Soft fluidic actuators include bellows [34], [35], fiber-reinforced structures [36]–[38], balloon-like actuators [39], and actuators reinforced by constant-surface-area (fabric-like) structures [15], [40].

Given the value that self-sensing soft actuators would create, a great deal of effort has been focused on developing technologies that could be used to this end. The following material reviews strategies proposed for sensing the displacement of soft, fluidic actuators and systems. These include external localization strategies, inertial measurement, rigid internal sensors and soft sensing technologies. A brief overview of inductance sensing and published proposals to use inductance sensing in soft, fluid systems is also given.

1.2.1 External Localization

External localization systems include visual localization, electromagnetic tracking, and radio frequency indoor positioning systems. Camera-based 3D motion capture has been used to provide feedback for continuum manipulators [41], [42] and an inflatable humanoid [43]. Many orthosis and exoskeletons driven by soft fluid actuators rely on camera-based motion capture technology for position tracking [44]–[47]. These systems track the positions of retro-reflective markers with sets of cameras in known locations surrounding the robot or device. Popular implementations of this technology are available from companies such as Vicon (Oxford, UK) and Optitrack (Corvallis, OR, USA). The marker identification relies on special lighting conditions. The cameras typically provide timed light pulses emanating from around the lens area. The markers reflect this light back towards the sources. Because the cameras typically assume that any reflection of the timed light signal is a marker, other reflective objects have to be removed from the workspace or covered. Each marker needs to be

identified by at least two calibrated cameras for the marker position in 3D space to be estimated. To estimate the position and orientation of a rigid body, three markers (each seen by at least two cameras) are needed. This method is popular because many markers can be tracked simultaneously by the same set of cameras.

Laser beacons can also be used [48], [49]. These beacons create a structured field of light that allows photo-receivers on a rigid body to calculate their position relative to the beacons. A popular implementation of this technology tracks the headset and hand controllers in the virtual reality platform *HTC Vive* (HTC, Taoyuan City, Taiwan). Like 3D motion capture systems, laser beacon systems require a line-of-sight in order to operate. Accordingly, they have limited utility in a visually occluded workspace.

Electromagnetic tracking systems avoid the occlusion problems of the vision-based systems. These sensors work by placing electromagnetic (EM) sensors placed in an externally created field. The sensors consist of small sets of coils that are magnetically coupled to the external beacon coil. By connecting the individual sensors to a processing box, the location and orientation of each sensor can be estimated. These EM trackers have been used in feedback control [50], [51] of soft robotic devices. Popular implementations of this technology are found in the *Aurora* and *trakSTAR* systems (Ascension Technology Corp, Shelburne, VT, USA).

Another proposed technology is Radio Frequency Indoor Positioning. These systems can have vast workspaces but limited accuracy [52]. Systems have been proposed using Radio-Frequency Identification Tags, wireless networking signals, and Bluetooth [53].

External localization technologies all rely on fixed networks of reference points that predefine the workspace. In closed, laboratory-like environments, systems such as these may be useful. On the other hand, for mobile robots and human-assistive devices, a finite, predefined workspace is a serious limitation.

1.2.2 Inertial Measurement

Inertial Measurement Units (IMUs) provide another option for tracking robot motion [54], [55]. IMUs rely on the fusion of measurements from gyroscopes, accelerometers and a magnetometer to estimate the orientation of the sensor. By comparing values from multiple IMUs distributed along the robot, the relative orientations can be estimated. Orientation estimates from IMUs, however, are not always accurate. The accelerometers are very sensitive to vibration and acceleration. The heading of an IMU can change without changing the measured gravity vector. Without a change in the measured gravity vector, the heading can only be estimated from drift-prone angular velocity estimates or from measurements of the earth's magnetic field. The local magnetic field, however, is often locally distorted by large metal objects and electric motors [56], [57]. Without reliable magnetic field information, IMUs are susceptible to drift in their heading estimates.

1.2.3 Rigid Internal Sensors

1.2.3.1 Coupling to Rigid Linkages

There are numerous ways to utilize rigid sensors to track the movement of soft actuators. The most common method is to constrain the motion of the soft actuator to a rigid kinematic linkage [58]–[62]. In this way, the joints of the linkage can be tracked with traditional rotary or sliding sensors. Doing so, however, fails to take advantage of soft actuators' principle strengths–they can be used without rigid linkages and precise alignments. Moreover, when devices interact with the human body, rigid linkages and bulky sensors are often undesirable.

1.2.3.2 Measuring Distance Between Actuator Ends

Some have proposed systems that measure the displacement between the end-pieces of the soft actuator. For instance, a microwave transducer could be placed at one of the actuator ends [63]. By measuring the phase of the reflected signal, the actuator length could be determined. Alternatively, an optical or ultrasound transmitter could be placed on one side of the actuator and a reflector or receiver could be placed on the other side [64]. The length of the actuator could then be determined by the signal attenuation or time of flight. Similarly, the diameter of a McKibben muscle can be measured through changes in photo-reflectance [65]. It appears, however, that these methods would be most effective when the actuator ends are aligned. Such alignment is not always guaranteed in soft robotic applications.

1.2.3.3 Measuring the Recoil of Strings

In tentacle-like continuum manipulators, the actuators often change their length to bend the tentacle [30]. In these cases, researchers have often relied on measuring the length of strings running alongside the actuators [66], [67]. These strings, however, introduce several problems. First, they are vulnerable to lateral pressure. If the strings bump against an external object, they may be deflected. This deflection changes the length of the string but does not necessarily change the length of the actuator. This can introduce a bias into the measurement of the actuator length. Second, the physical routing of the strings is problematic. The strings are often routed through small eyelets spaced along the length of the system. If particles enter these small holes, they can impinge on the motion of the string. These eyelets leave the string exposed to the outside world where they can wear away or be cut. Finally, and most importantly, measuring the length of the strings requires rigid, spring-loaded sensors. These sensors add weight and complexity to the system. The physical bulk of the sensors limits the number of strings that can be used. For example, in the

OctArm continuum manipulator, the string recoil systems completely surround the base of the manipulator [66]. By all appearances, it would be difficult to adapt the system to include more strings.

1.2.3.4 Measuring Flow Into and Out of Actuator

Another method to measure the motion of a soft, fluid-powered actuator is to measure its volume. This could be done, for example, with a flow-meter measuring the flow into and out of the actuator. Alternatively, the flow into and out of a volume that contains the actuator could be used [68]. These methods would likely be more accurate when used with incompressible fluids such as water. It is possible that this method could result in a drift in the position estimate. This is because flow is essentially a measure of the change in actuator volume. This change in volume would need to be integrated to produce an estimate of the current volume.

1.2.4 Curvature Sensors

The motion of some soft robots corresponds to the bending of inextensible portions such as a flexible "spine." In such systems, curvature sensors could be used. These sensors exist in many varieties [69]. For example, optical fibers with Fiber Bragg Gratings, for example, can register curvature via changes in the fiber strain [70]. The strain changes the spacing of the gratings and the corresponding reflected wavelength. These sensors have been used for feedback control of a continuum manipulator [71]. The optical fibers provide curvature sensing in a very small package. Other systems rely on changes in transmitted light [72], [73], the proximity of an external magnet [74] or piezo-electric effects [75] to measure changes in curvature. Commercially-available curvature sensors have been integrated into the "fingers" of soft end-effectors [76]. A helical-tape of LED/phototransistor pairs can be used to create a "cable-like shape-sensor" that can estimate the shape of a long snake-like sensing-cable [77]. This

commercially available sensor was used in the Festo "BionicMotionRobot", a soft trunk-like manipulator driven by bellows [78]. For this robot, Festo reports a motion repetition accuracy of $\pm 10\,\text{mm}$ (with a $850\,\text{mm}$ trunk-length).

1.2.5 Soft Deformation Sensors

Many different technologies have been proposed to create inherently soft sensors. These soft sensors are typically rely on elastomers that change properties under strain. It is conceivable that these elastomeric sensors could be embedded into the structure of a soft fluidic actuator. The elastomeric sensors could be used, for example, in a rubber bladder surrounding the pressurized fluid [79], [80]. They could be used in a sheath that surrounds the actuator [81] or a ring that measures the diameter of the actuator at a certain point [82], [83]. A stretchable elastomeric sensor could also be used inside the actuator to sense the distance between the end-pieces [84].

1.2.5.1 Optical

The attenuation of transmitted light in optical conduits can be used to measure the deformation of soft devices. For instance, optical fibers can be pre-bent into a structure that couples structure length to the radius of the fiber bends. By measuring the bend-induced attenuation in the fibers, the length can be estimated [73]. Other optical techniques rely on stretchable elastomeric light conduits. These conduits cause a greater portion of the light to be lost when they are strained [85]. Stretchable conduits such as these have been used in a soft, hand-like end-effector [86].

One disadvantage of these sensors is that the measurement signal is sensitive to multiple modes of deformation [86]: bending, elongation and lateral pressure. Thus, with only one sensor measurement, assumptions must be made about which effect (or combination of effects) is causing the change in the signal.

1.2.5.2 Resistance-Based

One way to create an elastomeric transducer is to use strain to create changes in the resistance of an embedded conductive structure. These structures can be formed by adding carbon to an elastomer [87]–[89]. The pattern of the conductive elastomer can be optimized to align the sensitivity of the sensor with the direction of the strain of interest [90], [91]. Such sensors, however, have non-linear behaviors that limit their usefulness. Wang and Ding, for example, report that resistance of their elastomer required nearly 100 seconds to achieve steady-state after strain [92]. This time sensitive response is due to stress relaxation in the elastomer and can cause other effects. For example, the resistance may spike at the onset of a step change in strain and show hysteresis under cyclic strain [91], [93], [94]. For the sensor to be used during the time of transience, the time response needs to be taken into account [88]. Conductive elastomers have been used in diameter sensors [83] and length sensors [80] for McKibben muscle actuators. Conductive yarns have also been used in McKibben muscles [95]. Coiled conductive nylon thread has been used to create sensors [96]. Carbon-nanotube-based sensors have been used to measure bending in bellows [97].

To avoid some of the issues of created by a chemical bond between the elastomer and the conductive element, conductive pastes [98] or liquid can be used. Microchannels of conductive fluid in elastomers can detect very small strains within the elastomer [99]. Similar ideas have been explored since as early as 1953 [100]. As the elastomer is strained, the geometry of the microchannels changes. For instance, a microchannel may become longer with a narrower cross section. This results in an increase in electrical resistance. A common liquid choice is Eutectic Gallium Indium, though ionic liquids may be used to boost the resistivity [101]. Park and Wood demonstrated that these sensors could be embedded in an elastomeric sheath over a soft fluid actuator [81]. Their sensor exhibited a large and approximately linear response to strain induced in the actuator over the course of its contraction. Others

have used similar sensors in soft, fluid-driven bending actuators [102], [103].

Some weaknesses of this method include: hysteresis, a limited operating temperature, and a sensitivity to strains induced by lateral pressures (unrelated to actuation). Recent work has proposed the use of "wavy channels" for the ionic liquid to eliminate problems of hysteresis and strain relaxation [104]. Temperature changes can be problematic. Park and Wood's actuator relied on the low-melting-point alloy Eutectic Gallium Indium [81] which solidifies at about 15 °C [105]. Though ionic (non-metallic) liquid sensors can flow over a wider range of temperatures, many ionic liquids exhibit large changes in conductivity with temperature. For instance, the conductivity of an ionic liquid may change 50-400 times from -15 °C to 120 °C [106]. The microchannel sensing technology has been used to create highly-sensitive tactile sensors [99]. The high sensitivity of these channels to small lateral pressures, however, can bias measurements of channel length. Recent work has proposed designs for which the sensitivity to lateral pressure is minimized [107].

1.2.5.3 Capacitance-Based

Another soft sensing technology is found in dielectric elastomers. These capacitor-like elastomeric structures use a thin sheet of elastomer to separate two compliant electrodes. Alternative techniques may rely on concentric tubes of conductive liquid [108] or a comb-like structure [109]. As the strain in the elastomer sheet changes its thickness, the capacitance between the electrodes changes correspondingly. Dielectric elastomer sensors have been used to sense the pressure and motion of soft actuators [79], [110]. It should be noted that, aside from sensing, dielectric elastomers can be used to both generate electricity [111], [112] and create active strain [113], [114]. As a sensor, however, dielectric elastomers are very sensitive to changes in temperature. Jean-Mistral et al. tested the dielectric constant of the most popular elastomer at a variety of temperatures [115]. At high excitation frequencies, they found that the

dielectric constant increased about 30 % over a temperature range of -40 °C to 100 °C. This 30 % change in the dielectric constant could bias the estimate of the capacitance by 30 %. For comparison, the strain-induced change in capacitance of a commercially available sensor is less than 60 % [116].

1.2.6 Inductance Overview

In this dissertation, the term "inductance" is used interchangeably with the more cumbersome "self-inductance." Self-inductance is a measure of magnetic flux imposed on a circuit by itself (per unit current). Self-inductance depends on the geometry of the circuit and on the proximity of nearby conductors and/or ferromagnetic materials. The inductance of a circuit resists changes in current. Dynamically, it has been compared to the inertia of mechanical systems.

The voltage across each element in an inductive circuit can be considered as an element of a vector $\boldsymbol{v}$. The relationship of the voltage vector $\boldsymbol{v}$ to the vector $\boldsymbol{i}$ of currents in each circuit element is given by

$$\boldsymbol{v} = \frac{d\mathbf{L}}{dt}\boldsymbol{i} + \mathbf{L}\frac{d\boldsymbol{i}}{dt} + \mathbf{R}\boldsymbol{i} \tag{1.1}$$

where $\mathbf{R}$ is a diagonal matrix with elements corresponding to the resistances of the individual circuit elements and $\mathbf{L}$ is the inductance matrix.

The inductance matrix $\mathbf{L}$ is a symmetric matrix made up of the self-inductance of the individual elements L' and the mutual inductance between circuit elements M (with m total circuit elements)

$$\mathbf{L} = \begin{bmatrix} L'_{1,1} & M_{1,2} & \dots & M_{1,m} \\ M_{2,1} & L'_{2,2} & \dots & M_{2,m} \\ \vdots & & \ddots & \vdots \\ M_{m,1} & \dots & & L'_{m,m} \end{bmatrix}. \tag{1.2}$$

The two subscripts of L' or M describe the circuit elements under consideration.

Note in Eq. (1.1) that rapid changes in inductance can effect the voltage of the terminals. In theory, sufficiently fast changes in inductance could overcome the resistive losses and generate electrical power. As a sensor, however, the primary concerns are the inductance L and resistance R measured at the terminals. In this dissertation, it is assumed that the circuit is excited by sufficiently high frequency currents to neglect the product of the current and the time-rate-of-change in inductance

$$\text{for } \frac{d\mathbf{L}}{dt}\boldsymbol{i} \approx 0, \;\; \boldsymbol{v} \approx \mathbf{L}\frac{d\boldsymbol{i}}{dt} + \mathbf{R}\boldsymbol{i}. \tag{1.3}$$

For the air-core circuits presented in this work, the inductance is typically on the order of micro-Henries and the resistance is on the order of Ohms. The resistance is many orders of magnitude higher than that of the inductance. Accordingly, high-frequencies of current are needed to create reactance from the inductance. The higher the frequency, the larger the relative amplitude of $\frac{d\boldsymbol{i}}{dt}$ to $\boldsymbol{i}$ becomes.

1.2.7 Inductance-based sensors

Inductance sensors come in many varieties. Inductance sensors can measure proximity, displacement and rotation. By exciting eddy currents, they can also identify the presence of flaws in nearby metal "targets." The changing permeability of magnetic cores under strain can be used to create force or torque sensors. One advantage of inductance sensors is that they can often be made to operate "contact free" in harsh environments [117]. On the other hand, the precision winding, cores and shielding of many inductance-based sensors can make them bulky and expensive. Additionally, the measurement of inductance often relies on analog circuitry that can be intimidating to system designers. Recent developments, however, have facilitated the measurement of inductance with digital interfaces.

Inductance-based sensors can measure displacement through the motion of a ferromagnetic core [117]. For example, the motion can be used to increase the "air gap" of a single winding inductor resulting in a decrease in inductance. A similar principle has been applied to measure the piston position in rigid fluid-powered actuators [118]. The Linear Variable Displacement Transformer (LVDT) relies on balanced primary and secondary windings. A common configuration is to have the primary coil between two secondary coils that are connected in series with opposite polarity. When the core is centered, there is no induced current in the secondary circuit. Moving the core to either side linearly increases the amplitude of the current in the secondary circuit. Similar techniques can be used to create rotational sensors.

Inductance sensors may also rely on induced eddy currents in a nearby metal target [117], [119]. Exposing conductive metal to the alternating field of a coil will induce currents in the metal which oppose the field of the coil. This can be used to create proximity switches as well as distance sensors. The inductance sensors can also be used at a fixed distance to detect flaws within a metallic structure [119], [120].

Changing levels of inductance have also been used for force and torque transducers. The "Villari effect" changes the magnetic susceptibility of metals under stress and is pronounced in certain nickel alloys [121]. This effect describes the change in an alloy's magnetic susceptibility in the presence of mechanical stress. By measuring the inductance of a coil with an alloy core, the stress can be deduced. Another strategy is to use inductance sensors to measure the deformation of a compliant structure with known stiffness [117], [122].

The analog circuitry necessary to excite and measure inductive coils has been a barrier to the widespread application of inductance-based sensing. Recently, microchip-based, low-power and precise inductance-sensing technology has become available [123]. For example, chips developed by Texas Instruments can quickly and precisely resolve the inductance of a parallel inductor-capacitor tank circuit with a fixed capac-

itor. This is accomplished by exciting and measuring the resonant frequency of the circuit [124]. This technology permits low-cost digital sensors that can measure precise changes in inductance. Other advances have allowed the development of inductive sensors that can be interrogated with a remote wireless coil [125].

1.2.8 Inductance Sensing in Soft, Fluid-Driven Structures

Sensors for soft fluid structures that rely on changes in inductance have been proposed in various forms. Since the commencement and partial publication of elements of this work, others have begun to replicate the results and explore similar ideas [126].

Stretchable belts with integrated wires have long been used to measure the expansion of the human abdomen and thorax via respiratory inductance plethysmography. By using wires in a "zig-zag" pattern on the belt, a stretchable, single turn coil is created. The inductance of this coil can be used to estimate its cross-sectional area. A similar technique has been used recently to measure the expansion of a balloon catheter. The zig-zag pattern, in this case, is created with a standard sewing machine [127].

There are also many patents and patent applications for inductance sensors for soft, fluid-driven actuators. The automation company Festo has a patent for a system with a solenoid-like coil wrapped around an iron-filled elastomer inside of a soft fluid actuator [84]. There are several systems proposed in patents or patent applications for measuring the height of air suspension systems with inductance or magnetic coupling. According to the nature of patents, the description of the technology is often quite vague. One patent describes conical metal springs inside of rolling-sleeve air springs [128]. The shortening of the air spring changes the length and inductance of the metal springs. Other patents propose incorporating conductive elements into the walls of a flexible air spring [129]–[131]. The changing geometry of helical elements, for example, could lead to a change in inductance with height [130]. The changing

overlap of the conductors could lead to a variable capacitance with height [129]. In addition to measuring the actuator length, the conductive elements could be used to heat the rubber in extreme cold [131]. Another proposal is to use the magnetic coupling of short wire coils at the ends of an air spring [132]. A prototype of this system has been tested [133].

1.3 Need for Further Research

In certain settings, it is possible to adapt traditional, rigid-sensing techniques to soft actuators. Soft sensing technologies are the subject of ongoing research and often require complex fabrication techniques. Many rely on the deformation of elastomers or the bending of fragile optical fibers. There has been virtually no scientific effort to understand how inductance-based sensors could be used to sense and control the motion of soft robotic systems. Inductance-based sensors have the potential to be used in the same harsh environments for which soft robots are so promising.

1.4 Research Goal

This dissertation provides the fundamental knowledge necessary for the design, analysis, fabrication and use of inductance-based sensors for soft fluidic devices. My contributions include models for the inductance and resistance of sensors making up the helical fibers of Fiber Reinforced Elastomeric Enclosures (FREEs). Such sensors are referred to as "Smart Braids." The models developed here inform the design choices of Smart Braid sensors. The models are experimentally validated for the case of a McKibben muscle actuator. The sensors are experimentally evaluated as feedback for the motion control of two application-like robotic test-beds.

This work also includes an investigation of inductance-based sensors for bellows-driven devices. Models for the inductance are developed and the implications for

design are explored. The sensors are also fabricated and evaluated in a robotic test-bed.

The goal of this research is to study inductance-based sensors that can create state estimation for feedback in fluid-powered soft robotic applications. This research investigates the feasibility of the proposed sensing method through models, experimentation and application. The models developed here will enable rigorous design methodologies. The proposed sensing circuits have been fabricated and tested on soft robotic actuators and systems. These actuators and systems have served as test-beds to validate the models, to reveal additional design considerations, and to characterize the performance of the proposed sensors.

1.5 Contributions

This dissertation represents the first serious scientific exploration into the use of inductance-based sensors for the estimation and control of soft robotic systems. The sensing systems proposed in this work rely on measurements of inductance from conforming electrical circuits. By designing the current paths appropriately, one can create inductance changes that provide a reliable measure of actuation. By using flexible off-the-shelf wires, this solution is low-cost, lightweight and preserves the unique advantages of soft robotic systems.

The specific contributions are:

1. Chapter II: **Developed a novel, closed-form kinematic model for Fiber-Reinforced Elastomeric Enclosures (FREEs).**

2. Chapters III-V: **Investigated the design and experimentally tested the use of conductive reinforcing fibers ("Smart Braids") to sense and control the motion of FREE actuators and systems.**

(a) Derived models for the inductance and resistance of Smart Braid circuits on FREE actuators (Chapter III).

(b) Explored the design space of Smart Braid sensors. Studied the influence of the design parameters on the electrical properties of the circuit (Chapter III).

(c) Experimentally validated the inductance models in a McKibben muscle FREE (Chapter IV).

(d) Experimentally evaluated the performance of the Smart Braid sensors as state-estimators for feedback in two application-like systems (Chapter V).

3. Chapter VI: **Investigated the design and experimentally tested the use of inductance-based sensors for bellows-driven continuum joints.**

(a) Derived models of inductance-based sensors on bellows actuators.

(b) Explored the effect of design parameters on the performance of inductance-sensors on bellows.

(c) Modeled and experimentally evaluated inductance-based sensors on a two-degree-of-freedom continuum joint driven by bellows.

In order to explore the design of Smart Braid sensors on FREEs, it was necessary for me to derive a new descriptive framework for FREE actuators. The framework I developed describes the behavior of each FREE by a single unitless quantity η. This quantity parameterizes a functional relationship between the fiber angles of the actuator. The resultant kinematic model allows the behavior of FREEs to be analyzed independent of actuator-specific geometry. It is the first kinematic model of FREE fibers that can be used to calculate large deformations without the need to iteratively compose small deformations from local "instantaneous" strain. The closed-form nature of this model has enabled new design analyses for FREE actuators.

With this new model, I derived models for the inductance and resistance of FREE actuators. These models enabled me to analyze the effect of design parameters on Smart Braid performance. I identified regions of the FREE design space for which Smart Braid sensors provide useful measures of actuator motion (and regions for which they do not). I fabricated a Smart Braid in a McKibben muscle pattern and compared the experimentally-measured inductance values to those predicted by the models. This Smart Braid was then tested as the reinforcement of an actual actuator. As predicted by the model, the inductance-response to contraction was linear. It showed virtually no hysteresis and resulted in actuator length estimates with approximately 1 mm of error (for a 29 cm braid). Smart Braid McKibben muscles were then integrated into two soft robotic systems to test the ability of the sensors to provide estimation suitable for feedback control. Closed-loop motion control was demonstrated in both a revolute joint and a bending continuum manipulator.

This dissertation also explores the use of inductance-based sensors to estimate and control bellows-driven devices. The inductance sensors were modeled and the effect of the design choices was analyzed. The sensors were experimentally evaluated in a commercial, 2-DOF bellows-driven continuum joint. This is an example of a system that would be difficult to measure with traditional sensors. The inductance-based sensors were able to measure the orientation of the joint with an RMS error of approximately 1.1 ° and control it with steady-state RMS error of less than 3 °.

CHAPTER II

A Closed-Form Kinematic Model for Fiber Reinforced Elastomeric Enclosures

Adapted from Wyatt Felt and C. David Remy. "A Closed-Form Kinematic Model for Fiber Reinforced Elastomeric Enclosures." *ASME Journal of Mechanisms and Robotics (Under Review).*

2.1 Introduction

Soft, fluid-driven actuators use structured compliance to create motion from the expansion of flexible volumes. Actuators based on these principles may, for example, contract along a central axis like biological muscles [38]. The McKibben muscle is a popular variety of such "pneumatic artificial muscles." Each McKibben muscle consists of an elastomeric tube surrounded by a sleeve of braided helical fibers. The braid is made up of equal numbers of right-handed and left-handed helices of the same pitch. They were developed in the 1950s by their namesake, Joseph Laws McKibben [134]. Since that time, they have been used in numerous applications such as legged robots and human assistive devices [135].

Joshua Bishop-Moser [136] extended the functional principle of McKibben muscles to a generalized class of cylindrical soft actuators known as Fiber-Reinforced Elas-

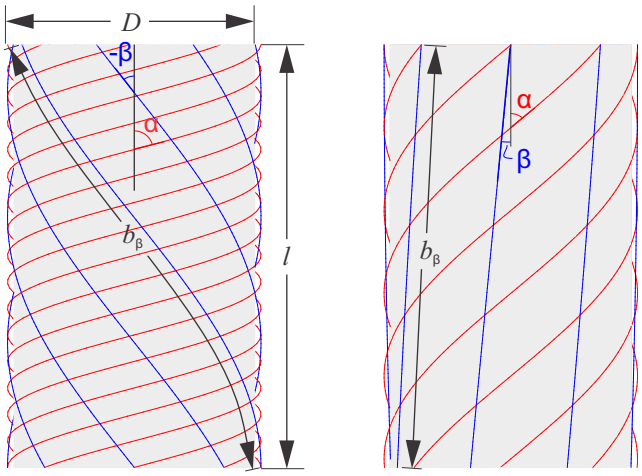

Figure 2.1: A Fiber-Reinforced Elastomeric Enclosure (FREE) is a cylindrical soft pneumatic actuator. A FREE consists of an elastomeric tube surrounded by sets (or "families") of identical helical fibers. The fibers in each family have the same angle with respect to the long axis (e.g. α) and the same "unwound" length (e.g. b_α). Shown here are examples of two-fiber-family FREEs. The families are respectively described by the angles α and β. The "unwound" length of the helical fibers in each family, b_α and b_β, remains constant, whereas the axial length l and diameter D change during actuation.

tomeric Enclosures (FREEs). Like McKibben muscles, FREE actuators are formed from two sets of identical helical fibers. A "set" or "family" of fibers is a group of fibers characterized by the same angle with respect to the cylinder axis (e.g. α or β). In the McKibben muscle, the two sets maintain equal and opposite angles ($\alpha = -\beta$). In a FREE, the fibers are wound with fiber angles selected by a designer to result in a desired behavior (Fig. 2.1). This choice of configuration permits complex actuated behaviors such as twisting while extending or contracting.

The kinematics of FREEs were initially developed only for small deformations. Krishnan et al. [137] described the motion of FREEs with instantaneous strain equations. These equations described the transformation of the FREE as a small change relative to its current configuration. To calculate the evolution of a FREE actuator over large deformations, the instantaneous strains were successively composed. This fiber-only kinematic model allowed the designer to consider the kinematics of the

FREE fibers under tension without considering the elastomer.

Combined fiber-elastomer methods model the motion of specific FREE actuators with specified geometries and defined elastomeric properties. For instance, finite-element solvers can be used to model FREEs [138]. Recent work has begun to explore the use of constitutive models to predict the motion of unloaded contracting, twisting or bending fiber-reinforced actuators [139] and torsionally loaded fiber-reinforced actuators [140]. These constitutive methods rely on models of strain energy in the elastomers and fibers to relate internal pressures to predicted deformations for specific actuator geometries. The governing equations of [137] can also be adapted to consider the elastomer [141].

The model presented in this chapter allows the designer to consider the kinematics of FREE fibers independent of specific geometry and material choices. For instance, in an FEA model, one would need to define the inner and outer diameter of the elastomer, the elastic material, a model for the elastic behavior, the length of the actuator, the two pitches of the fiber families, the fiber material, the number of reinforcing fibers in each family, the pressure ranges, etc. Once these choices have been made, a computationally intensive process must be conducted to evaluate the behavior of the specified FREE. After conducting a number of these numerical experiments, it is perhaps possible to extract some design heuristics from the observed behavior, but it is difficult to generalize the results.

In the model presented in this chapter, the behavior of the FREE actuators is described in terms of a single variable. This variable, η, is the ratio the lengths of the fibers in the two sets and is independent of the specific actuator geometry and materials. η is a design choice that is conserved over the course of actuation. The introduction of η allows this chapter to extend models developed for McKibben muscles [142] into the broader class of FREE actuators. The mathematical model presented in this chapter describes large-deformation kinematics of FREEs in closed-

form and without the need to compose a succession of instantaneous strains.

The kinematic model presented here describes the length, diameter, rotation and volume of FREE actuators as functions of the fiber angle β. The structure of this model provides a common language to describe every cylindrical, two-helical-fiber-set FREE by parameters that define the behavior (η) and state (β) of the actuator. The size and geometry of the actuator is given by the length b_β of the β fibers and the diameter D_0 (when $\beta = -\pi/2$).

The simple, analytic nature of this model facilitates the understanding and design of FREE actuators. The application of this model is demonstrated in an actuator design case study. In another example application, the model is used to understand how the reinforcing fibers limit the range of motion of FREE actuators.

2.2 Kinematic Modeling

2.2.1 Assumptions and Definitions

The model presented in this chapter assumes that the fiber-reinforced actuators are made from two sets of helical, inextensible fibers with respective angles α and β (Fig. 2.1). The fibers surround an elastomeric bladder containing the pressurized fluid. It is assumed that sufficient fibers are used to prevent the bladder from bulging between the gaps in the fibers. The elastomer is assumed to be infinitely extensible with negligible stiffness. The fibers are assumed to be always under tension from the internal pressure in the bladder. Because the individual fibers within the families are identical, the kinematics of only one fiber in each family need to be considered.

It is also also assumed that the profile of the FREE actuator remains cylindrical. This approximates an unbent actuator away from its ends. At the actuator ends, the diameter tapers to match the fixed-diameter of the end [143]. The cylindrical assumption allows the adaptation of simple helical formulas that have long been used

to describe McKibben muscles [142]. The length of this cylinder is l and its diameter is D. All fibers wrap around it in a helical fashion. The individual fibers in their respective families behave identically. They all have the same axial length l and diameter D as the cylinder. Under these assumptions, the length of the cylinder l is related to the "unwound" length b of the fibers in a family via the cosine of their angle

$$l = b_\alpha \cos(\alpha) = b_\beta \cos(\beta)\,. \tag{2.1}$$

Similarly, the diameter of the cylinder D is a function of the fiber angles and fiber lengths

$$D = \frac{b_\alpha \sin(\alpha)}{n_\alpha \pi} = \frac{b_\beta \sin(\beta)}{n_\beta \pi}. \tag{2.2}$$

The diameter is additionally a function of the number n of times that the fiber circles the axis. For example, $n_\alpha = 0.75$ signifies that, at the current diameter, the fibers of the α family circle the axis three-quarters of one time. The sign of n indicates the handedness of the helix (positive for right-handed) and matches the sign of the corresponding fiber angle.

$$\begin{aligned} \text{sign}(n_\alpha) &= \text{sign}(\alpha) \\ \text{sign}(n_\beta) &= \text{sign}(\beta)\,. \end{aligned} \tag{2.3}$$

The cylinder diameter and length will change as the actuator volume expands. These changes will correspond to changes in the fiber angles α and β. The number n of fiber turns may also change as the actuator ends rotate relative to one another about the cylinder axis. The "unwound" length b of the fibers, however, remains constant.

Krishnan et al. [137] analyzed the instantaneous kinematics of FREEs with values of α and β between -90 ° and 90 °. As they noted, however, the symmetry of FREEs makes this formulation redundant. This model eliminates the redundancy, without loss of generality, by deliberately specifying which fiber family is labeled by α and

which is labeled by β. In this model, the angle α is used to describe the family with the greater or equal "unwound" fiber length b (i.e. $b_\alpha \geq b_\beta$, and thus $|\alpha| \geq |\beta|$). Furthermore, the analysis is restricted to helices formed by the α fibers that are right-handed and thus maintain a positive value of α. Because α is always positive, and α is strictly greater than β (β is negative when $|\alpha| = |\beta|$), both angles cannot be equal to zero simultaneously.

$$\begin{aligned} 0 < \alpha \leq \frac{\pi}{2} \\ -\alpha \leq \beta < \alpha \end{aligned} \tag{2.4}$$

2.2.2 Behavior Described by η, State by β

The behavior of a FREE actuator is defined by the ratio η of the "unwound" lengths b of the fibers from the two sets

$$\begin{aligned} \eta = \frac{b_\beta}{b_\alpha} \\ 0 < \eta \leq 1. \end{aligned} \tag{2.5}$$

Under the assumptions of this model, the angle α follows uniquely from the angle β. With η, a simple analytic relationship between the fiber angles can be developed from Eq. (2.5) and Eq. (2.1)

$$\alpha = \cos^{-1}(\eta \cos(\beta)) \,. \tag{2.6}$$

Equation (2.6) provides a clear functional relationship between the angles of each FREE (Fig. 2.2) parameterized by η.

The relationship between the fiber angles described by Eq. (2.6) has been observed previously but never defined in such an explicit form. Krishnan et al. [137] noted that each two-fiber-family FREE belongs to "a one-dimensional family of fiber angle configurations." With the model presented here, it is now clear that the ratio η

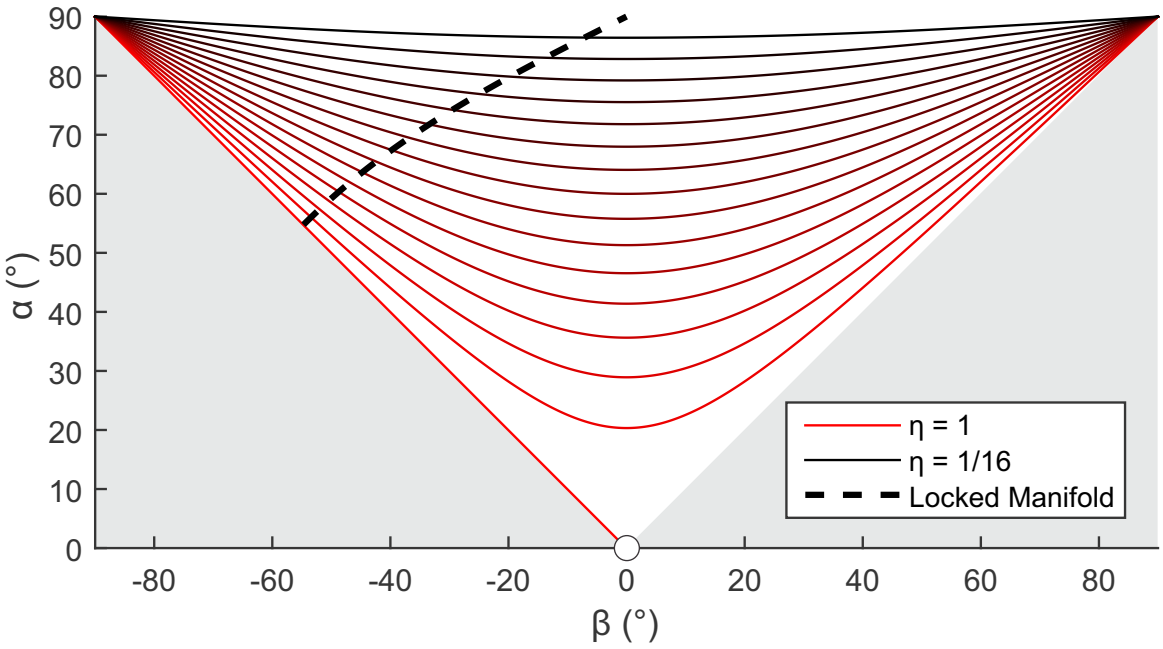

Figure 2.2: The ratio $0 < \eta = \frac{b_\beta}{b_\alpha} \leq 1$ of the lengths of fibers in the two families determines the feasible angle combinations for a FREE actuator. The angle β can be used to specify the state of the actuator along the functional relationship of possible combinations. The locked manifold (dashed black line) is the set of angle combinations that maximize the volume of the actuator. When the volume of the actuator is increased by an internal pressure, the configuration of the actuator will advance towards the locked manifold. The gray regions of the figure are redundant and thus not specifically defined by this model. β is constrained to remain strictly less than α. Thus, when $\eta = 1$ ($\alpha = -\beta$), β is constrained to be less than zero. This is indicated by the circle at the origin. The feasible region includes the line $\alpha = -\beta$ but the line $\alpha = \beta$ is excluded. The values of η shown in this figure (and the others) are: 1, $\frac{15}{16}$, $\frac{7}{8}$, $\frac{13}{16}$, $\frac{3}{4}$, $\frac{11}{16}$, $\frac{5}{8}$, $\frac{9}{16}$, $\frac{1}{2}$, $\frac{7}{16}$, $\frac{3}{8}$, $\frac{5}{16}$, $\frac{1}{4}$, $\frac{3}{16}$, $\frac{1}{8}$, and $\frac{1}{16}$.

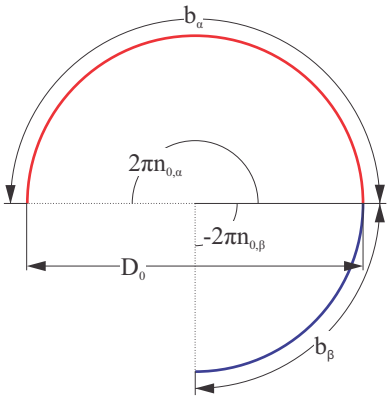

Figure 2.3: When the helices are planar circular arcs, the diameter is D_0. Shown here are the paths of an α fiber (red) and a β fiber (blue) for $\eta = 0.5$, $n_{0,\alpha} = 0.5$ and $n_{0,\beta} = -0.25$.

and Eq. (2.6) can be used to define this one-dimensional "family" of fiber angle configurations.

2.2.3 Size Described by b_β and D_0

The length, diameter and volume of a FREE actuator can be described as functions of η and β and variables that describe the dimensions of the particular actuator, b_β and D_0. The first of these, b_β, is the "unwound" length of the individual fibers in the β family (Figs. 2.1 and 2.3). The diameter D_0 is a standardizing measurement used for McKibben muscle actuators [142]. This quantity can also be defined for FREE actuators (Fig. 2.3). D_0 is calculated from Eq. (2.2). It is the diameter of the helices if $\beta = -\pi/2$ (and thus $\alpha = \pi/2$)

$$D_0 = \frac{b_\alpha}{n_{0,\alpha}\pi} = -\frac{b_\beta}{n_{0,\beta}\pi} \tag{2.7}$$

where n_0 is the number of fiber turns at that diameter.

Thus each FREE actuator can be defined by the actuator-specific quantities η, b_β and D_0. The state of the actuator is given by β. Examples of FREEs with the same values of b_β and D_0 (but different values of η and β) are shown in Figure 2.4.

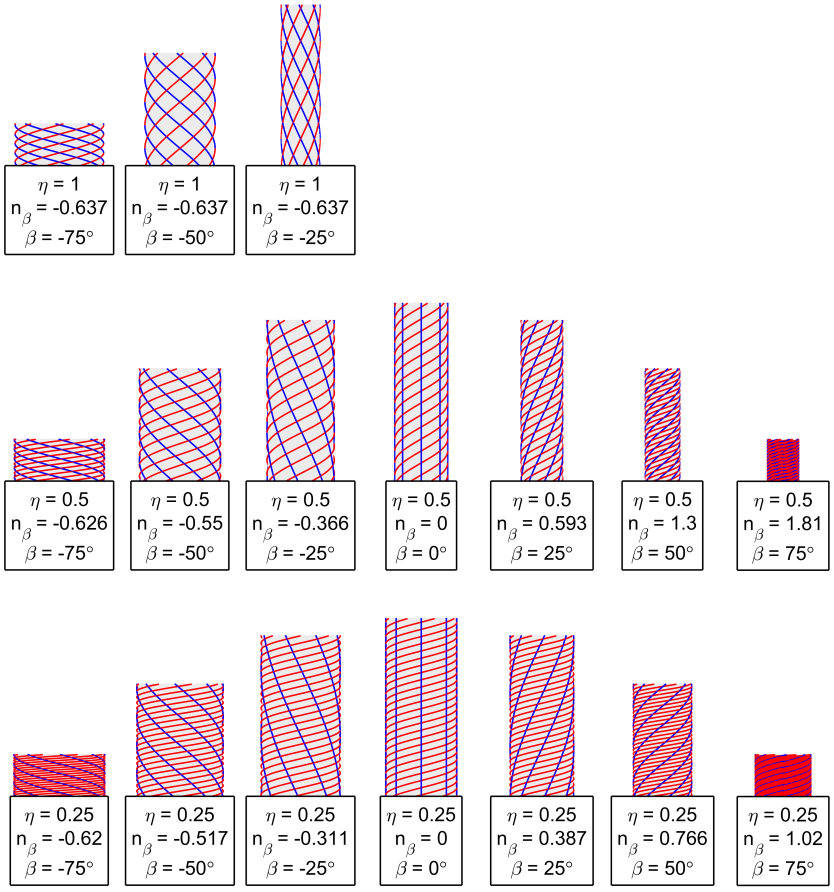

Figure 2.4: Examples of FREEs with the same b_β and D_0 but different η levels at various values of β. For the actuators shown here, D_0 is half of b_β. Each row corresponds to a value of η and each column a value of β.

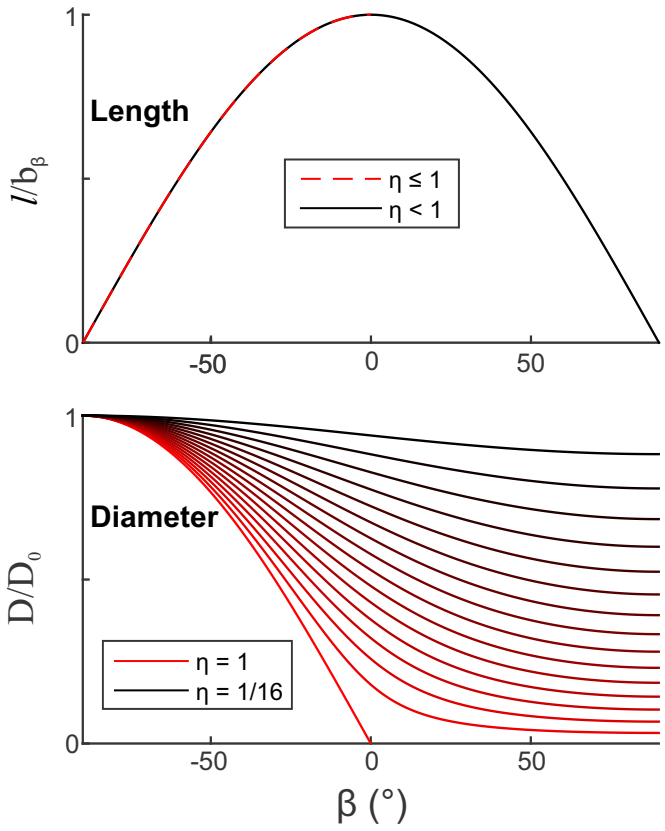

Figure 2.5: The length and diameter of FREE actuators for various values of η across β. The length of the actuator is the cosine function scaled by b_β and is always greatest at $\beta = 0$ ($l = b_\beta$). The diameter scales linearly with D_0 and always increases with decreasing values of β. The maximum diameter is D_0.

2.2.4 Calculating Rotation Δn, Diameter D, Length l, Volume V and Surface Area A_{surf}

The model presented in this chapter allows the length, rotation, diameter and volume of a FREE actuator to be described as functions of the actuator state β. The expression for the axial length $l(\beta)$ (Fig. 2.5) is straightforward and is given by Eq. (2.1)

$$l(\beta) = b_\beta \cos(\beta)\,. \tag{2.8}$$

Note that the length of the actuator scales linearly with the length b_β and that the maximum length achievable by the actuator is b_β.

The axial rotation of the actuator is designated by Δn and is conserved in the fiber turns n_α and n_β at D.

$$\begin{aligned} n_\alpha &= n_{0,\alpha} + \Delta n \\ n_\beta &= n_{0,\beta} + \Delta n \end{aligned} \tag{2.9}$$

where Δn is zero when $D = D_0$. Eq. (2.2) leads to an expression for Δn

$$\Delta n = -n_{0,\beta} \frac{\sin(\beta) + \sin(\alpha)}{\sin(\alpha) - \eta \sin(\beta)}. \tag{2.10}$$

Note that there is no rotation when $\eta = 1$ (McKibben muscle)

$$\begin{aligned} \eta = 1 \rightarrow \beta = -\alpha \rightarrow \\ \sin(\beta) + \sin(\alpha) = \sin(-\alpha) + \sin(\alpha) = 0 \rightarrow \\ \Delta n = 0. \end{aligned} \tag{2.11}$$

Substituting Eq. (2.6) into Eq. (2.10) gives the axial rotation $\Delta n(\beta)$ in radians

$$\Delta n(\beta) = -n_{0,\beta} \frac{\sqrt{1 - \eta^2 \cos^2(\beta)} + \sin(\beta)}{\sqrt{1 - \eta^2 \cos^2(\beta)} - \eta \sin(\beta)}. \tag{2.12}$$

The rotation Δn scales linearly with $n_{0,\beta} = \frac{-b_\beta}{\pi D_0}$ (Fig. 2.6).

The diameter $D(\beta)$ is found by substituting Eq. (2.6), Eq. (2.7), Eq. (2.9) and Eq. (2.12) into Eq. (2.2) (Fig. 2.5)

$$D(\beta) = D_0 \frac{\sqrt{1 - \eta^2 \cos^2(\beta)} - \eta \sin(\beta)}{1 + \eta}. \tag{2.13}$$

The diameter scales linearly with D_0.

Assuming that the thickness of the elastomer inside the fibers is negligible, the internal volume of the actuator is given by the volume $V(\beta)$ of the cylinder contained

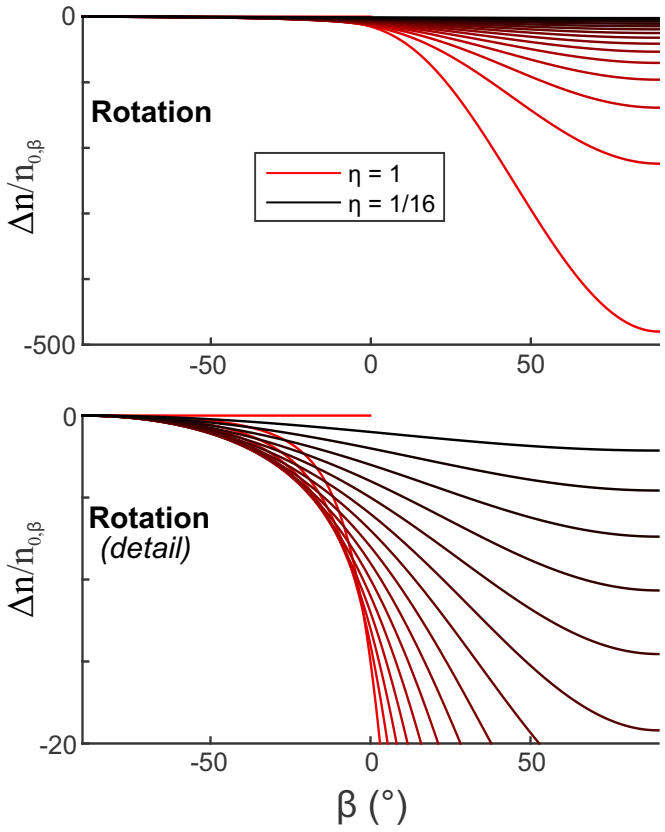

Figure 2.6: The axial rotation of FREE actuators for various values of η across β. For $\eta = 1$ there is no rotation. The values shown here are normalized by $n_{0,\beta}$. Note that $n_{0,\beta} = \frac{-b_\beta}{\pi D_0}$.

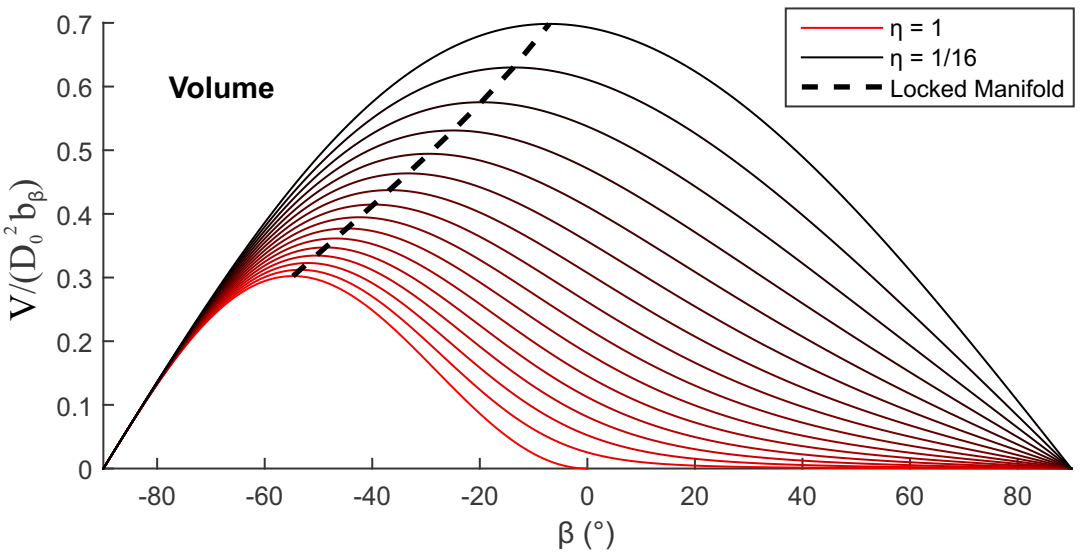

Figure 2.7: The volume of FREE actuators for various values of η across β. The volume values shown here are normalized by $D_0^2 b_\beta$. Each value of η corresponds to a unique angle β_{LM} that maximizes the cylinder volume.

within the fiber helices (Fig. 2.7)

$$V(\beta) = \frac{\pi}{4} D(\beta)^2 \, l(\beta) \, . \tag{2.14}$$

Substituting Eq. (2.8) and Eq. (2.13) into Eq. (2.14) yields

$$V(\beta) = \frac{\pi}{4} D_0^2 b_\beta \frac{\cos(\beta) \left(\sqrt{1 - \eta^2 \cos^2(\beta)} - \eta \sin(\beta) \right)^2}{(1+\eta)^2} . \tag{2.15}$$

From Fig. 2.7 it is clear that the volume of each FREE type has a unique maximal point. For example, for the McKibben muscle case when $\eta = 1$ and $\alpha = -\beta$, the volume is maximized when $\beta \approx -54.7°$. This has long been known [142]. Here, the value of β that maximizes the volume is designated β_{LM}. Smaller values of η correspond to less negative values of β_{LM}. Because internal pressures drive the volume to expand, an actuator fabricated with a β value greater than β_{LM} will decrease in β

under actuation. Similarly, actuators with β less than β_{LM} will increase in β under actuation. The derivative of the volume with respect to β is given by

$$\begin{aligned}\frac{dV}{d\beta} = -\frac{\pi}{4} D_0^2 b_\beta \frac{\left(\gamma - \eta \sin(\beta)\right)^2 \left(\sin(\beta)\,\gamma + 2\eta \cos^2(\beta)\right)}{\left(1+\eta\right)^2 \gamma} \\ \gamma = \sqrt{1 - \eta^2 \cos^2(\beta)}.\end{aligned} \tag{2.16}$$

The maximum volume occurs when $\frac{dV}{d\beta}$ is zero. Equation (2.16) yields the following invertible expression relating η to the angle β_{LM} that maximizes the volume

$$\begin{aligned}\frac{dV}{d\beta} = 0 \rightarrow \\ \eta = \frac{1}{\cos(\beta_{LM})\sqrt{4\cot^2(\beta_{LM}) + 1}} \\ -2\tan^{-1}\left(\sqrt{2-\sqrt{3}}\right) \leq \beta_{LM} < 0.\end{aligned} \tag{2.17}$$

The α and β combinations that maximize FREE volume were described by Krishnan et al. [137] as a "locked manifold" (Fig. 2.2)

$$1 + 2\cot(\alpha_{LM})\cot(\beta_{LM}) = 0 \tag{2.18}$$

where the corresponding angles are designated with the subscript LM. "Locked" refers to the fact that internal pressure can no longer drive the actuator to deform because the volume is already maximized. Substituting Eq. (2.6) into Eq. (2.18) yields Eq. (2.17).

The surface area of the actuator is the product of the circumference and the length

$$\begin{aligned}A_{\text{surf}}(\beta) &= \pi D(\beta)\, l(\beta) \\ &= \pi D_0 b_\beta \cos(\beta)\, \frac{\sqrt{1 - \eta^2 \cos^2(\beta)} - \eta \sin(\beta)}{1+\eta}.\end{aligned} \tag{2.19}$$

The surface area scales linearly with D_0 and b_β (Fig. 2.8).

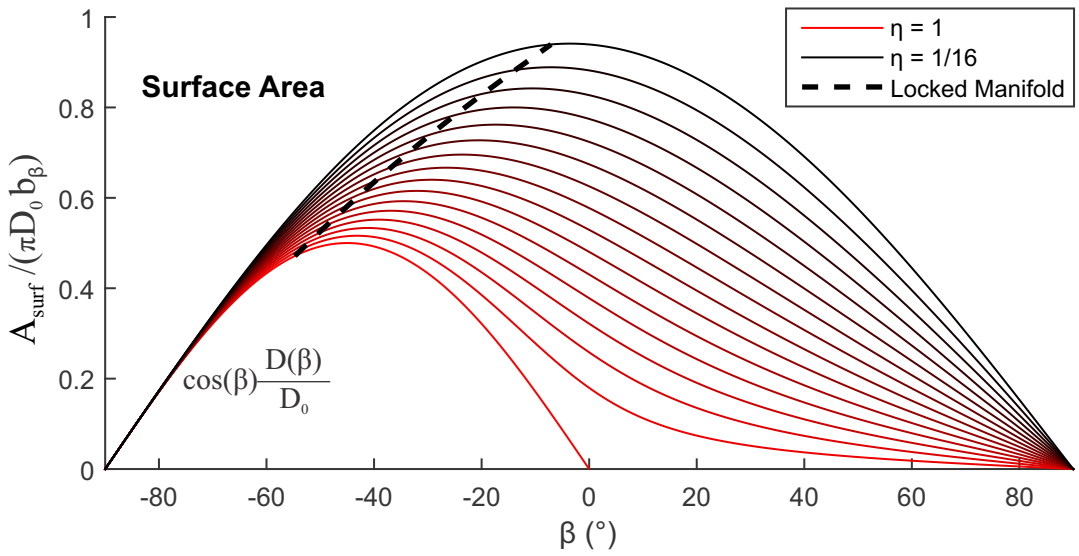

Figure 2.8: The surface area of FREE actuators for various values of η across β. The surface area is related to the actuator range of motion. The surface area values shown here are normalized by $\pi D_0 b_\beta$. This normalized surface area corresponds to the maximum levels of G (for a given value of η) for which β is achievable (Eqns. (2.27) and (2.29)). G is a value that relates the thickness and number of fibers in each family to the size of the actuator.

2.3 Examples of Model Applications

The model presented in this chapter enables simple, closed-form design analyses for FREE actuators. This section explores two example applications of the model. First, specifications of FREE motion are used with the model to design in an actuator design case study. Second, is an exploration of how the motion range of a FREE actuator may be limited by the physical interference of the fibers.

2.3.1 Actuator Design Case Study

The model presented in this chapter can be used in FREE design. Consider, for example, a FREE that is specified to contract from an unpressurized length $l_1 = 5\,\text{cm}$ to $l_2 = 4\,\text{cm}$ while rotating a quarter-of-a-turn about its axis. The diameter of the actuator at the contracted state is to be $D_2 = 2.5\,\text{cm}$. To ensure that the contracted configuration will be achievable through pressurization, the angle β_2 of the fibers in

the contracted state is specified to be 10 ° greater than the angle β_{LM} that maximizes the volume.

By inspection, for an axially contracting actuator, the following must be true

$$-54.7^{\circ} < \beta_{LM} < \beta_2 < \beta_1 < 0. \tag{2.20}$$

The initial unpressurized angle β_1 can be selected numerically such that the quarter-turn rotation constraint is satisfied

$$n_{1,\beta} - n_{2,\beta} = \frac{b_\beta \sin(\beta_1)}{D_1 \pi} - \frac{b_\beta \sin(\beta_2)}{D_2 \pi} = 0.25 \tag{2.21}$$

where the rotation comes from the difference in the number of fiber turns given by inverting Eq. (2.2). The unknown values in Eq.(2.21) are functions of the specified kinematics and β_1. b_β comes from inverting the length expression in Eq. (2.1)

$$b_\beta = \frac{l_1}{\cos(\beta_1)}. \tag{2.22}$$

The angle β_2 of the fibers in the contracted state is given by inverting Eq. (2.1) and considering that β_2 must be negative due to Eq. (2.20)

$$\beta_2 = -\cos^{-1}\left(\frac{l_2}{b_\beta}\right). \tag{2.23}$$

The angle β_{LM} is given by the constraint that β_2 be 10 ° greater than β_{LM}

$$\beta_{LM} = \beta_2 - 10\frac{\pi}{180} \tag{2.24}$$

which, by Eq. (2.17), can be used to calculate η. The value of D_0 is found by inverting

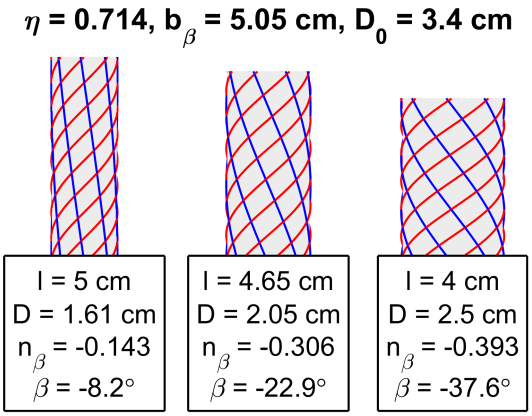

Figure 2.9: The model can be used to design FREEs that meet specified kinematics. For instance, the FREE shown in this figure was designed to rotate a quarter turn while contracting 20 %.

Eq. (2.13) with the values of D_2, β_2 and η

$$D_0 = D_2 \frac{1+\eta}{\sqrt{1-\eta^2\cos^2(\beta_2)} - \eta\sin(\beta_2)} \tag{2.25}$$

which allows D_1 to be calculated with Eq. (2.13), η and β_1.

The design specifications are achieved by fabricating an actuator with an unpressurized initial angle β_1 of -8.2 ° (Fig. 2.9, $\eta = 0.714$, $b_\beta = 5.05\,\text{cm}$, $D_0 = 3.4\,\text{cm}$).

2.3.2 Fiber Interference and Range of Actuation

A FREEs range of motion may be limited by the physical interference of the fibers. The analysis allows one to compute the region of β for which there is physical space on the actuator for the specified fiber sets. It is an extension of a similar analysis by Davis and Caldwell for McKibben muscles [144]. This analysis assumes that the reinforcing fibers are layered on the actuator (instead of braided or interwoven). It is also assumed that the diameter of the actuator is much larger than the diameter of the fibers such that the two sets of helices can be considered to have the same axial

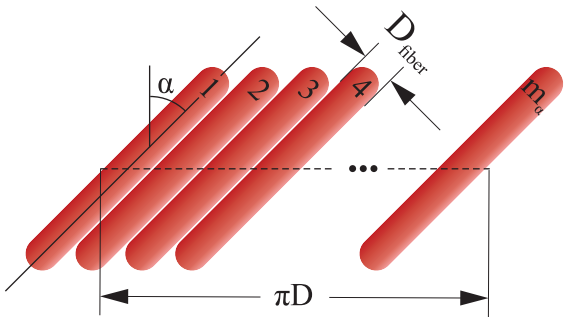

Figure 2.10: The multiples m of the fibers with diameter D_{fiber} must fit within the circumference πD of the actuator. This is true for the α (shown here) and β fiber families.

diameter.

Consider a FREE fabricated from multiple fibers in each fiber family. The numbers of helices in the α and β families is represented by m_α and m_β, respectively (e.g. $m_\alpha = 5$ means there are five fibers with angle α spaced around the axis of the actuator). The fibers are considered to have the same thickness characterized by a diameter D_{fiber}. The thickness of the fibers imposes a limit on the achievable angles. This constraint can be considered in terms of the actuator circumference (Fig. 2.10)

$$\begin{aligned} D\pi > & \frac{m_\alpha D_{\text{fiber}}}{\cos(\alpha)} = \frac{m_\alpha D_{\text{fiber}}}{\eta \cos(\beta)} \\ D\pi > & \frac{m_\beta D_{\text{fiber}}}{\cos(\beta)}. \end{aligned} \tag{2.26}$$

It is apparent that the m_β constraint is active in defining the boundary when $m_\alpha \leq \eta m_\beta$. That is, when the number of α fibers is less than η times the number of β fibers, then the β fibers constrain the actuator motion. When the number of α fibers exceeds η times the number of β fibers, then α fibers constrain the actuator motion. Thus, for example, a FREE actuator where $\eta = 0.1$ can have up to ten times the number of β fibers as α fibers without the β fibers limiting the actuator motion.

These constraints can be written in terms of a variable G

$$\begin{aligned} \cos(\beta)\,\frac{D(\beta)}{D_0} &> G_\alpha = \frac{1}{\eta}\frac{m_\alpha D_{\text{fiber}}}{\pi D_0} \\ \cos(\beta)\,\frac{D(\beta)}{D_0} &> G_\beta = \frac{m_\beta D_{\text{fiber}}}{\pi D_0}. \end{aligned} \tag{2.27}$$

G_β is the ratio of the width of the β fibers, if they were laid side-by-side, over the circumference of the actuator at D_0. The value G_α is the same ratio for the α fibers but divided by η. The values of G_α and G_β will remain less than the cosine of β times the normalized diameter $D(\beta)/D_0$ given by

$$\frac{D(\beta)}{D_0} = \frac{\sqrt{1-\eta^2\cos^2(\beta)} - \eta\sin(\beta)}{1+\eta}. \tag{2.28}$$

The inequalities in Eq. (2.29) are equivalent to the constraint that both values of G remain less than the normalized surface area

$$\begin{aligned} G_\alpha &< \frac{A_{\text{surf}}(\beta)}{\pi D_0 b_\beta} \\ G_\beta &< \frac{A_{\text{surf}}(\beta)}{\pi D_0 b_\beta}. \end{aligned} \tag{2.29}$$

Equations (2.27) and (2.29) define the boundary of the feasible configurations. For an actuator fabricated with certain values of G_α and G_β, the feasible region of β is given by the portion of the line in Fig. 2.8 above the larger G-value (e.g. G_α or G_β).

Examples of using the constraints in Eqns. (2.27) and (2.29) to evaluate the feasible range of β are listed in Table 2.1.

2.4 Discussion

The model presented in this chapter provides a closed-form framework for kinematic analysis and design of FREE actuators. The introduction of η and the an-

η	m_α	m_β	G_α	G_β	$\beta_{\min}$	$\beta_{\max}$
1	32	32	0.102*	0.102*	-84.1	-5.88
1	**64**	32	0.204*	0.102	-78	-12
1	**32**	**64**	0.102	0.204*	-78	-12
0.5	32	64	0.204*	0.204*	-78	56
0.25	32	64	0.407*	0.204	-65	50
0.125	32	64	0.815*	0.204	-30	17

Table 2.1: Feasible ranges of β (°) without fiber interference for $D_0 = 10\,\text{cm}$ and $D_{\text{fiber}} = 1\,\text{mm}$ ("*" indicates that a G constraint is active). The elements of the design that change from row to row are indicated with bold text.

alytic relationship between the fiber angles given in Eq. (2.6) is one of the major contributions of this chapter. Previously published fiber-only models have relied on "instantaneous" kinematics [137] to incrementally update fiber angles. To solve for large deformations with instantaneous kinematics, the nonlinear equations had to be iteratively solved and composed. The model presented here provides analytic functions describing the actuator rotation, length, diameter and volume. These functions are parameterized by the kinematic state of the actuator given by the angle β.

The simplicity of the present model simplifies the design and understanding of FREEs. This chapter, for example, shows how the model can be used to design a FREE that achieves desired kinematic behavior. As another example, the chapter shows how the model can be used to derive closed-form inequalities which approximate the feasible range of motion permitted in FREE actuators with fibers of finite thickness.

In addition to the closed-form kinematics, the present model has several improvements to previous FREE fiber-only models. The deliberate designation of the longer set of fibers with α allows the present model to describe FREEs with just a diagonal quadrant of the α-β coordinate frame. The ratio η leads to a simple parametric functional relationship between α and β (the first of its kind). This allows the state of a FREE with a particular η value to be parameterized by a single angle β (rather

than describing the state with potentially infeasible combinations of α and β). Previous work discovered that "every FREE belongs to a one-dimensional family of fiber angle configurations" [137]. This work provides the first analytic description of these configurations.

The model presented here shares the assumptions of previously published models fiber models [136], [137]. The reformulation presented here is a simplification of the kinematic description in the previous models. Accordingly, the experimental verification of the previous models can be considered verification of the present work.

Like the models that have preceded it, the present model has limitations. External loading, for example, could buckle one or both of the fiber families. This would violate the assumption that the fibers are under tension. The model presented in this chapter is limited to rotation and/or length changes. Additional fiber families on FREEs can create planar [139] or helical [136], [145] bends. The angles of the fibers in this model are constrained to be non-zero. So-called "straight-fiber" actuators are not governed by the equations presented here [146]. The governing equations of [137] have been adapted to include elastomer effects and non-cylindrical deformation [141].

The model presented in this chapter does not take into account non-cylindrical deformations or strain in the elastomers. This unmodeled elastomer strain will limit the motion of a FREE actuator to a small section of the possible fiber-angle-combinations defined by η. To account for the effects of the elastomer, a designer could take the insights from this fiber-only model and further explore them with fiber-elastomer models (e.g. via FEA [138] or constitutive models [139], [140]).

The models presented in this chapter will facilitate the growing understanding of FREEs. The identification of the descriptor η allows the behavior of FREEs to be described independent of actuator-specific geometry. The linearly scaling models makes this behavior simple to predict and understand. As the understanding of FREEs grows, engineers will find new opportunities for these unique actuators to

expand the functional ability of soft, fluid-driven systems.

Understanding the geometry of Smart Braid fibers is key to understanding the inductance of circuits made from the fibers. The normalization of the FREE geometry into terms that depend only on η and β is key to the development of the inductance model in the subsequent chapter.

CHAPTER III

Modeling and Design of "Smart Braid" Inductance Sensors for Fiber-Reinforced Elastomeric Enclosures

Adapted from Wyatt Felt and C. David Remy. "Modeling and Design of "Smart Braid" Inductance Sensors for Fiber-Reinforced Elastomeric Enclosures." *(In preparation)*

3.1 Introduction

Soft, fluid-powered actuators can provide lightweight and compliant actuation for robots and assistive devices. These actuators generate motion through the expansion of flexible fluid-filled chambers. By integrating structured reinforcements in the flexible chamber, the volumetric expansion can be shaped into useful work. For instance, cylindrical braids of fibers can be used to shape the volumetric expansion of an elastomeric tube into a forceful contraction. This combined fiber-elastomer structure is known as a McKibben muscle [142] and has been used in research for many decades [135]. Recently, researchers have begun to explore the use of different fiber configurations to create other motions besides contraction [136]. For instance, actuators can be fabricated with fiber configurations that cause the actuator to twist as it extends

or contracts along its axis. The desired motion can be "mechanically programmed" into the actuator through the fiber configuration. This broader class of soft actuators is known as Fiber-Reinforced Elastomeric Enclosures (FREEs). These actuators can create appropriate motion profiles for many applications that would otherwise require complex mechanical systems. For instance, they have been proposed for use in pipe inspection and soft manipulation [145], [147]. Their soft nature makes them ideal for many tasks that involve handling delicate structures or interaction with the human body. For example, FREE-like actuators have been used to handle undersea coral [28] and to assist the human hand [27].

In these applications, the use of soft actuators has so far been limited to purely open-loop motions. Closed-loop motion control could enable more widespread use in robotic devices, but would require sensors to measure the actuator motion. To overcome this shortcoming, a number of soft sensing technologies have been proposed for actuators such as FREEs. A thorough review of the challenges and proposed solutions is given in the introduction of this dissertation.

This chapter provides a solid theoretical background for the sensing of FREE actuators with Smart Braids. To this end, this chapter derives a normalized model for the inductance and resistance of Smart Braid FREEs and analyzes the effect of a number of design choices onto the behavior of the resulting sensor. These effects include: the number of fibers, fiber size, resistivity and circuit configuration (series or parallel). The remainder of the chapter is structured as follows: the kinematics of FREEs are presented in Section 6.3.1; section 3.3 introduces the series and parallel wiring configurations; section 3.4 presents a normalized model for the inductance of Smart Braid FREEs that is validated numerically and compared to existing experimental data; this is followed by a resistance model (Section 3.5) and a discussion on Smart Braid FREE design (Sec. 3.6); conclusions about the design of Smart Braid FREEs conclude the chapter (Sec. 3.7).

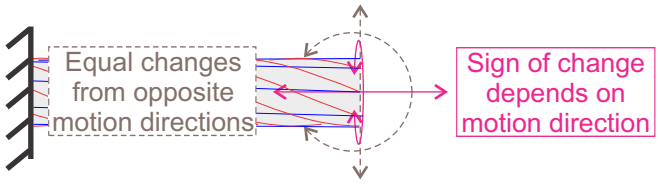

Figure 3.1: Because of the symmetry of a FREE, only relative rotations or translations between the cylinder ends along the axis result in distinguishable-sign changes in the geometry of the fibers.

3.2 Kinematics and Symmetries

As the volume a FREE expands from internal pressure, the geometry of the FREE fibers progresses, changing both the inductance and the relative positions of the actuator ends. By understanding the kinematics of a Smart Braid FREE, the changes in inductance can be understood in the context of the motion that is created by the actuator. This chapter considers Fiber-Reinforced Elastomeric Enclosures that are surrounded by two families of helical fibers with different pitch angles α and β. The geometry of the fibers is modeled with the assumptions and process outlined in Chapter II.

The cylindrical shape of the actuator and the periodic pattern of the fibers results in important symmetries. The geometry of the actuator fibers is invariant to rotations of $\frac{2\pi}{m}$ about the cylinder axis (Fig. 3.1). The geometric invariance of the actuator to rotations of $\frac{2\pi}{m}$ leads to the assumption that the self-inductance of each fiber is identical to that of the other fibers in its family. This symmetry also suggests that the sum of the mutual inductance pairs for a given fiber will be the same, regardless of which fiber in the family is considered.

Additionally, the linearized geometry response to many motions is zero. Consider a cylindrical FREE actuator undergoing small deformations away from a nominal straight configuration. If there are three or more fibers, the gradient of geometric changes is zero for deflections along or rotations about axes orthogonal to the cylinder

axis. In the linearized form, only relative deflections along or rotations about the cylinder axis have distinguishable geometry changes.

3.3 Serial vs Parallel Wiring Configurations

The fibers in a Smart Braid circuit may be wired in series or parallel. In the serial configuration, each end of the fibers in the α family is connected to the end of an adjacent fiber in the β family. Accordingly, a circuit is formed where the current from the first electrical terminal flows through each fiber in series before reaching the second electrical terminal (alternating between the α and β families).

In the parallel configuration, a parallel-group of the α fibers is connected in series with a parallel-group of the β fibers. From the first electrical terminal, the current first splits between all m of the α fibers before rejoining at the other end of the actuator. The current then splits between the β fibers before rejoining at the second electrical terminal. The current in each fiber is assumed to be an m-th fraction of the total current.

3.4 Inductance Model

A Smart Braid measures the motion of a FREE actuator through changes in the inductance of the conductive-fiber-circuit. Thus it is important to understand the relationship between the actuator motion and the inductance of the Smart Braid circuit. In this section, the inductance of Smart Braid FREEs is calculated across a range of η and β values to show the regions of the FREE design space in which Smart Braid sensing is useful. The resulting inductance values are then normalized by known scaling parameters to develop a general inductance model for Smart Braid FREEs. The model allows one to understand the trends in inductance independent of the geometries of a specific actuator. This model also analytically describes the

effect of certain design parameters on the FREE inductance. The model is validated numerically across the range of possible η and β values. The inductance predictions are also validated against experimental data for $\eta = 1$ (McKibben muscle).

The inductance of the Smart Braid circuit depends on the magnetic flux through the circuit. This flux is a function of the geometry of the circuit and the conductivity and magnetic permeability of the surrounding materials. The sensitivity of the inductance to the geometry of the circuit makes it possible to extract information about the actuator configuration from changes in the measured inductance. In this work, it is assumed that the circuit is sufficiently far from other conductors and ferromagnetic materials to neglect their effects.

3.4.1 Numerically Calculating Inductance

The complex geometry of Smart Braid FREE circuits makes a closed-form expression of the inductance intractable. With an analytic solution unavailable, it is necessary to rely on numerical methods to calculate the inductance values. To this end, a commercial tool, FastHenry2 [148], was used to calculate the inductance of a representative set of Smart Braid FREEs. The geometry of the circuits considered was selected to be similar to current experimental methods, to facilitate the normalization process described in Section 3.4.2, and to be computationally feasible.

For the calculation, the diameter D_0 was assumed to be 10 cm and the number $n_{0,\alpha}$ of turns at that diameter was ten. The geometry of eight fibers was modeled for each fiber family (i.e. $m = 8$). The conductivity of the wires was that of annealed copper $5.8\times10^7\,\mathrm{Ohm^{-1}m^{-1}}$ (with a magnetic permeability of $\mu_{\mathrm{cond}} = 4\pi \times 10^{-7}\,\mathrm{H/m}$). Because FastHenry2 only supports conductors with rectangular cross-sections, square cross-sections were used with a cross-sectional area equal to that of a round conductor with a radius a of 1 mm. The excitation frequency (30 Hz, skin depth $\delta = 1.2\,\mathrm{cm} >> a$) was chosen to approximate a uniform current-density in the wires. The diameter D_α

of the α-family fibers was equal to that of the β fibers D_β (which was the actuator diameter D defined by Eq. (2.2)).

The inductance was calculated for values of η ranging from $\frac{1}{16}$ to $\frac{16}{16}$. The values of β incremented from -87 ° to 87 ° in 3 ° increments. The inductance was only calculated at angles that were feasible according to Eq. (2.27) with a fiber diameter D_{fiber} 1.5 times larger than the conductor diameter. The paths of the fibers in each family were assumed to originate at the same point at the base of the actuator (with m origin points shared by an α and a β fiber spaced evenly around the circumference of the base). The curved fibers segments were created with 50 nodes per turn. If a fiber made less than a tenth of one turn, five nodes were used.

3.4.2 Normalized Inductance Model

The values of inductance calculated in Section 3.4.1 correspond to the specific circuit configuration and geometry of the specified example. To generalize this result and understand the effect of design choices on the inductance, it is desirable to develop an inductance expression that depends explicitly on the design parameters. To this end, we developed a normalized inductance model that transforms the calculated inductance values from Section 3.4.1 into a general model of Smart Braid FREE inductance.

To accomplish this normalization, several assumptions must be made (in addition to the geometric assumptions made in the kinematic model). The first assumption is that the ratio of wire radius to actuator size is fixed. To understand the effect of this ratio, consider the inductance of a long, straight, round, non-magnetic wire [149]. The self-inductance L' is approximated by

$$L' = \frac{\mu b}{2\pi}\left[\ln\left(\frac{2b}{a}\right) - 1 + \frac{Y}{2}\right] \tag{3.1}$$

where b is the length of the wire, a is the wire radius, Y is related to the current distribution and μ is the magnetic permeability of vacuum. With uniform current ($Y = 0.5$), decreasing the wire radius from $a = b \times 10^{-3}$ to $a = b \times 10^{-4}$ results in a calculated self-inductance that is approximately 34 % higher. Geometric similarity must thus include the wire diameter.

The normalized model further assumes that the current is uniformly distributed in the conductor. This assumption neglects current distribution effects such as the skin effect and the proximity effect. When the skin effect dominates (at high frequencies), Y approaches zero. For a conductor radius $a = b \times 10^{-3}$, the high-frequency inductance ($Y = 0$) is only 4 % smaller than the inductance with uniform current ($Y = 0.5$).

It is also assumed that the magnetic field is approximately uniform around the circular perimeter, along the length of the cylinder, and through the thickness of the braided or layered conductors. These are common assumptions for long solenoid-like circuits. These assumptions are increasingly accurate for increased numbers of fibers m (uniformity around perimeter), increased sensor length relative to the sensor diameter (uniformity along length), and small radial spacing between the conductors (uniformity through thickness).

With these assumptions, a normalized inductance model for Smart Braid FREEs can be constructed. Assuming that the wire radius scales linearly with the sensor size allows the model to scale proportionally to D_0. By assuming equal flux in the circular cross-section, the inductance of the series configuration circuit is approximated to scale with the square m^2 of the number of fibers. The assumption of a uniform field along the length allows the inductance to be normalized by the number of turns $n_{0,\alpha}$. The assumption of a uniform field in the thickness allows us to ignore the braiding or layering of the conductors.

With these assumptions, the inductance of a Smart Braid FREE in a series con-

figuration L_s is approximated with the following expression

$$L_s \approx \mu m^2 D_0 n_{0,\alpha} \chi(\eta, \beta) = \frac{\mu m^2 b_\alpha}{\pi} \chi(\eta, \beta) \tag{3.2}$$

where μ is the magnetic permeability of the surrounding medium. χ is described in the subsequent paragraph. The parallel inductance L_p is related to the series inductance through the assumptions of symmetry and an m-th fraction of the current in the fibers. These assumptions lead to a parallel inductance value that is $1/m^2$ times smaller than the serial inductance value

$$L_p \approx \frac{\mu b_\alpha}{\pi} \chi(\eta, \beta)\,. \tag{3.3}$$

The expressions in Eqs. (3.2) and (3.3) are linearly scaled by a unitless function $\chi(\eta, \beta)$ which is solely a function of the type η and state β of the Smart Braid FREE. The inductance values calculated in Section 3.4.1 were normalized to approximate the value of the unitless function (Fig. 3.2). The calculated values of χ and the scripts used to generate the FastHenry2 input files are archived on the MATLAB file exchange [150]. Based on the assumptions of the model, using χ in Eqs. (3.2) and (3.3) will be most accurate when: the fibers are densely spaced around the perimeter, the wire radius is approximately $D_0 \times 10^{-2}$ and the sensor is "long" relative to its diameter. These expectations are validated in Section 3.4.3. The predictions of the numerical model are compared to experimental results in Section 3.4.4. The design discussion in Section 3.6 inspects the approximated values of χ to draw conclusions about the viability and design of Smart Braid FREEs.

3.4.3 Numerical Validation of Normalized Inductance Model

The χ-function provides valuable insight into the behavior of Smart Braid FREEs. Ideally, it only needs to be calculated once and can describe the behavior of a wide-

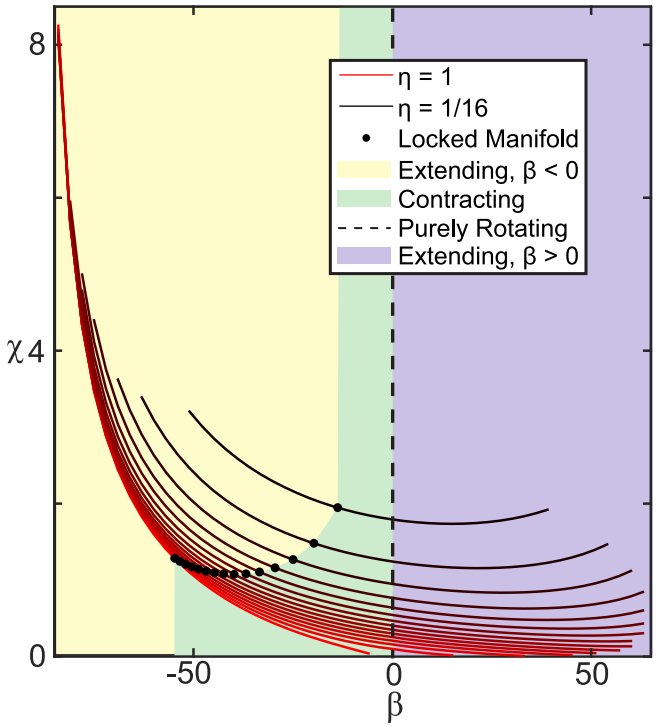

Figure 3.2: The inductance of a Smart Braid FREE scales linearly with the unitless function $\chi(\eta, \beta)$ that depends only on the type and state of the actuator (expressed by η and β). Smaller values of η result in higher values of χ for the same angle β. The "locked manifold" is the point of maximal volume for a given FREE type. When pressurized, the angle β of the actuator progresses towards the value of β at the locked manifold.

variety of Smart Braid FREEs independent of the other parameters. In practice, the inductance of Smart Braid FREEs will differ from the values predicted by Eqs. (3.2) and (3.3). The purpose of this section is to show the validity of the normalized model and provide rough quantitative bounds for the error between the normalized model and more accurate but computationally expensive direct simulations of the sensor geometry.

To this end, predictions from the normalized model were compared to inductance values simulated directly for different geometries and configurations. The directly simulated inductance values rely on the same procedure used to approximate χ (described in Section 3.4.1) but with select changes in parameter values. The error of the normalized model is quantified as the algebraic difference between the prediction of the normalized model and the result of the direct simulation. This error is normalized by the predicted inductance range of the normalized model. For example, a difference of $1\,\mu$H, with parameter values that lead to a predicted inductance range of $10\,\mu$H, corresponds to an error of 10 %. The results of this numerical validation are listed in Table 3.1.

Parameter Values used for the Normalized Model Serial Configuration, $D_0 = 10\,\text{cm}$, $a = 1\,\text{mm}$, $D_{\text{fiber}} = 1.5a$, $m = 8$, $n_{0,\alpha} = 10$, $f_{\text{excite}} = 30\,\text{Hz}$, $D_\alpha = D_\beta = D$					
Parameter Change		**Avg. Error**	**Max. Abs. Error** (% of range)		
Description	Quantity	(% of range)	Quantity	at β (°)	at η
Parallel configuration		-1.1e-08	-7.6e-07	0	5/16
Increasing D_0 and wire radius proportionally	$D_0 = 1\,\text{m}$, $a = 1\,\text{cm}$	-6.5e-08	2.1e-05	0	7/8
Increasing D_0 only	$D_0 = 1\,\text{m}$	-2.7	-4.1	-84	1
High frequency (skin depth $\delta << a$)	$f_{\text{excite}} = 30\,\text{Hz} \rightarrow \delta = 0.038\,\text{mm}$	7.8e-16	-3.5e-11	-81	1
Fewer (sparse) fibers	$m = 4$	-2.4	-4.1	-45	1
More (dense) fibers	$m = 12$	0.64	1.1	-45	1
Longer length	$n_{0,\alpha} = 15$	-0.33	-5.5	-84	3/4
Shorter length	$n_{0,\alpha} = 5$	0.88	14	-84	3/4
Very short length	$n_{0,\alpha} = 0.5$	7.1	72	-84	3/4
Layered fibers	$D_\alpha = D + D_{\text{fiber}}$, $D_\beta = D - D_{\text{fiber}}$	-0.88	-3.8	45	13/16

Table 3.1: Numerical Model Validation (Error shown is % of inductance range predicted by the normalized model)

The numerical results validate the assumptions of the model and provide bounds for the expected error as the sensor considered deviates from the parameter values used to approximate χ. The relationship between serial and parallel wiring con-

figurations is supported by the simulations. Additionally, scaling both the length and conductor radius together preserves the accuracy. Increasing only D_0 (without increasing the wire radius) leads to an under-prediction of the inductance by the normalized model. A high excitation frequency has virtually no effect. Using fewer fibers results in an under-prediction of the inductance by the normalized model. This difference is greatest then the fibers are furthest apart (e.g. $\eta = 1, \beta = -45°$). The relative magnitude of the error in the model is smaller when considering more fibers (compared to the consideration of fewer fibers). Similarly, increasing the length of the sensor results in less relative error than decreasing the length of the sensor. Evaluating shorter-length sensors with the normalized model tends to over-predict the inductance (due to the greater role of end-effects in the overall inductance). These effects are most pronounced at the most negative values of β. Layering the fibers results in inductance predictions that are at times larger and at times smaller than the inductance predicted by direct simulation. When the fibers are layered, the average difference is -0.88 % of the inductance range and the average *absolute* difference is 1.03 %

These results show that the scaling terms of the normalized model capture the trends of the inductance change across changes in parameter values. The largest errors observed for this validation were when the sensor length was small compared to the diameter. As β approaches -90 °, the length of a FREE approaches zero while its diameter approaches D_0. Thus, in this region, the assumption of a "long" circuit breaks down. When evaluating different sensor lengths with the same value of D_0, the largest divergences between the model and the numerical simulations occurred at the lowest values of β. This limits the usefulness of the model in predicting accurate inductance values as β approaches -90 °.

This validation has other limits. While the error in inductance prediction often deviates by only a few percentage points of the inductance range, at a given point it

is often many times larger or smaller than the inductance values predicted by direct simulation. Thus, the model provides a valuable way to predict the effects of the parameters but is not the most accurate way to predict specific inductance values. Moreover, the error quantified in this validation does not capture error from other assumptions of the model. It does not quantify the effect of non-cylindrical motions such as bending and diametrical tapering at the ends of an actuator. Nor does it capture the effect of braided wires, electrical junctions between the helices or nearby metal.

3.4.4 Experimental Validation of Normalized Inductance Model

The numerical validation of Section 3.4.3 supports the use of the normalized model in early design in lieu of computationally expensive direct numerical simulation. Section 3.4.3, however, does not provide direct evidence for the agreement between the predictions of the normalized model and experimental results. This section compares the model to inductance measurements from a physical prototype.

The sensor consisted of eight fibers in each family connected in series with $\eta = 1$, $b_\alpha = b_\beta = 34\,\text{cm}$ and number of turns $n_\alpha = n_\beta = 3.375$ ($D_0 = 3.2\,\text{cm}$). The radius of the conductor was $a = 0.42\,\text{mm}$. The braid was created by weaving wire over a 3D-printed template. The template was printed with "ABSplus" from a Stratasys Dimension Elite printer. The template was designed to affix to a dowel during the braiding process. After the braid was completed, the dowel was removed and the template was collapsed and removed from within the braid. The wire used had soft copper stranding and PVC insulation with a conductor area of $0.33\,\text{mm}^2$ (22 AWG, DABURN, #2671, Outer diameter 1.346 mm). A single strand of wire was woven to form the entire braid.

For the model validation experiments, the Smart Braid sensor was only a wire braid, with no inner, elastomeric bladder. This allowed the sensor to maintain the

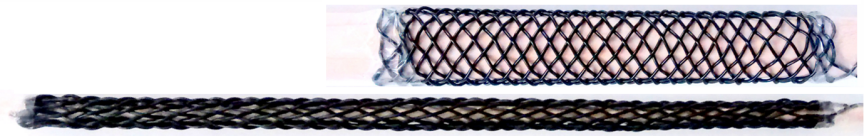

Figure 3.3: The model was compared to measurements from a Smart Braid stretched over dowels of different diameter.

cylindrical shape assumed by the long solenoid equation. The length was changed by stretching the braid over a series of cores with different diameters (Fig. 3.3). Wooden dowels were used because they are non-magnetic with a magnetic permeability that is practically identical to that of vacuum. Seven dowels were used with the following nominal diameters: 6.35 mm, 9.53 mm, 12.70 mm, 15.88 mm, 19.05 mm, 22.23 mm, 25.40 mm. The braid was stretched over each dowel three times. The 21 trials were conducted in random order. In each trial, the length of the braid was measured once and 100 inductance measurements were taken. The inductance of the braid was measured with an LCR meter (NI PXI-4072) with an effective excitation frequency of 30 kHz and a maximum sampling rate of 40 Hz [151]. The LCR meter works by comparing the magnitude of the sensor impedance at low and high frequencies [152]. Test stand sensor measurements and control signals were processed with a data acquisition unit (NI PXIe-6341). The LCR meter and data acquisition unit used a PXI express chassis (NI PXIe-1073) to communicate with custom scripts in LabVIEW.

The radial thickness of the sensor was approximated as two wire outer diameters (2×1.346 mm). Thus the diameter used to identify the β for Eq. (3.2) was the inner diameter plus two wire outer diameters. The scaled predictions of Eq. (3.2) were compared against the experimentally recorded inductance values. The experimental validation (Fig. 3.4) resulted in an average absolute error of only 7.8 %. The model also predicted the sensitivity to length change with an error of only 10 %. The sensitivity comes from a linear regression against the data.

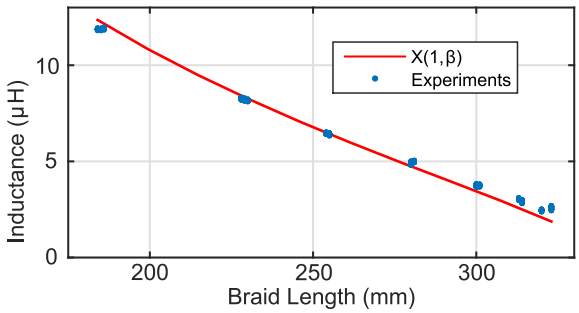

Figure 3.4: The normalized inductance model for Smart Braid FREEs (χ, red line) predicted the inductance of the experimental sensor (blue dots) with an average absolute error of only 7.8 %. The model also predicted the sensitivity to length change with an error of only 10 %.

The accuracy of the experimental results comes from similarity to the assumptions of the model and the parameters values used to approximate χ. The wires of the experimental sensor were relatively densely distributed around the circumference and their number, eight, was the same as the sensor modeled for χ. The experimental sensor also had a relatively long length compared to its diameter. Though the size of the experimental sensor differed from the size of the sensor used to approximate χ, the ratio of D_0 to the conductor radius was roughly the same ($a = 1.3D_0 \times 10^{-2}$ in the experiments and $a = 1D_0 \times 10^{-2}$ for the χ approximation). The sensor was also tested in strictly cylindrical conditions (as is assumed by the kinematic model). One important difference between the prototype and the model is the braided conductors used on the experimental sensor.

3.5 Resistance

The ability to measure the inductance of a circuit can be limited by high levels of electrical resistance. To understand how well the changes in inductance can be measured, this section presents a model of the resistance of Smart Braid circuits and the effect of the design parameters on the resistance.

The series resistance R_s is

$$R_s = \frac{m\rho}{A_{\text{cond}}}\left(b_\alpha + b_\beta\right) = \frac{m\rho b_\beta}{A_{\text{cond}}}\left(\frac{1}{\eta} + 1\right) \tag{3.4}$$

where A_{cond} and ρ are the cross-sectional area and resistivity, respectively, of the conductive material in each fiber. The resistance R_p of the parallel circuit is

$$R_p = \frac{\rho}{mA_{\text{cond}}}\left(b_\alpha + b_\beta\right) = \frac{\rho b_\beta}{mA_{\text{cond}}}\left(\frac{1}{\eta} + 1\right). \tag{3.5}$$

Thus the series resistance is larger than the parallel resistance by a factor of m^2.

At high excitation frequencies, the skin effect can increase the real portion the circuit's AC impedance. When the skin depth δ is much smaller than the conductor radius a, the high-frequency resistance R_{HF} increases inversely proportional to the skin depth

$$\delta = \sqrt{\frac{2\rho}{2\pi f_{\text{exite}}\mu_{\text{cond}}}}, \text{ for } \delta << a \;\; R_{HF} = \frac{a}{2\delta}R \tag{3.6}$$

where f_{exite} is the excitation frequency (Hz), ρ is the resistivity of the conductor and μ_{cond} is the magnetic permeability of the conductor.

3.6 Design Discussion

The models of inductance and resistance can be used to explore design choices for Smart Braid FREEs. In particular, the inductance model provides insight into which combinations of η and β values yield useful sensing and actuation properties. The effect of the design parameters on sensitivity, quality, range-of-motion, manufacturability and fiber stress is also explored. For emphasis, some of the resulting design principles are highlighted in italics.

Since the inductance of a Smart Braid FREE is directly proportional to the function $\chi(\eta, \beta)$, inspection of this function can provide insight into Smart Braid FREE

design (Fig. 3.2). The following list highlights combinations η and β and discusses their usefulness for sensing and actuation. Recall that when $\eta = 1$ there is no rotation and β is always less than zero. When $\eta < 1$, the actuation includes rotation.

- $\beta < \beta_{LM}$**, Extending,** $\eta \approx 1$**, (Brighter red lines over yellow, Fig. 3.2):** The opposite chirality (handedness) and high turn-density of the fibers results in large overall inductance values, a monotonic inductance-to-length relationship and a high sensitivity to changes in actuator length. *Inductance measurements from Smart Braid actuators in this region are very good proxies for the actuator length.*

- $0 > \beta > \beta_{LM}$**, Contracting,** $\eta \approx 1$**, (Brighter red lines over blue-green, Fig. 3.2):** Compared to the previously considered $\beta < 0$ extension region, these actuators exhibit greater force-per-unit-pressure (for the same diameter and η-value) [136]. Though the overall inductance and sensitivity is smaller than the $\beta < 0$ extension region, the inductance-to-length relationship is still monotonic. *Accordingly, the length of these Smart Braid FREEs is easy to measure through the inductance.*

- $0 > \beta$**, Extending or Contracting,** $\eta \approx 0$**, (Darkest red line over blue-green and yellow, Fig. 3.2):** The inductance is dominated by the contributions of the high-turn-density α fiber family. The sensitivity to changes in β becomes very small as β approaches zero. *For these low values of η, Smart Braid sensing is better-suited for measuring pressurized extension than contraction.*

- $\beta = 0$**, Purely Rotating, (Dashed vertical line, Fig. 3.2):** The torque-per-unit-pressure is highest from actuators for which η is close to 1 [136]. The greatest relative inductance sensitivity to rotation (normalized by the current inductance value) also occurs when η is close to 1. These high values of η,

however, are characterized by low overall inductance which lowers the sensor "quality." *Accordingly, it may only be possible to coarsely measure pure rotation.*

- $\beta > 0$**, Extending, (Lavender, Fig. 3.2)**: The inductance-to-length relationship in this region is non-monotonic. The highest sensitivities are seen for small values of η at large values of β. *For much of this region, Smart Braids do not provide useful measures of the actuator state.*

In addition to the geometric response, the sensitivity of inductance to actuation depends on the wiring configuration. In the serial configuration, the sensitivity increases with the square of the number of fibers (i.e. m^2). In the parallel configuration, the sensitivity is smaller and independent of the number of fibers. *Thus to maximize the absolute inductance sensitivity, a serial configuration should be used with as many fibers as possible.* This may be desirable, for instance, when the inductance of the lead wires is unknown or subject to change.

When measuring inductance through the frequency of a resonant circuit, the absolute change in frequency is related to the relative change in the inductance. *The relative change in inductance does not depend on whether the fibers are wired in series or parallel.* Instead, it scales with the value of $\chi(\eta, \beta)$ and its derivative $\frac{d\chi}{d\beta}$.

The "quality factor" Q of a Smart Braid circuit is the ratio of the inductive reactance to the electrical resistance

$$Q = \frac{1}{2\zeta} = 2\pi f_{\text{exite}} \frac{L}{R}. \tag{3.7}$$

Neglecting the skin and proximity effects, the quality factor for the series circuit Q_s is found by substituting Eq. (3.4), Eq. (2.5) and Eq. (3.2) into Eq. (3.7). The quality factor for the parallel circuit Q_p is derived similarly using Eq. (3.5) and Eq. (3.3).

The quality factor of the two wiring configurations is the same:

$$Q_s = Q_p = \frac{2 f_{\text{exite}} \mu m \chi(\eta, \beta)\, A_{\text{cond}}}{\rho \left(1 + \frac{1}{\eta}\right)}. \tag{3.8}$$

To maximize Q, the excitation frequency should be as high as possible. The upper limit of the excitation frequency is often imposed by the electronics characterizing the inductance or the parasitic capacitance [153]. For a fixed excitation frequency, it is desirable to maximize the ratio of the inductance to the resistance. The quality factor increases with lower material resistivity ρ, but this is bounded by the available materials. Introducing a ferromagnetic core can increase μ but can also introduce hysteresis and eddy current losses that reduce the overall quality factor. Thus, *to maximize the quality factor, the cross-sectional area of the conductor in each fiber A_{cond} and the number of fibers in each family m should be increased.*

There are limits, however, to increasing the conductor radius and the number of fibers. Increasing the conductor radius has diminishing returns as the size of the radius approaches and exceeds the skin depth (see Eq. (3.6)). Increasing the number of fibers can also increase the parasitic capacitance of the circuit (and thus limit the excitation frequency) [153].

Increasing the conductor radius and the number of fibers can also limit the range of motion of the actuator. To maintain a desired range of motion, the product of the fiber outer diameter and the number of fibers must be kept below certain levels. Because the conductor area scales with the square of the fiber diameter, *increasing the fiber diameter preferentially over the number of fibers can help increase the quality factor without restricting the actuator range of motion.*

FREEs and McKibben muscles are typically wound or braided from many disconnected fibers. To form a circuit, the helices must be connected together. To create a serial configuration, each α fiber end must be connected to a β fiber end such that a

single circuit is formed that includes all the fibers in series. The number of required electrical nodes for the series circuit scales with the number of fibers. The relative positions of the fibers that need to be connected will change with the length of the FREE. This makes forming a series circuit in an automated process difficult. In the parallel configuration, however, only three electrical nodes are needed–one connected to the proximal ends of all the α fibers, one connecting the distal ends of all the α and β fibers, and one for the proximal ends of the β fibers. Thus, *from a manufacturing perspective, the parallel configuration is much simpler than the series.*

The fibers of a FREE must also bear the stress of actuation. *Using more fibers and/or larger cross sections of stress-bearing material reduces the material stress.* Fibers could be made from high-tensile-strength conductors such as aluminum or from a combination of conductive and high-tensile-strength material. Models of fiber stress in two-fiber-family FREEs are the subject of current investigation. Care needs to be taken to prevent stress-induced fatigue and failure.

3.7 Conclusions

This chapter demonstrates that inductance-based "Smart Braid" sensors can be used to sense the motion of soft cylindrical actuators known as Fiber Reinforced Elastomeric Enclosures (FREEs). The changing geometry of fibers allows one to measure actuated motion via changes in the Smart Braid inductance. This chapter develops a normalized inductance model and a resistance model for two-fiber-family Smart Braid FREEs. The inductance model was validated numerically and against existing experimental data.

The purpose of the inductance and resistance models is to provide insight into the effects of design choices and to reveal which types of Smart Braid FREEs are useful for sensing and actuation. The inductance model relies on a numerically identified dimensionless function $\chi(\eta, \beta)$. This function depends only on the ratio η of the fiber

lengths and the angle β of one of the fiber families. One of the main contributions of this chapter is the approximation, presentation and analysis of this function. Inspection of the function reveals important conclusions about Smart Braid sensing. For example, FREEs exhibit the greatest inductance sensitivity to length change when $\beta < \beta_{LM}$ and $\eta \approx 1$. Overall, the greatest inductance sensitivities are achieved when the fiber families have different chirality (i.e. handedness). When the chirality is the same, the inductance response may exhibit low sensitivity and have a non-monotonic relationship to the actuator stroke progression. When measuring pure rotation, there is a trade-off between inductance magnitude and sensitivity. The highest inductance values are achieved for low values of η, but the greatest relative sensitivities are achieved with η values that approach 1. This suggests it may be difficult to precisely measure the state of purely rotating FREEs with Smart Braid sensors.

The quality factor of Smart Braid sensors increases with the number of fibers and the cross-sectional area of the conductors. It is unaffected, however, by whether the conductors are connected in series or parallel. One advantage of a parallel configuration is that it can be manufactured more easily with an automated process.

The inductance model presented in this chapter is currently limited to approximating purely cylindrical sensors. It is expected to be most accurate for long sensors with a D_0-to-conductor-radius ratio on the order of 10^2 and relatively dense fiber spacing. It neglects the effects of tapering diameters and bending that can occur in physical actuators. The model accurately predicted the inductance of a similar experimental prototype with an average absolute error of only 7.8 %. The experimental validation was limited to the case of $\eta = 1$ (McKibben muscle).

The results of this chapter suggest that Smart Braids should be able to accurately measure the motion of many kinds of FREEs. The type of FREE with the most widespread use is the contracting McKibben muscle actuator. The results of the inductance model suggest that Smart Braid sensing should be well-suited for this

style of actuator. The following chapter experimentally tests the ability of Smart Braids to measure the length of these actuators.

CHAPTER IV

Experimental Evaluation of a "Smart Braid" McKibben Muscle

4.1 Introduction

The most common Fiber-Reinforced Elastomeric Elastomeric Enclosure is the Mckibben muscle (also known as a Pneumatic Artificial Muscles or PAM). These actuators contract along their length like biological muscles [154] without rotation.

PAMs, like other fiber-reinforced actuators are compliant and force-dense. They can create ten times the pulling force of a traditional pneumatic cylinder of the same diameter [155] without the friction of sliding seals. The compliant and sealed structure of PAMs allows them to be used without the precise alignment or protection from the elements that servomotors require. These properties of PAMs have led to a variety of applications. Their force density makes them useful in bio-mimetic robots that jump and run [58], [156]. Their compliance makes them attractive for use in robots with soft joints or in continuum robots without any discrete joints at all [30]. OctArm, for

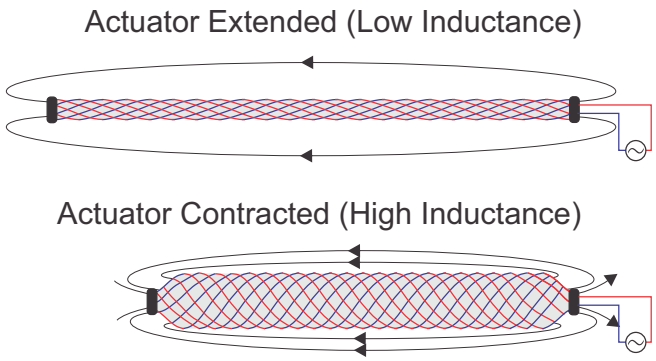

Figure 4.1: By using wire in place of the typically-non-conductive fibers of a pneumatic artificial muscle, one can create a "Smart Braid" that senses the contraction of the actuator. This is accomplished by measuring the inductance of the circuit formed by the wires in the braid. As the actuator contracts, the increasing alignment of the wires leads to a higher inductance. ©2016 IEEE

example, is a trunk-like manipulator that uses triplets of extending PAMs to create bending in sections of its length [66]. The ability of PAMs to function without rigid linkages or precise alignments has led to widespread application in powered orthoses and exoskeleton devices [44]–[46].

In robotic applications, it is necessary to pair the PAM actuators with sensors to allow for closed-loop control of the generated motions. Traditional encoders, however, have limited usefulness in many PAM-actuated robots. Traditional encoders need to be kept clean and dry. They need to be coupled to rigid mechanical joints. These conditions are not always available in robots that rely on PAM actuators. For instance, it would be beneficial if PAM-actuated running and walking robots could operate in muddy and wet environments. Though the PAMs themselves have no need to remain clean and dry, attempts to shield the encoded joints can add weight, complexity, and cost. Similarly, traditional encoders are designed to be connected to single-degree-of-freedom, rigid mechanical joints. Soft robots often do not offer such convenient coupling points.

Clearly, actuators that could sense their own contraction or extension state would be very valuable. Such actuators could provide position feedback with compliant joints and in continuum robotic devices. An extensive review of technologies that could accomplish this is provided in Section 1.2 of the introduction to this dissertation.

In this chapter, a McKibben muscle actuator is fabricated with a Smart Braid forming its reinforcing fibers. The wires of the Smart Braid form a circuit in such a way that the current circles the axis of the actuator as if it was a solenoid (Fig. 4.1). When the actuator contracts, the current vectors in the wires become more aligned and the inductance of the circuit increases.

The simplest way to consider the change in inductance is to approximate the circuit as a long solenoid. Its inductance can then be approximated by

$$L = \mu \frac{N^2 A}{l}, \tag{4.1}$$

where μ is the magnetic permeability of the core and N is the number of turns. A and l are the cross-sectional area and the length, respectively. When a McKibben muscle is pressurized, its volume increases. The reinforcing fibers cause the length of the actuator to decrease as its cross-sectional area expands. Because the ends of actuator have no relative rotation during actuation, the number of turns remains constant. The shortening and widening of the actuator lead to an increase in inductance. This makes the inductance of the circuit sensitive to the contraction of the actuator–with the inductance more than doubling over the course of a full contraction.

This chapter demonstrates how a simple, linear calibration of inductance can be used to measure contraction of a McKibben muscle in quasistatic, loaded, and dynamic conditions. The results show that the actuator contraction (57 mm stroke) can be measured with a linear function of the inductance ($R^2 = .9996$). A large load applied to the actuator (5 kg), resulted in only a millimeter of sensor bias. The sensor

performance did not degrade at actuation frequencies up to 4 Hz.

4.2 Actuator Testing Methods

4.2.1 Fabrication and Instrumentation

A complete McKibben muscle actuator was fabricated by affixing a Smart Braid sensor over a flexible silicone tube. The sensor was fabricated according to the process described in Chapter III. In addition to sensing contraction, the fibers of the Smart Braid reinforce the elastomeric bladder and cause the actuator to contract as the pressurized air pushes the volume of the bladder to expand. The sensor performance was tested under loaded and dynamic actuator contractions. The Smart Braid was stretched over a silicone tube with a 9.53 mm outer diameter (6.35 mm inner diameter) and connected to the test stand. The hose clamps required to attach the Smart Braid actuator to the test stand reduced the length of active, fully-extended portion of the actuator to 29 cm.

The actuator was evaluated in a custom-made test apparatus in which different pressures and loads were applied while both inductance and the ground truth actuator contraction were measured. Pressure control was achieved with a custom feedback loop driven by a proportional valve (Enfield LS-V05s) and a pressure transducer (WIKA A-10). Contraction of the actuator was measured from the motion of a sliding carriage affixed to the actuator end. A string potentiometer was used to measure the position of the carriage (UniMeasure LX-PA, 10" range). Figure 4.2 shows the test-stand assembled with the actuator. The inductance was measured with the same LCR meter described in Chapter III.

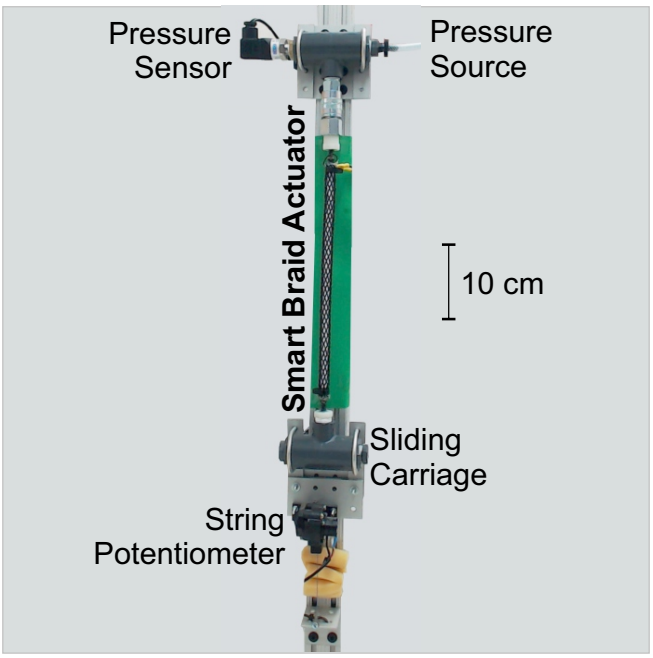

Figure 4.2: A custom-made test stand was used to characterize the inductance-length relationship of the Smart-Braid actuator. The actuator is contracted by filling the inner bladder with pressurized air. The top side of the actuator is fixed and the bottom is attached to a sliding carriage. Weights can be attached to the carriage to load the actuator. The inductance of the Smart Braid was measured with an LCR meter. A ground truth measurement of contraction is obtained from a string potentiometer attached to the carriage. ©2016 IEEE

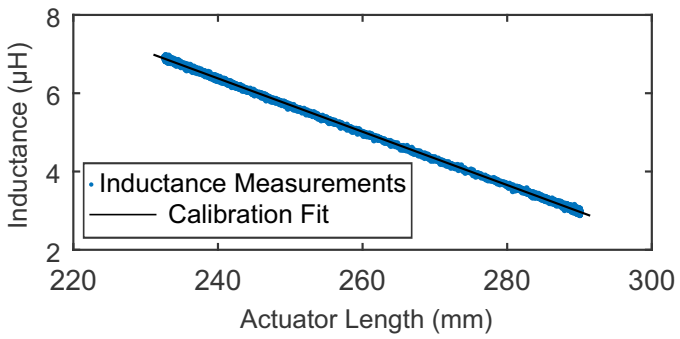

Figure 4.3: The experimental calibration data was fit with a linear function ($R^2 = 0.9996$). ©2016 IEEE

4.2.2 Sensor Calibration

To calibrate the sensor, inductance measurements were collected while the gauge pressure in the actuator was increased gradually to 0.34 MPa (49 psi) and then decreased to atmospheric levels over the course of 200 seconds. The shortest recorded actuator length was 232.5 mm which corresponds to a contraction of approximately 20 %. To calibrate the sensor, the inductance measurements taken during the contraction and extension cycle were fit with a linear regression to the actuator length measured with the string potentiometer attached to the sliding carriage. Figure 4.3 shows the inductance and position measurements taken during the calibration and their linear regression. The calibration resulted in a strong linear fit ($R^2 = 0.9996$). The linear function predicting the actuator length l (in millimeters) from the inductance measurements L (in henries) is given by

$$l = -14.68 \times 10^6 L + 333.628. \tag{4.2}$$

This corresponds to a sensitivity of -6.81×10^{-8} $^{\mathrm{H}}/_{\mathrm{mm}}$.

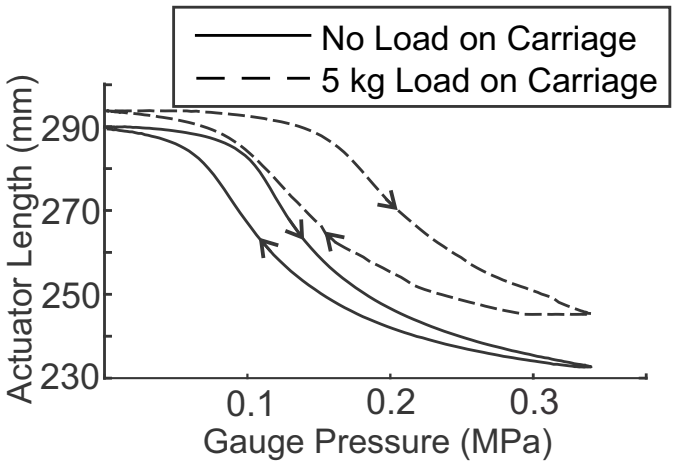

Figure 4.4: Adding an end-load to the actuator decreases the actuator contraction that can be achieved with the same pressure. This behavior is similar to other actuators of this kind [155]. ©2016 IEEE

4.2.3 Sensor Performance Verification

4.2.3.1 Loaded Conditions

To evaluate how an end-load would affect the correlation between the lengths predicted by the Smart Braid and the length measured at the sliding carriage, the actuator was tested with a series of weights (0 to 5 kg in 1 kg increments) attached to the sliding carriage. The contraction of the actuator was driven by the same pressure sequence used in the calibration. The load caused the degree of contraction to decrease under the same pressure conditions. The pressure contraction relationship is illustrated in Fig. 4.4 for the no load and 5 kg tests. After the 5 kg test, the actuator was again tested without any weight. Thus a total of seven weight trials were conducted. In each weight condition, the mean and standard deviation of the error is calculated. The error is the difference between the length calculated by the inductance of the Smart Braid and the length measured at the sliding carriage.

4.2.3.2 Dynamic Conditions

To evaluate the usefulness of the Smart Braid under dynamic actuation conditions, the performance of the sensor was evaluated at a series of actuator contraction frequencies. The contractions were driven by sinusoidal pressure profiles. The gauge pressure was first varied between approximately 0.013 MPa and 0.33 MPa at a frequency of 0.25 Hz for 20 seconds. The frequency was then increased in 0.25 Hz increments up to 4 Hz. At each frequency setting, data was collected for 20 seconds. Because inductance measurements were not available more frequently than 40 Hz, the actuator frequency was not increased beyond 4 Hz. Valve flow limitations caused the magnitude of the pressure change to decrease gradually as the frequency increased. The gauge pressure at the highest frequency varied between approximately 0.14 MPa and 0.2 MPa. The frequency response of the Smart Braid inductance measurements to the actuator length (as measured at the sliding carriage) was characterized at the test frequencies using spectral analysis in MATLAB's System Identification Toolbox. Only one dynamic sequence was performed.

4.3 Actuator Testing Results

Over the course of the actuator contraction, the inductance of the Smart Braid increased from 2.96 μH to 6.88 μH. Repeating the calibration conditions (Fig. 4.5, 0 kg) resulted in a measurement error with a standard deviation of 0.83 mm. The fit of the linear regression to the calibration data is excellent ($R^2 = 0.9996$). The residual of the calibration is defined as the difference between the calibration measurements and the calibration fit. The standard deviation of the residual was 0.48 mm. Moreover, the sensitivity of this calibration is only 8 % smaller than the sensitivity predicted by the inductance model proposed in Chapter III.

When loads were added to the carriage, a slight difference was observed between

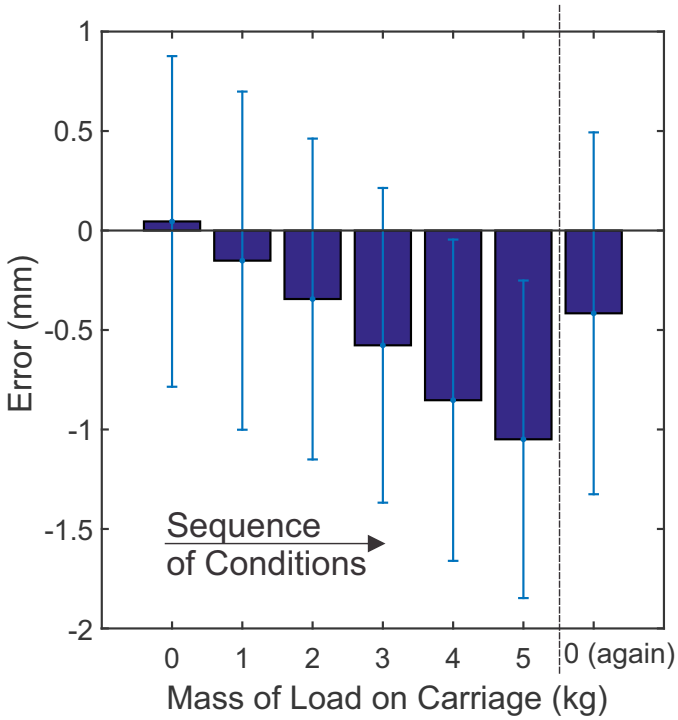

Figure 4.5: Increasing the load on the sliding carriage to 5 kg caused the inductance-based measurements to diverge slightly from the string-potentiometer readings. This is potentially due to compliance in the connections between the actuator (where the inductance of the Smart Braid is measured) and the sliding carriage (where the string potentiometer is attached). Shown are means of the error plus/minus a single standard deviation. When the load was removed, some bias remained. ©2016 IEEE

the length calculated by the Smart Braid inductance measurements and the length measured at the sliding carriage. This difference increased with the load. At the highest load (5 kg) the mean error between the sensors was -1.05 mm. When the no load condition was repeated after the 5 kg test, the mean error between the sensors was -0.41 mm. Figure 4.5 illustrates this sensor bias. Figure 4.6 shows the deviation between the sensor measurements in the 5 kg condition.

The dynamic tests showed virtually no phase lag or change in magnitude response for frequencies up to 4 Hz. A bode plot of the spectral analysis of the Smart Braid sensor response is shown in Fig. 4.7. The uncertainty of the magnitude response increased as the samples per cycle became sparser. A representative snippet of the

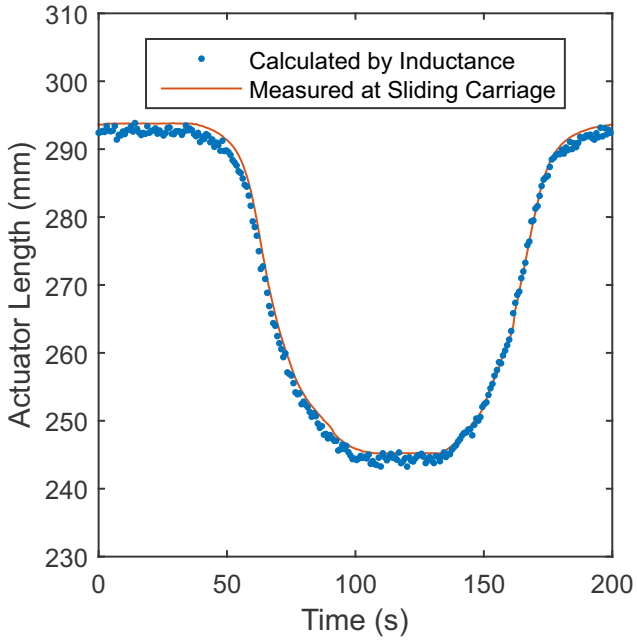

Figure 4.6: Shown are a series of measurements during the contraction-extension cycle with a 5 kg load. The Smart Braid reliably reports position with an average error of 1 mm. ©2016 IEEE

sensor measurements at 4 Hz is shown in Fig. 4.8. A video with portions of the dynamic test is included in the supplementary materials.

4.4 Discussion and Conclusions

One goal of this chapter is to experimentally demonstrate the use of a Smart Braid to sense the contraction of a McKibben muscle actuator. The Smart Braid tested was able to measure the actuator contraction to within about a millimeter in dynamic and loaded conditions. This was accomplished without any additional mechanical components. The electrically conductive circuit formed by the fibers is the only difference from a standard McKibben muscle. Despite this simplicity, the contraction can be accurately measured with only a linear calibration of the inductance measurements. The Smart Braid can provide measures of length at contraction frequencies beyond the typical bandwidth of PAM actuators [157]–[159].

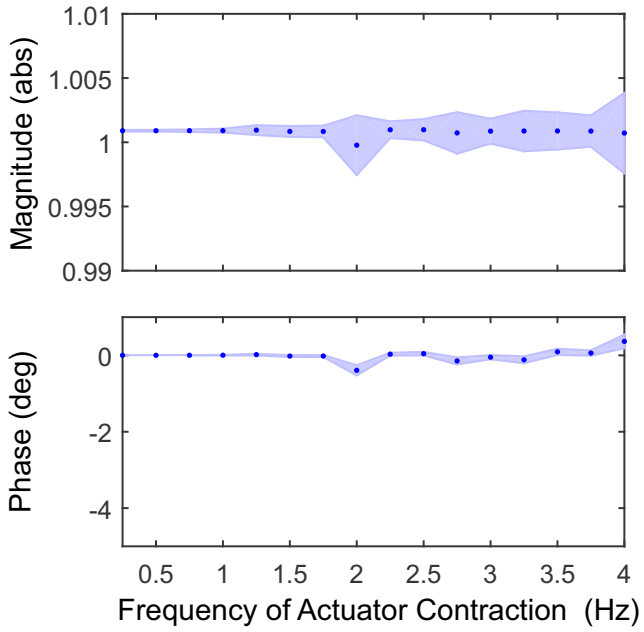

Figure 4.7: The Smart Braid sensor provides accurate measurements over a broad dynamic range. For frequencies up to 4 Hz there is neither substantial attenuation nor phase lag. The dots show results of a spectral analysis at 16 different frequencies. The lightly shaded bands show the bounds corresponding to three standard deviations. ©2016 IEEE

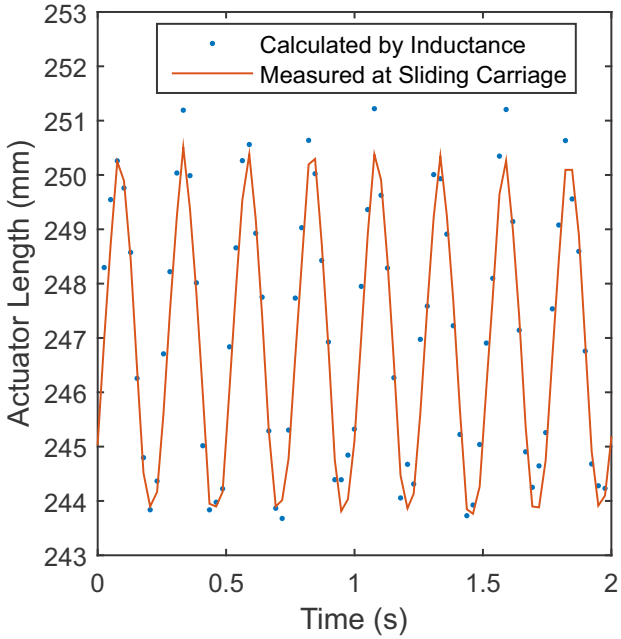

Figure 4.8: Even at rapid actuator contractions, the Smart Braid sensor provides a reliable length measurement. No phase lag or attenuation can be observed even at the 4 Hz excitation frequency shown here. ©2016 IEEE

With a 5 kg load, a bias of approximately 1 mm was observed between the actuator-level measures of the Smart Braid and joint-level measurements. This may be caused by compliance in the actuator connections. Not all of this stretching was recoverable; after the mass was removed, the sensor still exhibited a half-millimeter bias. Stretching in the connections is a weakness of any actuator-level sensing method. There are several possible ways to resolve this. The first is to make the connections as stiff as possible. Another way is to use redundant sensor measurements. PAMs are commonly used in antagonized configurations. An antagonized pair would provide a degree of sensor redundancy to help correct for the small biases. Finally, one could compensate for the bias by measuring the magnitude of the end-load. This can be achieved, for example via a pressure sensor. Alternatively, the resistance-strain relationship of the Smart Braid wires could measure the actuator force output directly [3], [160].

The inductance models of the previous chapter do not model the effect of the hose clamps on the Smart Braid or the resulting tapering at the ends of the actuator. Despite this, the sensitivity of the actuator was only 8 % smaller than the sensitivity predicted by the inductance model of Chapter III. The diameter constraints of the hose clamps and the tapering of the diameter did not greatly affect the predictive ability of the proposed models because only about 16 % of the actuator had a tapered or constrained diameter (3.77 cm tapered and 1 cm constrained of the 30 cm braid). For these effects to be considered in the future, the geometry could be specified and directly simulated to predict the inductance.

The results of this chapter suggest that Smart Braid actuators will be useful for robotic devices. One of the issues that became clear through the experiments of this chapter is the biasing effect that elasticity in the actuator connections can have. In the subsequent chapter, Smart Braid actuators are further evaluated as feedback for soft robotic systems. The effect of the connector elasticity is modeled and compensated for. Another issue with the actuators tested in this chapter is the direct exposure of the wires to the stress of actuation. The ordinary flexible used are not ideal for cyclic exposure to high tensile stresses. The manual fabrication process for the Smart Braid was also extremely slow (on the order of 8 hours). The conclusion of the dissertation discusses these issues and possible solutions.

CHAPTER V

Using "Smart Braid" McKibben Muscles for the Feedback Control of Soft Robotic Systems

Adapted from Wyatt Felt, Khai Yi Chin, and C. David Remy. "Smart Braid Feedback for the Closed-loop Control of Soft Robotic Systems". *Soft Robotics*. 2017.

Adapted with permission from SOFT ROBOTICS, published by Mary Ann Liebert, Inc., New Rochelle, NY

5.1 Introduction

The motion of many soft systems is often controlled in a purely open-loop fashion [25]–[27] or through manual teleoperation [28]. In some systems, the primary objective may be to exert forces on the environment with little concern for the robot pose. In other systems, such as manipulators, measuring and controlling the robot pose is essential. Open-loop control can be very effective if the system is well-known, no external disturbances are present, and positional accuracy is not imperative. The approach fails, however, if the system is subject to unknown forces or constraints from the environment, or if one cannot obtain a precise system model or is unable to invert this model due to hysteresis or other nonlinear effects [161]. To perform motion control under such circumstances, closed-loop feedback becomes imperative.

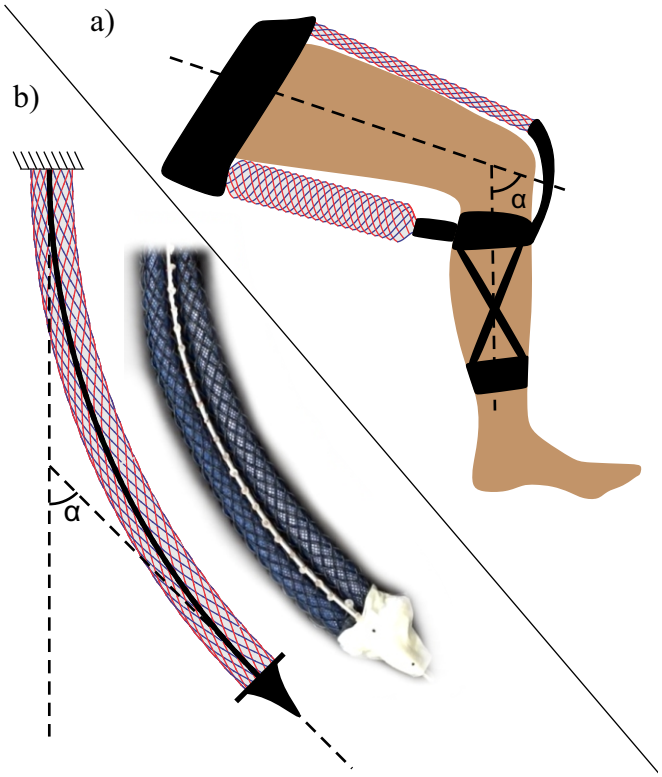

Figure 5.1: Shown are two examples of soft robotic systems: a) a soft orthosis that assists in creating torques about a human knee and b) a one degree of freedom continuum manipulator. In each case, the systems are not readily sensed by traditional, rigid sensors. The present work proposes the use of soft, flexible sensors to provide feedback control for systems like these. In particular, pneumatic McKibben muscles are used with inductance-based "Smart Braid" sensors on their exterior to measure actuator lengths. Closed-loop feedback was enabled and experimentally evaluated in the control of two bench-top systems analogous to those depicted here.

As the field of soft robotics matures, there is consequently an increasing interest in transforming soft *mechanisms* into soft *robots* that can measure and control their own motion [41]–[43], [50], [51], [71].

Despite recent advances, practical closed-loop motion control of soft robotic systems remains a challenge [14], [19], [30]. The pose of many soft systems is difficult to measure with sensors common to rigid robots such as rotary and linear encoders. Soft robotic systems rarely provide convenient coupling points for such sensors. For example, the control of a soft, assistive device (Fig. 5.1a) might require sensing of

human joint motion where the joint cannot be accessed directly. For a continuum manipulator, the problem is even more challenging, as motion is distributed throughout the entire system and no discrete joint axis exists (Fig. 5.1b).

In this chapter, flexible sensors built into the structure of soft actuators are used to provide feedback for the motion control of two soft robotic systems. The first system was a revolute joint (Fig. 5.2). This allowed the rigorously comparison of the efficacy of feedback from the proposed sensors to that from a rotary encoder. This system is also an example of applications with a well-defined joint axis, yet in which the joint angle is difficult to measure; for example, in an assistive robotic device for an elbow or knee joint (Fig. 5.1a). The second system tested was a planar, one degree of freedom continuum manipulator (Fig. 5.1b). This system highlights the ability of flexible sensors to enable the motion feedback control of systems without rigid joints.

The soft robotic systems evaluated here were driven by McKibben muscles. McKibben muscles consist of an elastomeric bladder surrounded by a braided sheath [142], [162]. The braided sheaths shape the expansion of the elastic bladder into a forceful contraction. McKibben muscles' soft nature and high force density has led to their widespread application in human-assistive devices [44], [46], [47], [61], [135]. They have also been successfully employed in a range of continuum manipulators [66], [163], [164].

In this chapter, the length of each McKibben muscle was measured with Smart Braid sensors. The Smart Braid sensors used in the present work were fabricated according to the process outlined in Chapter IV. To improve the fatigue life of the sensors, the wires of the Smart Braid were isolated from the stress of actuation. This was accomplished by using an inner, PET braid that reinforced the bladder against the internal pressure. The sensor braid was added over the top of this plastic braid. Both braids had similar fiber angles to create a similar contraction behavior.

This chapter presents the first demonstration of Smart Braid inductance sensors

in the feedback control of robotic devices. Section 5.2 includes the model, methods, and results of the revolute joint system. Here, a method is proposed to compensate for compliance between length-sensing actuators (Smart Braid or otherwise) and the motion output. Section 5.3 consists of a similar series of experiments on the continuum manipulator. Section 5.3 also includes a model for Smart Braid sensors on continuum segments. Section 5.4 contains general discussion and conclusions.

5.2 Revolute Joint

The first example studied was a one degree of freedom revolute joint driven by antagonized McKibben muscles (Fig. 5.2). Smart Braid measurements of actuator length were used as feedback to control the joint angle. The controller actively compensated for the compliance in the actuator connections. The performance of this Smart Braid feedback controller was then compared to the performance of a similar controller that used feedback from a rotary encoder. This allowed a rigorous evaluation and comparison of the proposed Smart Braid feedback.

In the test fixture of the revolute joint, two Smart Braid McKibben muscles (Fig. 5.2) rotated a load via steel cables and a pulley with radius r =25.4 mm (Fig. 5.4). The torque τ exerted on the load by the actuators was proportional to the difference between the two antagonized actuator forces, F_1 and F_2 (corresponding to actuators 1 and 2). The rotational inertia I of the load was approximately $2 \times 10^{-3}\,\mathrm{kgm}^2$. Joint friction was modeled as viscous damping with a damping coefficient b of approximately $1.2 \times 10^{-3}\,\mathrm{Nms}$. The inertia of the load primarily originated from two masses placed at the ends of a long rod. With the masses on separate ends of the rod (Fig. 5.3a), the center of mass of the load coincided with the axis of rotation with no resulting net torque from gravity. Shifting both masses to the same side (Figs. 5.3b,c) created a positive or negative load torque with a maximum magnitude of $\tau_{load} = 0.65\,\mathrm{Nm}$. In these configurations, the inertia of the system was approximately preserved.

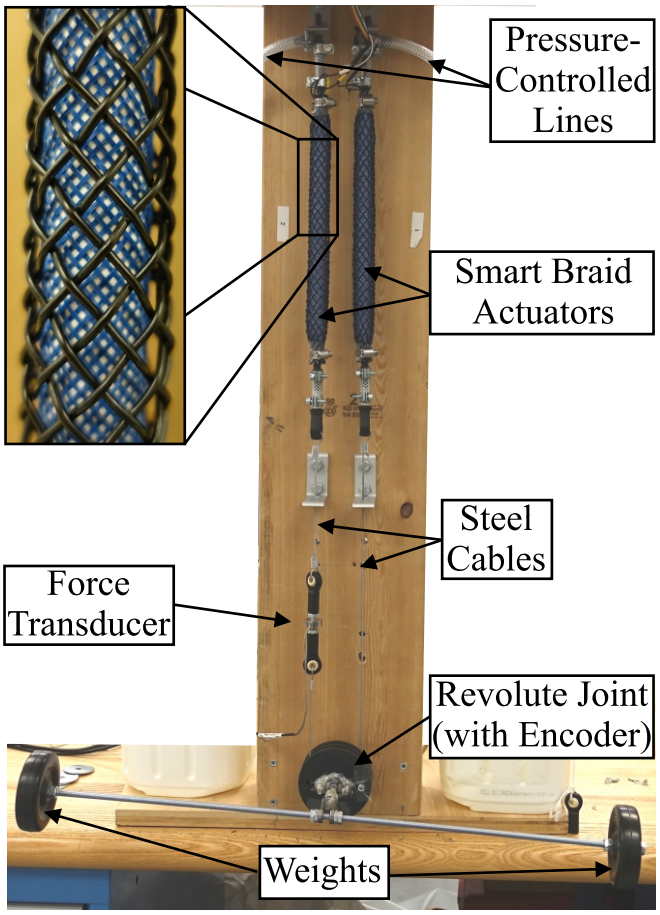

Figure 5.2: A one degree of freedom revolute joint allowed the comparison of two types of feedback control: one based on measurements from a rotary encoder and another based on measurements from Smart Braid sensors. The Smart Braid sensors used in the present work were placed on top of an inner, non-conductive reinforcing braid (enlarged detail, black wires are conductive, blue fibers are PET). A force transducer in series with the connection to the left actuator measured the tension in the connection cable.

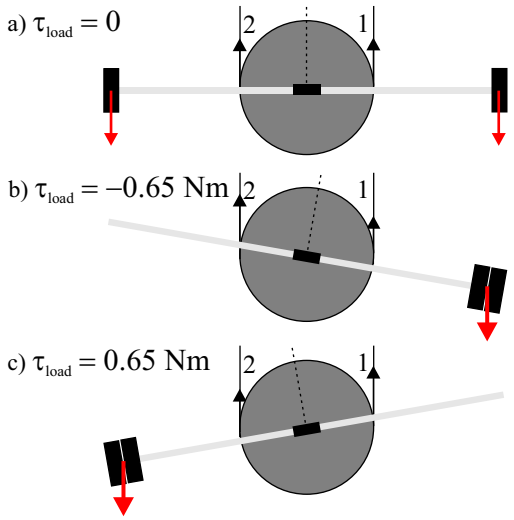

Figure 5.3: The revolute joint consisted of a pulley connected to two masses at the ends of a thin rod. The controller was tested in each of three conditions: a) with no load torque from gravity, b) with a negative load torque, and c) with a positive load torque.

5.2.1 Estimation of Revolute Joint Angle with Smart Braids

The actuator neutral lengths $l_{neutral}$ were defined as the lengths of the actuators when the joint angle was $0\,^\circ$ and the connections to the joint were without slack but unstretched. The actuator contractions x were the deviations of the actuator lengths l away from $l_{neutral}$

$$\begin{aligned} x_1 &= l_{1,neutral} - l_1 \\ x_2 &= l_2 - l_{2,neutral}. \end{aligned} \tag{5.1}$$

For each actuator, a linear function of the inductance L was used to estimate the actuator contraction $x(L)$ [3]

$$\begin{aligned} x_1(L_1) &= a_{r1}L_1 + b_{r1} \\ x_2(L_2) &= a_{r2}L_2 + b_{r2}. \end{aligned} \tag{5.2}$$

If the connections between the actuator and joint were perfectly stiff, the length of the actuators could be used to directly determine the joint angle. Chapter IV, sug-

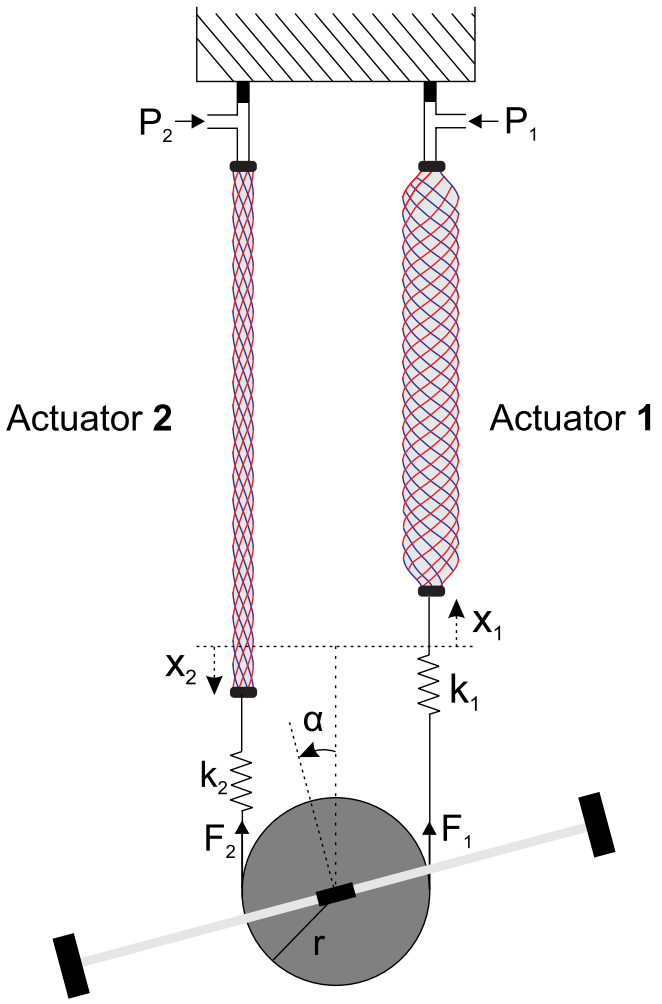

Figure 5.4: When pressurized (with pressure values P_1 and P_2), the actuators in the revolute joint test fixture exerted forces F_1 and F_2. The difference in the two forces created a net torque on the rotating load which induced contractions in the actuators x_1 and x_2 and a rotation of the load (expressed by the angle α). The actuators connections were compliant and thus modelled as springs with linear stiffness k_1 and k_2.

gests that measurements of joint-motion can be skewed by compliance in mechanical couplings between joint and actuator. This compliance was thus compensated for by modeling the force output of the actuator and the compliance of the connection points. This compliance compensation used measurements of the actuator pressure to estimate the actuator force output. With the assumption that the connections were under tension, the displacement of the actuators was written in terms of the joint angle α and the output force F. This relationship took into account the stretching of the actuator connections (with stiffness k)

$$\begin{aligned} x_1 &= r\alpha + \frac{F_1}{k_1} \\ x_2 &= r\alpha - \frac{F_2}{k_2}. \end{aligned} \tag{5.3}$$

The estimates of α that result from inverting these relationships will be most accurate when the forces F are small and the stiffnesses k of the connections are high.

5.2.2 Calibration of the Revolute Joint

To characterize the force, pressure and contraction relationship of the actuators, an empirical function was used. It was based on the contraction ratio ϵ_i [165] which is the normalized difference between the fully extended actuator length l_e and the current actuator length l_i

$$\epsilon_i = \frac{l_e - l_i}{l_e}. \tag{5.4}$$

The estimated actuator force output $\hat{F}_i$ was modeled as a polynomial that is linear with respect to actuator pressure P_i and quadratic with respect to the contraction ratio ϵ_i:

$$\hat{F}_i = p_{00} + p_{10}P_i + p_{01}\epsilon_i + p_{11}P_i\epsilon_i + p_{02}\epsilon_i^2. \tag{5.5}$$

To collect the necessary data for the calibration, the actuators were tested under a range of cable tensions and actuator pressure values. The tensions ranged between

5 N and 30 N (with 5 N increments). At each tension level, the pressure of actuator 1 was set to each of a series of pressure values between 0.1 MPa and .31 MPa for 30 seconds (in .035 MPa increments). During each 30 second period, the pressure in actuator 2 was adjusted automatically to create the desired tension. This adjustment process was driven by measurements of cable tension from the force transducer in line with actuator 2 (Fig. 5.2). In this way, data was collected at each combination of the tension levels and actuator 1 pressures. After each combination of pressure and tension was tested on actuator 1, the process was repeated with actuator 2 at the fixed pressure values. In this case, the pressure in actuator 1 was adjusted to maintain the desired cable tension. The steady-state data from the last 15 seconds of each pressure-tension combination were used in the calibration.

The data from these experiments were used to identify the coefficients of Eq. (5.2) and the estimated connection stiffness $\hat{k}$ in Eq. (5.3) (Table 5.1). The data were also used to identify the coefficients of Eq. (5.5) (Table 5.2). Note that connections to actuator 2 were less stiff than those to actuator 1. This was caused by the additional, compliant cable-ends used to include the force transducer in the cable (Fig. 5.2). The low values of the coefficient of determination R^2 in Table 5.2 result, in part, from hysteresis effects which are not modeled [165] and the noisy measurements from the force transducer.

Table 5.1: Identified Coefficients for Eq. (5.2) and (5.3)

	a_r (mm/μH)	b_r (mm)	$1/\hat{k}$ (mm/N)	R^2
Actuator 1	13.47	-89.417	0.0547	0.99942
Actuator 2	-13.881	86.979	0.110	0.99910

Table 5.2: Identified Coefficients for Eq. (5.5)

	p_{00} (N)	p_{10} (N/MPa)	p_{01} (N)	p_{11} (N/MPa)	p_{02} (N)	R^2
Actuator 1	-24.312	518.76	-33.769	-1429.5	-285.66	0.66
Actuator 2	-37.934	788.98	-200.03	-2503.7	494.79	0.87

5.2.3 Compliance Compensation and Feedback Control of the Revolute Joint

The goal of the feedback controller was to regulate the joint angle α to a desired angle α_{des}. Based on this desired angle, the relationships in Eq. (5.3) defined the desired length x_{des} of each actuator as a function of estimated actuator force outputs $\hat{F}_i$ and estimated connection stiffnesses $\hat{k}_i$:

$$\begin{aligned} x_{1,des} &= r\alpha_{des} + \frac{\hat{F}_1}{\hat{k}_1} \\ x_{2,des} &= r\alpha_{des} + \frac{\hat{F}_2}{\hat{k}_2}. \end{aligned} \tag{5.6}$$

The force estimates $\hat{F}_i$ in the compensation terms were found by evaluating Eq. (5.5) with measurements of current pressure and actuator length. Length measurements were obtained from inductance values via Eq. (5.2).

The difference between the desired and measured contraction of each individual actuator constituted the control error e_i:

$$e_i = \frac{x_{i,des} - x_i\left(L_i\right)}{r}. \tag{5.7}$$

This error was normalized by the pulley radius r to yield values in units of joint angle. The complete compensation process is illustrated in Figure 5.5.

A separate PID controller for each actuator regulated the position errors e_i by commanding desired actuator forces $F_{i,des}$ (Fig. 5.6). To maintain tension in both actuators, an equal "preload" force F_{pre} was added to each desired force value. Differ-

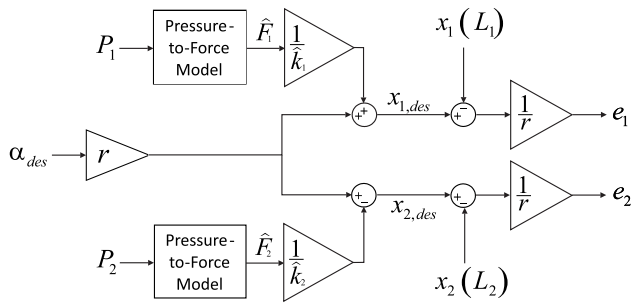

Figure 5.5: The desired actuator contractions $x_{i,des}$ included a compensation term to account for stretching in the actuator connections. This compensation term was based on estimates of the force output $\hat{F}_i$ and the stiffness of the connections $\hat{k}_i$ of each actuator. The control error between the desired and measured contraction was scaled by the radius r of the pulley to yield a joint angle error e in units of radians.

ent levels of preload were evaluated experimentally. Because the actuators are unable to create negative forces, both $F_{i,des}$ were saturated to be positive:

$$\begin{aligned} F_{1,des} &= \max\left(k_p e_1 + k_d \dot{e}_1 + k_i \int e_1 + F_{pre}, 0\right) \\ F_{2,des} &= \max\left(-k_p e_2 - k_d \dot{e}_2 - k_i \int e_2 + F_{pre}, 0\right). \end{aligned} \tag{5.8}$$

By inverting Eq. (5.5), the desired forces $F_{i,des}$ were converted into desired pressure values for each actuator $P_{i,des}$, and sent to pressure-control valves.

The performance of the Smart Braid feedback was compared to feedback from a rotary encoder on the joint. When using the encoder for feedback, the actuator-specific error value was simply the difference between the desired angle α_{des} and the measured angle $\alpha_{measured}$

$$e_1 = e_2 = \alpha_{des} - \alpha_{measured}. \tag{5.9}$$

This error was used in both PID controllers of Eq. (5.8). No compliance compensation had to be performed.

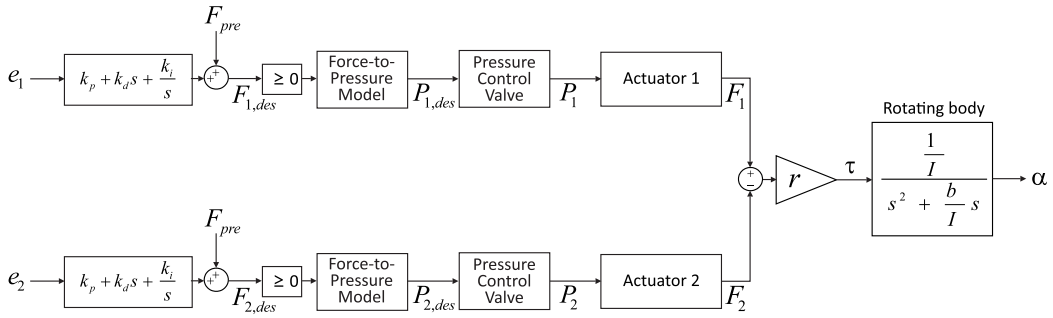

Figure 5.6: For the revolute joint, two separate PID controllers commanded a desired force $F_{i,des}$ for each actuator in reaction to estimated joint angle error terms e_i. When the Smart Braids were used for feedback, e_i were determined individually from the measured inductance and pressure. When the encoder was used for feedback, e_i were equal. To generate the desired forces, the controller computed desired pressure values from a model of the actuator force-pressure-length relationship and sent these values to two pressure control valves.

5.2.4 Experimental Implementation, Revolute Joint

A Texas Instruments "inductance-to-digital converter" (TI LDC1612/4, [166]) provided rapid measurements of the sensor inductance. This chip operates by exciting the natural frequency of a resonant tank circuit formed by an inductor and a capacitor in parallel. The Smart Braid sensors were connected in parallel with 390 pF capacitors. The series resistance of the Smart Braid sensors was approximately 0.3 ohms. The inductance values from the sensors had a target sampling rate of 1 kHz. An analysis of the inductance measurements from the Smart Braids in relaxed conditions showed an RMS noise level of 0.24 nH.

In the revolute joint test fixture, a digital incremental encoder (Koyo Electronics Industries, TRDA-2E2500VD) provided joint angle measurements with a quadrature resolution of 0.036 °. The pulley radius r where the cables were connected to the revolute joint was 25.4 mm. A force transducer (Omega LC201-100) was attached serially to the steel cable of actuator 2. This was used to characterize the force-pressure relationship of the actuators, characterize the stiffness of the actuator connections,

and measure preload tracking performance. The systems were controlled with custom scripts in LabVIEW. The measurements from the test apparatus were collected and processed with a data acquisition unit (NI PXIe-6341), which used a PXI express chassis (NI PXIe-1073) to communicate with LabVIEW. Inductance measurements were collected via an I2C bus (NI USB-8451). The mass flow rate into the actuator lines was controlled with proportional pneumatic valves (Enfield LS-V05s). The pressure in each actuator line was measured with pressure transducers (WIKA A-10) with a 0.41 MPa range and controlled with a custom controller with compensation for the non-linear aperture flow across the valves [167]. A 250 Hz LabVIEW loop acquired data from the pressure-sensors and sent commands to the valves. The system pressure was limited to 0.31 MPa. Estimates of $\dot{e}$ were filtered with a five-point moving average. In the control loop, the measurements of inductance were filtered with a 3rd-order low-pass Butterworth filter with a cutoff frequency of 10 Hz. To prevent excessive integrator wind-up, the product of the error integral and the integral gain was not permitted to exceed a magnitude of 50 N. The two types of feedback were tested in random sequence at each of seven preload levels F_{pre}: 5 N, 7.5 N, 10 N, 12.5 N, 15 N, 17.5 N and 20 N. Gains for each feedback type were selected by the "some-overshoot" Ziegler-Nichols method [168]. First a set of tuning trials were conducted in which gains were identified individually at each preload level. From the identified gains, the most conservative ones were subsequently used in the controller evaluation, where they were kept identical for all commanded preload levels (Table 5.3). This was done to ensure control stability in the event that the preload level did not match the commanded level.

Table 5.3: Gains for revolute joint feedback controller

Feedback Type	k_p (N/rad)	k_d (N/ (rad/s))	k_i (N/ (rad s))
Encoder	19.80	3.4	74.05
Smart Braids	18.15	4.16	52.27

Each controller configuration was tested on a fixed sequence of step changes for the desired joint angle α_{des}. The sequence was a random series of 21 angles between -30 ° and 30 °, that were held for ten seconds each. The data from the first five seconds of each step were considered "transient" and the data from the last five seconds were considered "steady-state." The performance was quantified by the root-mean-square (RMS) of the absolute error between the reference angle (α_{des}) and the angle measured by the encoder. During these tests, no load torque was applied (Fig. 5.3a). Each feedback type was tested at a given preload level three times. Statistical significance between the feedback types was determined by paired t-tests across each of the commanded angles in the combined three tests. The values of the measured preload were averaged over the last five seconds of each step in the sequence.

In order to evaluate the effectiveness of the compliance compensation in Eq. (5.6), the controller tests were repeated with the two load configurations that generated a non-zero net-torque (Figs. 5.3b,c). The unmodeled load torque renders open-loop control infeasible and stretches the actuator connections asymmetrically.

5.2.5 Results, Revolute Joint

Feedback control based entirely on soft, Smart Braid sensing is feasible. The Smart Braid feedback controller was able to track step changes in the commanded angle (Fig. 5.7). With no load torque, Smart Braid feedback led to an average RMS in the joint angle error of 1.73 ° (standard deviation 0.69 °) during the last five seconds of each commanded angle (considered steady-state, Fig. 5.8). The average RMS of the tracking error in the first five seconds of the commanded angles was 7.85 ° (SD 5.21 °). Even with load torques of 0.65 Nm, the average steady-state error remained less than 2 ° (SD $<$ 1 °, Fig. 5.9).

The positional accuracy of the inductance feedback controller was comparable to the performance of a controller with feedback from the rotary encoder. During the

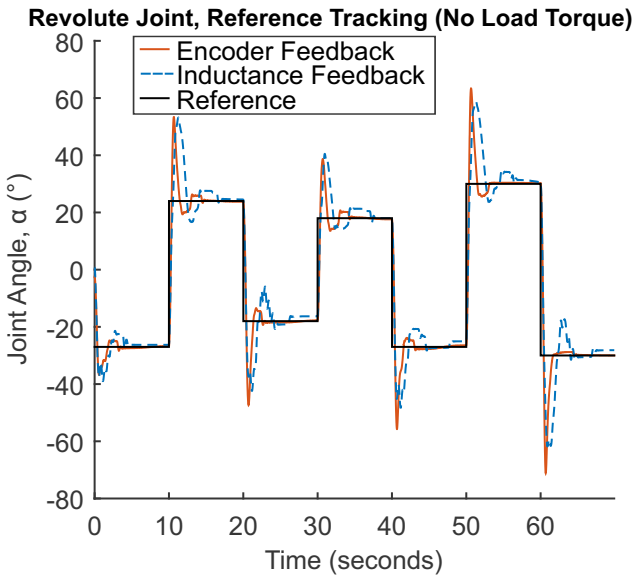

Figure 5.7: Comparison of the effect of feedback type on the reference tracking of the revolute joint controller. On average, the encoder feedback (red lines) resulted in better joint angle tracking than the Smart Braid feedback (blue lines). During the first five seconds after the commanded step change, the average RMS of the error was 16 % smaller in the encoder feedback case. In the last five seconds, the RMS of the encoder feedback error was, on average, 51 % smaller than the Smart Braid error. In the case shown here, the desired preload was 10 N and no load torque was applied. Reported values were measured with the rotary encoder.

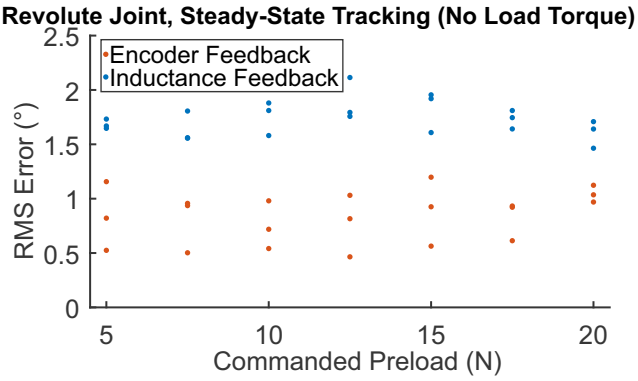

Figure 5.8: Comparison of the steady-state error of the two feedback types used on the revolute joint under different preload conditions. Shown are the average RMS values across the three trials with no load torque. The vertical axis corresponds to the RMS of the reference error during the last five seconds of a commanded angle. The feedback from the encoder resulted in smaller errors in the steady-state tracking.

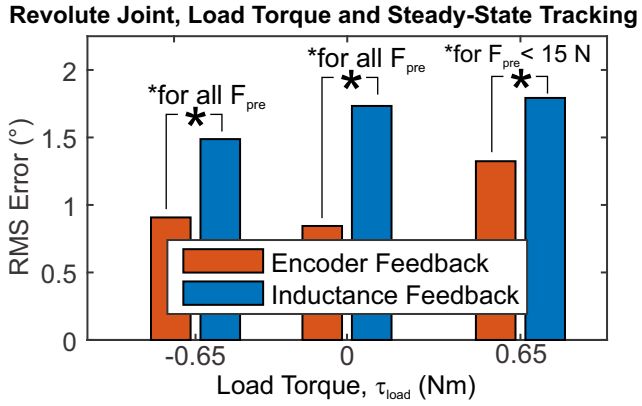

Figure 5.9: Comparison of the steady-state error of the two feedback types used on the revolute joint under different load torque conditions. The height of the bars represents the averages of the RMS error across all the commanded preload levels during the last five seconds of each of each commanded angle. The average error with encoder feedback was always less than with inductance feedback. This difference was statistically significant ($p < .05$) in all cases except when τ_{load} =0.65 Nm and the desired preload was 15 N or higher.

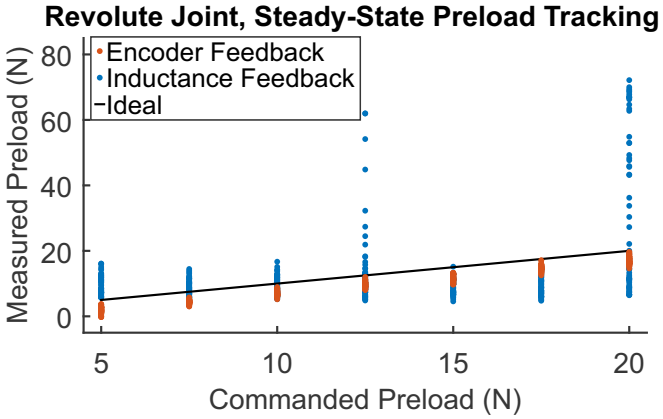

Figure 5.10: Shown are the preloads on the revolute joint averaged over during the last five seconds of each commanded angle in the controlled trials. The two types of feedback resulted in different preloads. The effectual single integrator of the encoder feedback resulted in better preload tracking than the two integrators of the inductance feedback. For the conditions shown here, no load torque was applied.

first five seconds after a step change in the reference angle the average RMS of the tracking error with encoder feedback was 6.60 ° (16 % lower than with Smart Braid feedback, SD 4.56 °, Fig. 5.7). Encoder feedback resulted in steady-state (during the last five seconds) errors with average RMS values between 0.8-1.3 ° depending on the load torque (SD $<$ 0.8 °, Fig. 5.9). This was smaller than the 1.5-1.8 ° average RMS errors exhibited with Smart Braid feedback.

Figure 5.10 shows the measured preloads averaged over the last five seconds of each reference angle in the controlled trials (no load torque). With Smart Braid feedback, preloads of nearly 70 N were observed in the 12 N and 20 N conditions. The large preloads resulted from integral windup in the physically antagonized yet independent PID controllers.

5.3 Continuum Manipulator

As a second example, the experimental work of this chapter includes the use of Smart Braid feedback in a simple, planar, one degree of freedom manipulator driven by Smart Braid McKibben muscles (Fig. 5.11). The manipulator consisted of two contracting McKibben muscles connected along their length to a bendable "spine." Differences in actuator pressure values caused different levels of contraction in the actuators, creating bending motions in the structure. By measuring the lengths of the actuators via Smart Braid inductance measurements, the degree of bending was estimated. This estimate was used as feedback to control the tip angle of the manipulator. This Smart Braid feedback control was compared to open-loop control based solely on actuator pressure.

5.3.1 Estimation of Continuum Manipulator Tip Angle with Smart Braids

The continuum manipulator was modeled as having a constant curvature enclosing an angle α. The length of the center of the manipulator was constant, constrained

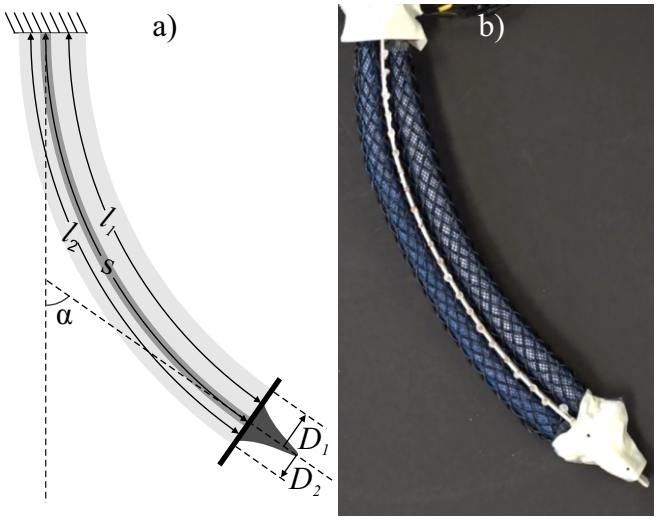

Figure 5.11: The continuum manipulator is formed from two Smart Braid actuators attached to a thin, flat, flexible beam. Contracting the actuators caused the beam to bend. a) The bend angle α was related to the lengths of the two actuators l_1 and l_2 and the fixed length s of the flexible spine. b) The prototype device bending.

by a thin beam of length s. The braids of the two actuators on the sides were tied to the thin beam. The length of the actuators along their center-lines l_i was related to the bending angle α by

$$\alpha = 2\frac{s - l_1}{D_1} = 2\frac{l_2 - s}{D_2} \tag{5.10}$$

where D_i is the diameter of the actuator cross section. It was assumed that the actuator radius was approximately the distance to the actuator center-line from the center-line of the thin beam.

The inductance L of the two Smart Braids is related to the tip angle α with an empirical equation which is linear with respect to the two inductance values [5]

$$\alpha_{est} = a_{c1}L_1 + a_{c2}L_2 + b_c. \tag{5.11}$$

5.3.2 Calibration, Continuum Manipulator

The control variable for the continuum manipulator was the pressure difference ΔP between the two actuators. From this difference, the desired pressure in each actuator was computed such that there always remained a minimal baseline pressure of P_{base}:

$$P_{1,des} = \begin{cases} P_{base} + \Delta P, & \Delta P > 0 \\ P_{base}, & \Delta P \leq 0 \end{cases}$$
$$P_{2,des} = \begin{cases} P_{base}, & \Delta P \geq 0 \\ P_{base} - \Delta P, & \Delta P < 0. \end{cases} \tag{5.12}$$

The value of baseline pressure P_{base}=0.05 MPa was selected to roughly correspond to the onset of actuator motion under no-load conditions.

To calibrate the continuum manipulator, ΔP was increased and decreased linearly between approximately -0.1 MPa and 0.1 MPa five times over the course of ten minutes. Because of the slowly-changing pressure values, the dynamics of the actuator motion were neglected. The calibration pressures were assumed to correspond to steady-state measured angles. These data were processed to identify a relationship between ΔP and α. The data were regressed to a linear approximation of the form

$$\alpha = a_{cp}\Delta P + b_{cp}. \tag{5.13}$$

The identified coefficients of Eq. (5.13) are listed in Table 5.4. The nonzero value of b_{cp} is indicative of the asymmetry in the system. The angle to pressure relationship

Table 5.4: Identified Coefficients for Eq. (5.13)

a_{cp} (deg/MPa)	b_{cp} (deg)	R^2
597	3.45	0.826

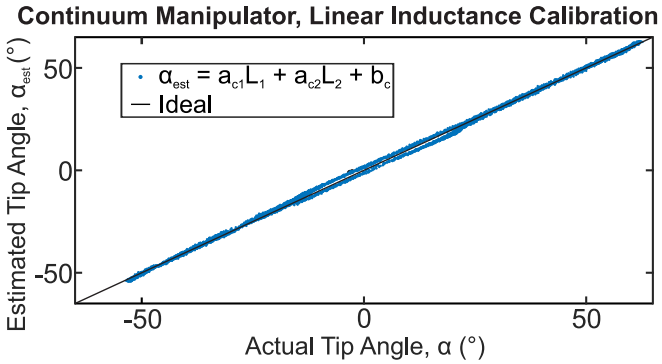

Figure 5.12: Shown are the estimated values of the tip angle ($\alpha_{est} = a_{c1}L_1 + a_{c2}L_2 + b_c = 31.93L_1 - 45.11L_2 + 77.08$) from the inductance values used in the calibration. These values are compared against the tip angle recorded by the camera.

exhibited hysteresis and non-linearity (Fig. 5.15). Different pressure values often resulted in the same tip-angle. This is apparent in the large degree of variation in the angle that is not captured by the linear model ($R^2 = 0.826$).

The calibration data were also used to identify a relationship between the continuum angle and the measured inductance of the Smart Braid actuators. A two-variable linear regression was used to identify the coefficients of Eq. (5.11). They are listed in Table 5.5. The RMS of the residual error was 1.17° (Fig. 5.12).

Table 5.5: Identified Coefficients for Eq. (5.11)

a_{c1} (deg/μH)	a_{c2} (deg/μH)	b_c (deg)	R^2
31.93	-45.11	77.08	0.999

5.3.3 Feedback Control of Continuum Manipulator

The Smart Braid feedback controller used inductance values and Eq. (5.11) to estimate the manipulator tip angle α_{est} (Fig. 5.13a). This estimate was compared against the reference angle α_{des} to calculate the feedback error e

$$e = \alpha_{des} - \alpha_{est}. \tag{5.14}$$

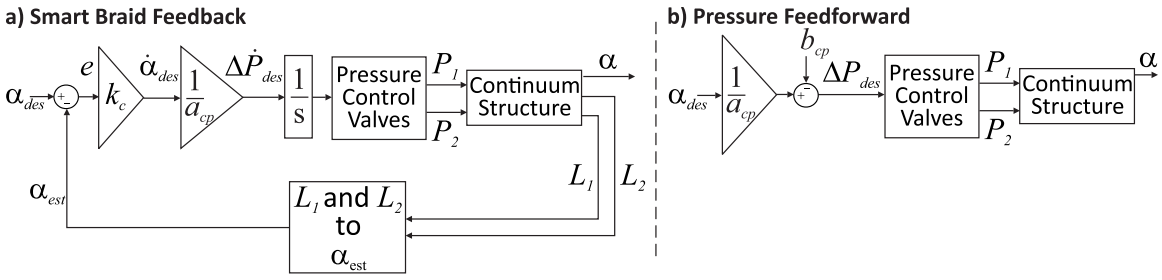

Figure 5.13: The performance of two controllers were compared on the continuum manipulator: a) the Smart Braid feedback controller which used tip angle estimates from the inductance-based, Smart Braid sensors and b) a feedforward controller for the actuator pressures.

This error e was scaled by the gain k_c to calculate a desired angular rate $\dot{\alpha}_{des}$

$$\dot{\alpha}_{des} = k_c e. \tag{5.15}$$

The desired angular rate was again scaled by the inverse of a_{cp} to calculate a desired rate of pressure difference change $\Delta\dot{P}_{des}$ according to the time derivative of Eq. (5.13)

$$\Delta\dot{P}_{des} = \frac{\dot{\alpha}_{des}}{a_{cp}}. \tag{5.16}$$

The desired rate of pressure difference change $\Delta\dot{P}_{des}$ was then integrated numerically in the controller to calculate the desired pressure difference ΔP_{des}. The corresponding actuator pressure values were calculated with Eq. (5.12) and sent to pressure-controlled valves.

For comparison, an open-loop, feedforward controller was implemented that used the inverse of Eq. (5.13) to generate pressure commands for the actuators (Fig. 5.13b).

5.3.4 Experimental Implementation, Continuum Manipulator

The continuum manipulator used the same data acquisition and pneumatic control hardware as the revolute joint. The manipulator was fabricated by fastening the outer, conductive braids of the actuators to a flexible spine. The spine consisted of two (0.83 mm thick) strips of Delrin plastic. To establish a ground truth, the angle α of the actuator tip was additionally measured by visually tracking the motion of two points at the actuator tip. The angle of these points was computed relative to two-fixed points on the ground plane. The point positions were recorded with a high-frame-rate camera (120 fps) placed above the manipulator (with the camera's visual field parallel to the plane of actuation). The system pressure was limited to approximately 0.20 MPa. As with the revolute joint, the Smart Braids were connected in parallel to 390 pF capacitors. For this system, the target inductance sampling rate was 250 Hz.

The value of the gain k_c used in the inductance feedback loop was $5\,\mathrm{s}^{-1}$. The performance of controllers was evaluated with the same pseudo-random step input used with the revolute joint. Each controller was evaluated three times. The steady-state tracking was evaluated over the latter half of each step. That is, the last five seconds of a step lasting ten seconds.

5.3.5 Results, Continuum Manipulator

The inductance feedback controller was able to track the reference signal with a smaller steady-state error than the pressure feedforward controller. Visually-tracked tip-angle trajectories from typical controller trials are shown in Fig. 5.14. The steady-state RMS error of the inductance feedback controller had an average value of 1.25° and a standard deviation of 0.63°. On the other hand, the pressure feedforward controller had larger and less consistent steady-state errors (mean of 14.98°, SD of 9.58°). Figure 5.15 shows the pressure differences and tip angles recorded during the

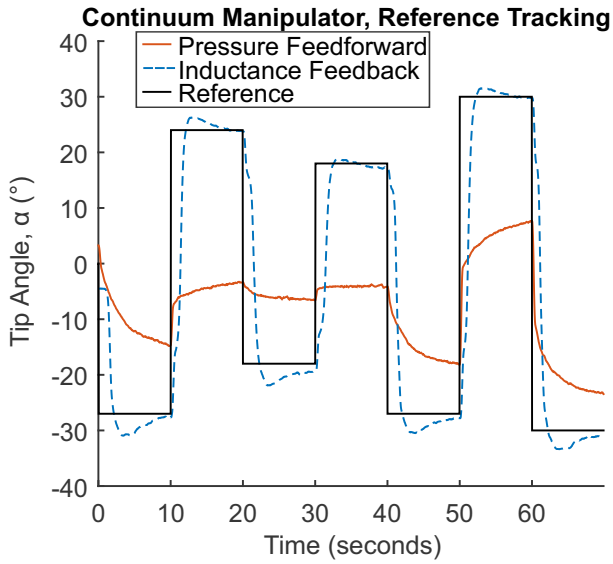

Figure 5.14: Shown are the tip angles of the continuum manipulator as recorded by the camera during two trials. The inductance feedback controller allowed the continuum manipulator to track the reference input with an RMS of 1.25° in the steady-state error (evaluated in the last five seconds of the step). The supplementary video includes a recording of the inductance feedback trial.

controller trials alongside the calibration data.

5.4 Discussion and Conclusions

This chapter shows how Smart Braid sensors can be used as feedback for the motion control of soft robotic systems. Smart Braids can provide rapid and precise measurements of actuator length. Motion control was demonstrated in both a revolute system and a bending continuum manipulator. For the revolute joint, techniques were developed to compensate for compliance between actuators and points of motion output. These techniques extend to other actuator length-sensing technologies.

The revolute joint was designed to rigorously compare the Smart Braid feedback to feedback from a rotary encoder. The high-inertia, lightly-damped ($I \approx 2\times10^{-3}\,\mathrm{kgm}^2$, $b \approx 1.2\times10^{-3}\,\mathrm{Nms}$) rotating load pushed the limits of the controller by creating highly dynamic loads. The results show that, even in this setting, inductance measurements

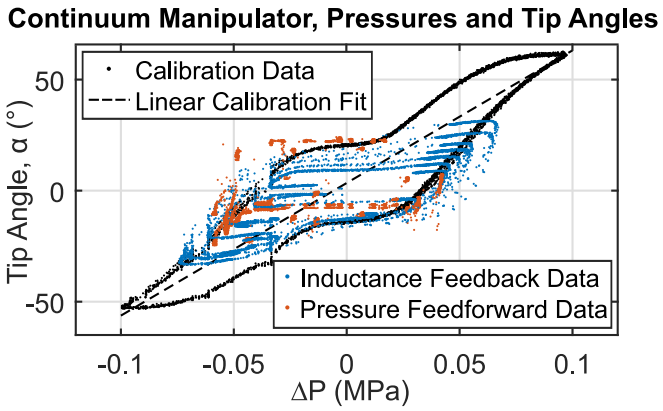

Figure 5.15: Shown are tip angles and pressure values observed during the calibration and controlled trials. They exhibited hysteresis and non-linearity. The black dots are the calibration data. The hysteresis is the main obstacle when inverting the calibration curve for open-loop feedforward control. In this chapter, the inversion was performed on a linear fit to the entire data set (dashed black line shown above). The colored dots are the data from the angle-control trials. In the controlled trials, the ambiguous relationship between the differential pressure and the tip angle is apparent.

from Smart Braid sensors can be used in real-time feedback control.

When load torques were applied to the revolute joint, the compliance compensation allowed the Smart Braid feedback controller to remain accurate. The addition of an external torque had only a small effect on the performance of the inductance-feedback controller. Without the compliance compensation (and given the connection stiffnesses characterized in Table 5.1), a negative load torque would have led to approximately 3° of steady-state error. The less-stiff tendon of actuator 2 would have resulted in a 6° error with the positive load torque. With the compliance compensation, the average RMS of the steady-state error in each case was less than 2°.

Controlling the actuators *individually* with the proposed compliance compensation technique sometimes created large tensions in the system. The large preloads could be precluded by controlling the two actuators together with a single controller (as was effectually the case with the encoder feedback).

Smart Braid feedback was also demonstrated on the angle-control of a bending

continuum manipulator. The feedback used in this chapter permitted the manipulator to reach desired joint angles using only the inductance measurements from the Smart Braids. The closed-loop control of the manipulator resulted in more accurate reference angle tracking than the simple, open-loop control of pressure. The comparatively poor performance of the open-loop control was due, in part, to hysteresis and unavoidable friction in the system (Fig. 5.15).

The bend sensing of the continuum manipulator relied on only two sensors. It was limited to approximating the shape of the manipulator as a single segment with constant curvature. This approximation is not necessarily accurate in the presence of external forces and constraints. The constant curvature assumption is most accurate when applied to short segments of the curve [169]. Using Smart Braid sensors on multiple, shorter segments of the actuators could allow more accurate estimation of the end-tip position and orientation. Similarly, the principles in this chapter could be extended to 3D manipulators.

The Smart Braid actuators in the present work are slightly different than those used in the previous chapter. In Chapter IV, the wires of the Smart Braid sensor served the role of both sensor and reinforcing fiber. In the pilot work for this study, it was found that the wires bearing the stress of the internal pressure would often yield under high and repeated strain. For this reason, it was decided to use Smart Braid sensors on top of a plastic braid that would bear the stress. After 40 hours of testing, the sensors showed no signs of wear. The addition of the Smart Braid sensor on top of the inner braid results in disparate length/diameter relationships in the wire braid and the plastic braid. In the revolute joint, this caused the Smart Braid sensor to have a larger diameter than the inner braid in contracted conditions (Fig. 5.2). In some applications, this would allow relative motion between the two braids, possibly biasing the estimates of the actuator length. A more sophisticated fabrication method could use a single layer of high-strength fibers with long-flex-life

conductors.

Though the fabrication method of the *actuators* was different, the *sensors* were fabricated in the same manner as Chapter IV. As such, they exhibited a similar sensitivity to the actuator contraction compared to sensors in the previous chapter. The actuator in Chapter IV showed a contraction sensitivities of $6.8\times10^{-8}\,{}^{\mathrm{H}}/_{\mathrm{mm}}$. In the present work, the sensitivities of actuators 1 and 2 were $7.4\times10^{-8}\,{}^{\mathrm{H}}/_{\mathrm{mm}}$ and $7.2\times10^{-8}\,{}^{\mathrm{H}}/_{\mathrm{mm}}$ respectively.

The results demonstrate that Smart Braids can control the motion of soft robotic systems. The Smart Braid sensors in this chapter enabled the closed-loop angle-control of a revolute joint and a continuum manipulator using local, flexible sensors. The contracting actuators used in this work are very similar to actuators used in industry [155] and extensively in robotics research [135]. The experimental results and methods of this chapter open a new avenue of design for soft robotic systems that rely on these actuators. Furthermore, they bring sensing to systems that would, perhaps, have been limited to open-loop control.

CHAPTER VI

Inductance-based Sensing for Bellows-driven Robots

Adapted from Wyatt Felt, Maria Telleria, Thomas F. Allen, Gabriel Hein, Jonathan B. Pompa, Kevin Albert, and C David Remy. "An Inductance-Based Sensing System for Bellows-Driven Continuum Joints in Soft Robots". *Under Review.*

6.1 Introduction

The dissertation up this point has focused on fiber-reinforced actuators. These actuators see a great deal of use in research and industry. Another common actuator in soft robotics is the bellows. The purpose of this chapter is to apply the inductance-based sensing strategy developed in the previous chapters to bellows. This chapter studies the viability of inductance-based sensors for circular bellows actuators from both a theoretical and experimental perspective.

This chapter focuses on sensing and controlling the motion of a particular type of soft robotic joint: the bellows-driven continuum joint. The sensing system relies on coils of insulated conductive wire wrapped around the minor diameters of the bellows. These coils form circuits with inductance values that change with the length of the bellows. The measured inductance values can be calibrated to measure the motion of

Figure 6.1: Bellows-driven continuum joints are used to create robots without finite degrees of freedom. Sensing the motion of such robots is a challenge. The inductance-based sensors presented in this work will bring estimation and control to robots like the one pictured here (created by Pneubotics).

the joint. This chapter demonstrates experimentally how sensors such as these can measure and control the motion of bellows-driven continuum joints.

The experimentation in this chapter utilizes a joint made from four pneumatically driven bellows that are positioned around a central steel cable (Fig. 6.1). This joint has been developed by Pneubotics. The bellows create bending torques about two axes while keeping the joint stiff in torsion. By pressurizing pairs of antagonized bellows simultaneously, the passive bending stiffness of the joint is also controllable. Joints with similar features have been developed for applications in industry and academia. These have relied on bellows [67], [170]–[172] and other soft, fluid-powered actuators [66], [173], [174].

The primary contribution of this chapter is the introduction of inductance sensors that measure the motion of bellows-driven continuum joints. This chapter develops the theory, models and design principles for these sensors. The experimental sensing system measures the motion of the joint independently in two halves along the joint length. This allows one to measure lateral displacement even when there is no change in orientation between the ends. The performance of the sensing system is tested in both quasi-static conditions and as feedback for the control of a bellows-driven joint.

The hardware of the experimental system is described in Section 6.2. Section

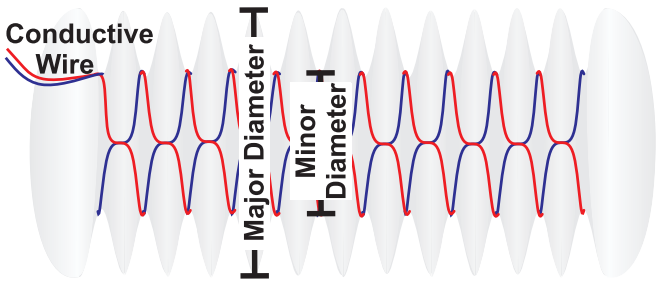

Figure 6.2: The minor diameters of the plastic bellows were wrapped with insulated conductive wire (red and blue). The inductance of the circuit provides a measure of the bellows length.

6.3 discusses theory, including the kinematics of the joint (6.3.1), models for the inductance sensor (6.3.2) and design principles relating to the same (6.3.3). Section 6.3.4 investigates the use of "split-joint" sensing to measure lateral displacement. The experimental methods and results are described in Section 6.4. This includes the calibration and verification of the sensing system (6.4.1), the estimation of the joint position under lateral loads (6.4.2) and the feedback control of the joint orientation (6.4.3). This is followed by a general discussion in Section 6.5.

6.2 Hardware

The inductance-based sensing system was implemented on a commercial, bellows-driven continuum joint. To create a self-sensing joint based on inductance, the minor diameters of the bellows were wrapped with flexible wire (Fig. 6.2). This created circuits of circular coils spaced along the length of the bellows. As a bellows expanded in length, the circular coils moved farther apart, reducing the inductance of the corresponding circuit. The joint was instrumented and controlled to calibrate and test the inductance-based sensing system.

The joint was provided by Pneubotics (an Otherlab company, San Fransico, CA, USA, Fig. 6.1). The joint consists of two plates connected to four bellows spaced around a central steel cable. The centers of the bellows are kept at a fixed distance,

designated b, of 4.9 cm from the central cable. The steel cable has a length h of 19.7 cm between the plates of the joint. It provides a "fulcrum" to convert the extension forces of the bellows into bending moments. The bellows have 26 major diameters between the plates of the joint. The major and minor diameters of the bellows are 6.7 cm and 4.9 cm, respectively. The joint is actuated by pressurizing the bellows with compressed air. The antagonized configuration of the four bellows creates a 2-DOF bending joint with independently controllable joint torque and passive stiffness. The unmodified joint has a range of motion of $\pm 90\,^\circ$ in each axis. In this work, the pressure in the bellows was maintained below 0.41 MPa.

The joint was outfitted with four distinct inductance circuits (Fig. 6.3). Pairs of adjacent circuits measured the bending in each half of the joint. The circuits were formed from "tinsel" wire with a high flex-fatigue life (TN3637, 1.14 mm outer diameter, resistance 538 $^{\text{ohms}}/_{\text{km}}$, MN wire, St. Paul, MN, USA). The flexible wire was wrapped around 12 minor diameters of the bellows in the corresponding half. Each minor diameter had two turns of current (except at the ends of the circuits where there was only one turn). The inductance was measured with an LDC1614 chip (Texas Instruments, Dallas, TX, USA). This chip measures the resonant frequency of four inductor-capacitor oscillating circuits in rapid succession. To this end, each inductive circuit was connected in parallel with a high-precision (1 %, NP0) 100 pF ceramic capacitor.

To provide a ground truth reference for the proposed sensor, the joint was mounted upside-down on a level mount such that the relative orientation of the ends could be measured with an IMU (3-Space Micro USB, magnetometer disabled, Yost Labs, Portsmouth, OH, USA). A 38 cm arm was attached to the end of the joint for calibration and testing. Weights were added to the end of the arm to create different loading conditions. The pressure in the bellows was controlled with electronic pressure regulators (TR, Enfield Technologies, Shelton, CT, USA). The data acquisition

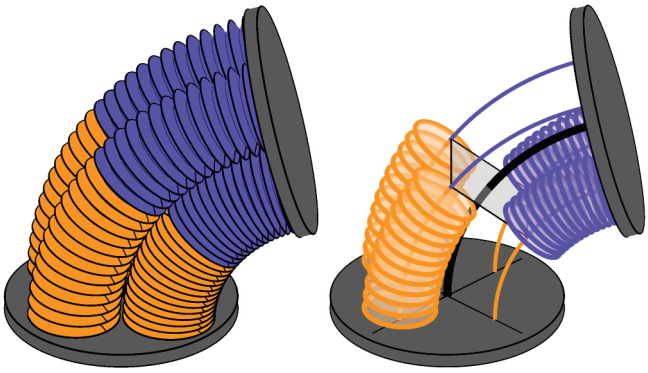

Figure 6.3: The deformation of the entire joint was approximated as the composition of two constant-curvature sections. Pairs of adjacent inductive sensor circuits (orange and blue circles) measured the bending of the each half independently. This "split-joint" configuration allows one to estimate the joint motion in non-uniform-curvature conditions.

and control was facilitated by LabVIEW.

6.3 Theory

6.3.1 Kinematic Model

The joint was modeled as the composition of two constant curvature sections (Fig. 6.3). This was designed to allow the deformation to be approximated even when the curvature across the length of the joint is not uniform.

For each constant-curvature section of the joint, the coordinate axes in the base frame originate at the center of the central cable and intersect with the bellows' centers (Fig. 6.4). The x-axis points towards bellows 1, the y-axis towards bellows 2, and the z-axis along the central cable (when straight). The bellows' centers are separated from the central cable by the constant distance b.

Here, the kinematics of each constant curvature section are described using a parametrization presented by Allen, et al. [175]. This parametrization has several desirable properties. It remains invertible in the straight configuration and has affine relationships between the rotation parameters and the lengths of the bellows. This

parametrization is based on the two components, u and v, of a rotation vector $\boldsymbol{\omega} = [u, v, 0]^T$. The z-component is always zero. This rotation vector $\boldsymbol{\omega}$ describes the orientation of the top of the plate relative to the base and is equivalent to rotating the top plate by an angle $\theta = \sqrt{u^2 + v^2}$ around the unit vector $\boldsymbol{\omega}/\|\boldsymbol{\omega}\|$. The rotation vector $\boldsymbol{\omega}$ can also be described by the angles ϕ and θ

$$\boldsymbol{\omega} = [u,\ v,\ 0]^T = [-\theta \sin\phi,\ \theta \cos\phi,\ 0]^T . \tag{6.1}$$

The homogeneous transformation from the base frame to a frame with distance h along the cable (assuming constant curvature across that distance) is given by the matrix $\mathbf{g}(u, v, h)$

$$\mathbf{g}(u, v, h) = \begin{bmatrix} \gamma v^2 + 1 & -\gamma uv & \zeta v & -\gamma hv \\ -\gamma uv & \gamma u^2 + 1 & -\zeta u & \gamma hu \\ -\zeta v & \zeta u & \cos(\theta) & \zeta h \\ 0 & 0 & 0 & 1 \end{bmatrix} . \tag{6.2}$$

The functions $\zeta(\theta) = \sin(\theta)/\theta$ and $\gamma(\theta) = (\cos(\theta) - 1)/\theta^2$ are defined when θ is zero. This is apparent from the Maclaurin series of sine and cosine.

The lengths $l = f(u, v)$ of the half-bellows sections along their center-lines are expressed as follows:

$$[l_1,\ l_2,\ l_3,\ l_4]^T = \frac{h}{2} + b\,[-v,\ u,\ v,\ -u]^T . \tag{6.3}$$

Because h is fixed, the length l of each bellows section is a function of either only v or only u.

The bending in the distal half of the joint was defined by $\boldsymbol{\omega}_a = [u_a, v_a, 0]^T$ and measured by the inductance values on the distal halves of bellows 1 and 2 (Fig. 6.3, blue). The proximal joint half was defined by $\boldsymbol{\omega}_b = [u_b, v_b, 0]^T$ and measured with

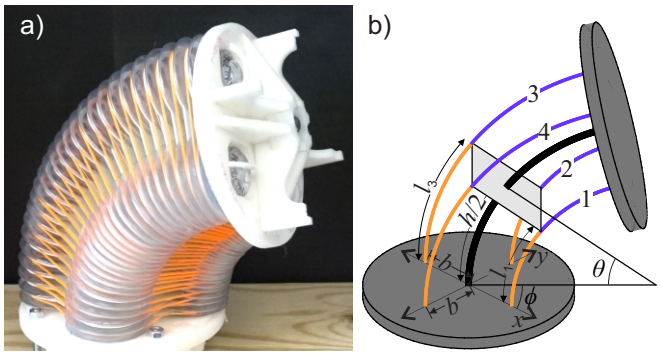

Figure 6.4: (a) Photo of a 2-DOF bellows-driven continuum joint. The orange fibers constrain the bellows around the central cable. (b) The kinematic model of the joint. Each half of the joint undergoes a bend angle θ with an orientation ϕ. The center of the joint is reinforced by a cable of length h (thick black line). The bellows are indexed from one to four. The centerlines of the half bellows (thin blue and orange lines) have lengths of l_1, l_2, l_3 and l_4. The centers of the bellows are spaced from the central cable by a distance b.

inductance sensors on bellows 3 and 4 (Fig. 6.3, orange).

6.3.2 Inductance Model

The inductive circuits are modeled as n circular coils of current connected electrically in series. Each circular coil is made up of N turns of wire. The total inductance L of the circuit is the sum of the self-inductance $L'_{i,i}$ and mutual inductance $M_{i,j}$ of the coils in the circuit. The total inductance $L = \sum_{i=1}^{n} \sum_{j=1}^{n} \mathbf{L}\,[i,j]$ is the sum of the elements in the inductance matrix $\mathbf{L}$

$$\mathbf{L} = \begin{bmatrix} L'_{1,1} & M_{1,2} & M_{1,3} & \dots & M_{1,n} \\ M_{2,1} & L'_{2,2} & M_{2,3} & \dots & M_{2,n} \\ M_{3,1} & M_{3,2} & L'_{3,3} & \dots & M_{3,n} \\ \vdots & \vdots & \vdots & \ddots & \vdots \\ M_{n,1} & M_{n,2} & M_{n,3} & \dots & L'_{n,n} \end{bmatrix}. \tag{6.4}$$

The self-inductance of the individual coils $L'_{i,i}$ does not change during actuation.

A circular wire coil with N turns of current, a coil radius r and a wire radius a has a self-inductance that is approximated by

$$L'_{i,i} \approx \mu N^2 r \left(\ln \left(\frac{8r}{a} \right) - 2 \right). \tag{6.5}$$

This approximation assumes that the current distribution is concentrated on the surface of the conductors. μ is the magnetic permeability of the surrounding medium (approximately $4\pi \times 10^{-7}$ H/m for nonmagnetic materials such as plastic and air).

The sensitivity of the inductance to joint motion comes from the change in mutual inductance between coils on different minor diameters. For these current paths, the mutual inductance is calculated numerically by integrating the Neumann formula [176]. For two paths in 3D space

$$\begin{aligned} \boldsymbol{C_1}(s_1) &= \left[x_1(s_1), y_1(s_1), z_1(s_1) \right]^T \\ \boldsymbol{C_2}(s_2) &= \left[x_2(s_2), y_2(s_2), z_2(s_2) \right]^T \end{aligned} \tag{6.6}$$

parameterized by $s_1 = [0, 1]$, $s_2 = [0, 1]$, the mutual inductance is given the double integral

$$M_{1,2} = \frac{\mu}{4\pi} \int_0^1 \int_0^1 \frac{\left(\frac{d\boldsymbol{C_1}}{ds_1}|_{s_1} \right) \left(\frac{d\boldsymbol{C_2}}{ds_2}|_{s_2} \right)^T}{\sqrt{(\boldsymbol{C_1} - \boldsymbol{C_2})(\boldsymbol{C_1} - \boldsymbol{C_2})^T}} ds_1 ds_2. \tag{6.7}$$

The mutual inductance between two N-turn coils on separate convolutions was approximated as N^2 times the mutual inductance between single-turn coils. This approximation is accurate when the distance between the turns in each coil is small relative to the distance between the two coils.

The inductance values of the circuits on the bellows change with the deformation of their corresponding joint section (e.g. $L_{1a} = f(u_a, v_a)$). In order to measure the motion of the joint, one must to invert this relationship (e.g. $u_a = f(L_{1a}, L_{2a}, L_{3a}, L_{4a})$). Here the kinematic and inductance models are used to investigate which combina-

tions of inductance sensors are suitable for use in this inversion. To this end, Eq. (6.7) was used to calculate the inductance of the circuits at different joint orientations. A circular loop of current was first defined as a geometric path. This path was then transformed by Eq. (6.2) to the appropriate positions around the joint as it underwent constant-curvature bending. For each pair of circular loops in a circuit, Eq. (6.7) was integrated with the MATLAB *integral2* function. To examine the effect of sensor placement, the sensors were modeled to be on the same section of the joint (i.e. with geometries dependent on u_a and v_a). In this configuration, the length change of the sensor modeled on bellows 1 was equal and opposite of that on bellows 3. The same relationship holds for bellows 2 and 4.

The geometry and corresponding inductance values were calculated at each combination of a series of 22 values of ϕ and 12 values of θ. The values of ϕ were equally spaced between $0\,^\circ$ and $343.64\,^\circ$ and the values of θ where equally spaced between $0\,^\circ$ and $90\,^\circ$. The inductance values were calculated only once when $\theta = 0$ (where ϕ does not change the geometry).

The modeled inductance values were used to evaluate four different sensor combinations. The first was a single-variable fourth-order polynomial regression of the length-changing rotation component against the modeled inductance of the sensor on bellows 1 ($v_a = f(L_{1a})$). The second regression was against the difference of the modeled inductance of the sensors on the antagonized pair, bellows 1 and 3 ($v_a = f(L_{1a} - L_{3a})$). The third combination was a two-variable polynomial regression against the adjacent sensors on bellows 1 and 2 ($v_a = f(L_{1a}, L_{2a})$). The final combination was a two-variable regression on the differences of each antagonized pair ($v_a = f(L_{1a} - L_{3a}, L_{2a} - L_{4a})$). The residual error of these regression types is listed in Table 6.1.

The single-variable regression ($v_a = f(L_{1a})$) explained $99.97\,\%$ of the variation in the corresponding rotation component (Fig. 6.5). The bulk of the remaining error

Table 6.1: Model Estimates of v_a with Combinations of Sensors

Polynomial Type (4th Order)	RMSE (°)	R^2
$v_a = f(L_{1a})$	0.323	0.9997286
$v_a = f(L_{1a} - L_{3a})$	0.149	0.9999421
$v_a = f(L_{1a}, L_{2a})$	0.029	0.9999979
$v_a = f(L_{1a} - L_{3a}, L_{2a} - L_{4a})$	0.020	0.9999990

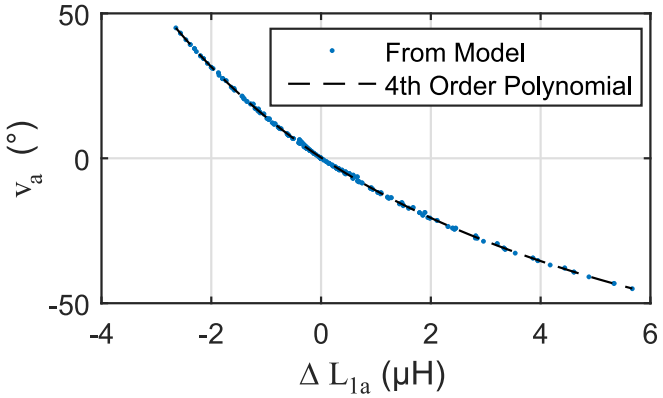

Figure 6.5: The results of the inductance model for the joint. Much of the variation in the rotational components (e.g. v_a) is explained by a simple polynomial regression against the inductance of a coil on the length-changing bellows (e.g. L_{1a}).

comes from the variance introduced by the orthogonal rotation component (e.g. u_a). The second combination looked at the difference between the inductance values L_{1a} and L_{3a}. If u_a were to effect L_{1a} and L_{3a} identically, the effect of u_a would be canceled in the difference. Though the effect of u_a on the two sensors is not identical, the regression against $L_{1a} - L_{3a}$ did lower the RMSE by 54 % ($v_a = f(L_{1a} - L_{3a})$). Including measurements from a sensor that primarily measures u_a ($v_a = f(L_{1a}, L_{2a})$) reduced the RMSE by an order of magnitude (compared to the single variable regression). A regression against the differences of both antagonized pairs only reduced the RMSE by an additional 30 %. The strategy of using two adjacent sensors on the same joint section (e.g. $v_a = f(L_{1a}, L_{2a})$) is adopted experimentally in this work.

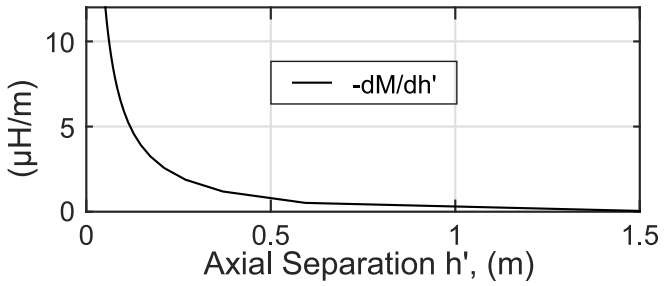

Figure 6.6: Shown is the mutual inductance sensitivity to separation of two coaxial circles of equal diameter (1 m) separated by a distance h'. The change in mutual inductance per distance traveled declines rapidly as the coils move farther apart.

6.3.3 Design Principles for Inductance Sensors on Bellows

Bellows-based inductance sensors exhibit the greatest sensitivity to motion when the minor diameters of the bellows are close together relative to the size of the diameters. Consider two coaxial circular wire coils of a single turn separated by a distance h' along their mutual axis. If the coils are moved closer together, the mutual inductance between them increases.

The change in mutual inductance per distance traveled is also affected by the distance between the coils. The sensitivity of the mutual inductance to a change in distance is $\frac{dM}{dh'}$. Its magnitude is greatest when the coils are close together and declines rapidly as they move farther apart. For example, from an axial distance of $h' = .05$ diameters to $h' = 1$ diameter, the sensitivity decreases by approximately two orders of magnitude (Fig. 6.6).

Thus inductance sensors are best-suited to work on bellows with minor diameters that are spaced much more closely than the size of the diameters themselves. The bellows used in this work, for example, have h' values of approximately 0.014 diameters when the joint is straight.

Another consideration is how many turns of wire to use in each coil. This consideration has trade-offs in sensor quality and actuation range. One measure of the

quality of an inductance sensor is the "Quality Factor" Q

$$Q = 2\pi f_{\text{excite}} \frac{L}{R} \tag{6.8}$$

where R is the resistance, L the inductance, and f_{excite} the excitation frequency. The maximum excitation frequency is often limited by the sensing circuitry or parasitic capacitance [153]. Thus, for a given frequency, it is desirable to maximize the ratio of inductance to resistance. The inductance scales with the radius r of the coils and with the square of the number of turns N^2 in each coil

$$L \propto rN^2. \tag{6.9}$$

The resistance is proportional to the number of turns N and the radius r of the circular coils and inversely proportional to the cross-sectional area of the conductor A_{wire}

$$R \propto \frac{Nr}{A_{\text{wire}}}. \tag{6.10}$$

Accordingly, the inductance to resistance ratio scales linearly with the number of turns N and the cross-sectional area of the conductors A_{wire}

$$\frac{L}{R} \propto NA_{\text{wire}}. \tag{6.11}$$

Thus, increasing the number of turns in each coil or increasing the cross-sectional area of the conductors increases the sensor quality. However, there are trade-offs to increasing these quantities. Increasing the number of turns can increase the parasitic capacitance which, if it becomes too high, can lower the feasible excitation frequency [153]. Furthermore, the wires take up physical space on the minor diameters. The

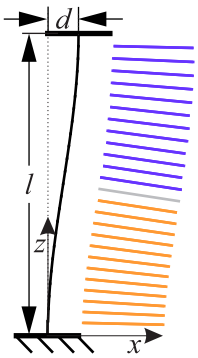

Figure 6.7: The geometry of the joint was simulated with a level displacement d. The models predict that using two circuits along the length of the joint improves the estimation of deformations like these.

cross-sectional area A_{coil} of the circular coils scales in the same way as $\frac{L}{R}$

$$A_{\text{coil}} \propto N A_{\text{wire}}. \tag{6.12}$$

This bulk of material in the convolutions could limit contraction of the bellows. In this work, the number of turns of wire in each of the circular coils was kept at a minimum.

6.3.4 Measuring Non-uniform Curvature

When actuated against external loads, the joint may be subject to non-uniform internal bending moments. These may lead to non-uniform curvature along the length of the joint. Measuring the curvature of the joint in multiple sections can improve the ability of the joint to sense certain non-uniform-curvature deformations. To demonstrate how multiple sensing sections can improve the estimation of the joint motion, the lateral displacement of the joint end was simulated with no change in orientation of the plates (Fig. 6.7). The chosen displacement was selected to highlight the opportunity of using multiple sensors along the joint length.

For this simulation, the profile of the central cable was approximated with the

simple planar equations of a thin cantilever. The cantilever considered here has a fixed end and is free but guided at the other end. A force and moment at the free end deflect it a distance d without rotation at the tip. The profile of the cantilever with this deflection is given by the following expression [177]

$$x\left(z\right)=\frac{dz^{2}}{l^{3}}\left(3l-2z\right) \tag{6.13}$$

where z is measured from the support along the length of the unloaded beam. l is the distance in z between the free and fixed ends. l is selected to conserve the length of the central cable.

The geometry of the central cable and coils was calculated for a a lateral displacement of $d = 2\,\mathrm{cm}$ in the xz-plane along the x-axis towards bellows 1. The profile of the central cable was defined by Eq. (6.13). The geometric paths describing the circular loops of current were transformed via Eq. (6.13) to their positions in the displaced configuration (Fig. 6.7). The mutual inductance between the loops on bellows 1 was then calculated with Eq. (6.7) and the MATLAB *integral2* function. Three different circuit configurations were modeled: one circuit spanning the entire bellows length (25 coils), two circuits (12 coils each) on each half of the bellows, and three circuits (8-9-8) each spanning approximately one third of the joint. The bending in each section was estimated by using the inductance values predicted for the lateral displacement in equations calibrated to constant-curvature bending. A single-variable, 4th-order polynomial (e.g. $v_a = f\left(L_{1a}\right)$) was used for each circuit. The deformation of the total joint was then estimated by composing the curvatures predicted by the calibration equations in each section.

For this type of lateral displacement, using two circuits per length of the joint (compared to one) was predicted to lead to smaller error in the estimates of d, l and θ (Table 6.2). Using three circuits was predicted to further reduce the errors in d and

l.

Table 6.2: Model-Predicted Error in Inductance-Based Estimates for a Lateral Displacement of 2 cm

Variable	Number of Circuits 1	2	3
d (mm)	-21.01	-4.88	-2.16
l (mm)	1.22	0.46	0.22
θ (°)	0.59	-0.31	-0.42

6.4 Experimental Evaluation

6.4.1 Calibration and Verification

The pressure P in each bellows is given by a base pressure P_{base} and a relative difference in pressure ΔP to its antagonized counterpart. The pressure differences ΔP_3 and ΔP_2 are used because they actuate v and u respectively with a positive sign.

$$[P_1,\, P_2,\, P_3,\, P_4]^T = P_{\text{base}} + [-\Delta P_3,\, \Delta P_2,\, \Delta P_3,\, -\Delta P_2]^T \tag{6.14}$$

The actuators were calibrated using a continuous 11 minute sequence of ΔP combinations. This resulted in well-distributed combinations of ΔP values (Fig. 6.8b). P_{base} was .2 MPa.

The calibration data were concatenated from data collected with each of the following masses attached to the end of the arm (Fig. 6.8a): 0 kg, 2.3 kg, 4.5 kg, 6.8 kg, 9 kg. The purpose of the added mass was to create a variety of bending conditions for the calibration.

The IMU mounted on the distal plate of the joint provided ground truth measurements of the joint orientation. The IMU measurements were interpreted to find the components of a rotation vector $\hat{\boldsymbol{\omega}} = [\hat{u}, \hat{v}, 0]^T$ by assuming the joint deformation to have constant curvature across its entire length. The inductance values from each

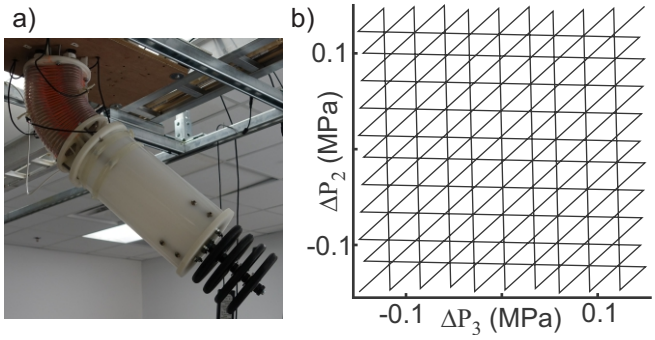

Figure 6.8: a) The joint was mounted upside-down on an elevated fixture. Mass was selectively added to the end of the arm for calibration and testing. Shown is a 9 kg of mass on the end of the arm. b) The combinations of ΔP used to calibrate the joint.

joint half were regressed with two-variable, 4th order polynomials on $u_a = u_b = \hat{u}/2$ and $u_a = u_b = \hat{v}/2$.

The calibration was verified against data taken in identical conditions that were not used in the calibration (Fig. 6.9). The inductance-predicted orientation of the joint was written as a unit vector in 3-space and compared to the orientation measured by the IMU. An inner product was used to determine the error (measured as a single angle) in the estimated orientation (Table 6.3). As predicted by the inductance models, including the data from the adjacent sensors improved the orientation estimates. This is the calibration used in the subsequent experiments (i.e. $v_a = f(L_{1a}, L_{2a})$, $u_a = f(L_{2a}, L_{1a})$, $v_b = f(L_{3b}, L_{4b})$, $u_b = f(L_{4b}, L_{3b})$).

Table 6.3: Experimental Verification of Joint Orientation Calibration

Polynomial Type (4th Order)		**RMSE (°)**
e.g. $v_a = f(L_{1a})$	$v_b = f(L_{3b})$	1.76
e.g. $v_a = f(L_{1a}, L_{2a})$	$v_b = f(L_{3b}, L_{4b})$	**1.11**

6.4.2 Estimation of Lateral Displacement

The purpose of this experiment was to test the ability of the inductance sensors to estimate the end-position of the joint under pure lateral displacement. This type

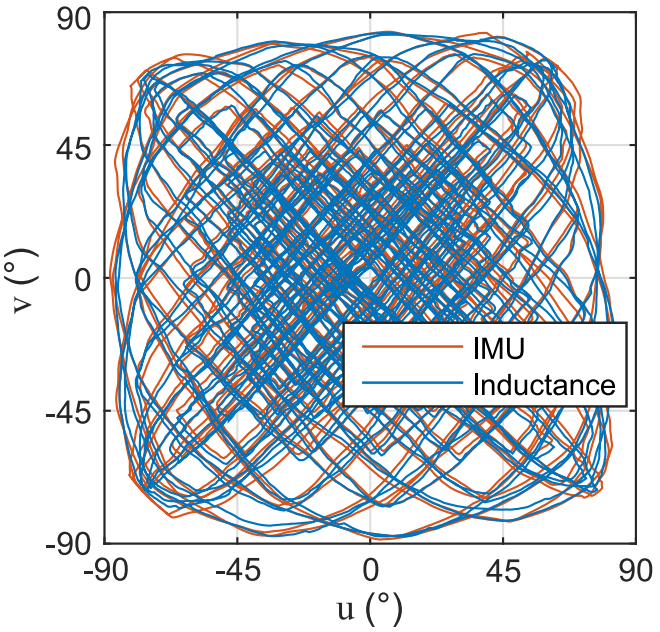

Figure 6.9: The rotation components from the verification data set of the joint calibration. The inductance sensors in each half of the joint were calibrated to predict the bending of the joint in that half. Combining the two halves resulted in an overall orientation estimate (blue). This closely matches the orientation measured by the IMU (red).

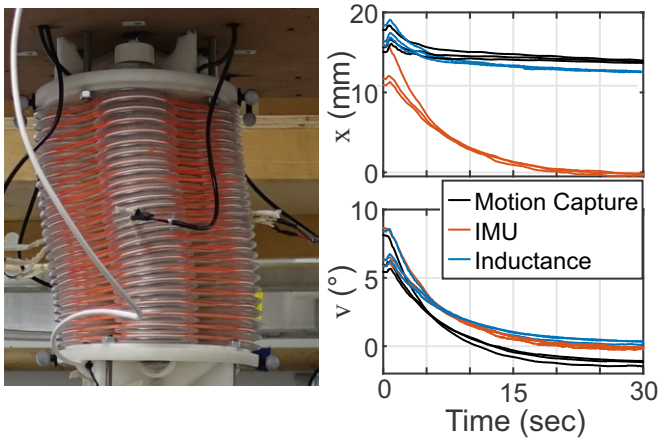

Figure 6.10: The photo shows the level joint with a forced, 14 mm displacement in the direction of bellows 1 (x). In this condition, the bending in one half of the joint is counteracted by bending in the other half. Also shown are the estimates of the lateral displacement x and the orientation v from the three lateral displacement tests. The lateral displacement predicted by the IMU (red) assumes the joint has a constant curvature across its entire length. As the angle of the joint approaches zero, the IMU displacement estimates (red) also approach zero. The inductance-predicted displacement (blue) remains close to the position recorded by the motion capture system (black). The inductance-predicted estimate of the orientation v also remains close to that measured by the IMU (most accurate).

of deformation is unobservable by the IMU. The ground truth in position for this test came from optical markers tracked with an Optitrack V120 Trio camera system (NaturalPoint, Corvalis, OR, USA). The ground truth in orientation came from the IMU. A string tied to the end of the joint was used to deflect the end of the joint towards bellows 1. The end of the joint was leveled by adjusting the bellows pressures until the IMU reported an approximately level configuration (Fig. 6.10). The resulting displacement between the ends of the joint was approximately 14 mm. Estimates of the joint displacement x and orientation v were calculated from the measured inductance values and the calibration identified in Section 6.4.1. The test was repeated three times.

From the onset of motion until the final level condition, the inductance provided

accurate measures of the joint displacement and orientation (Table 6.4, Fig. 6.10). In the final condition, with the joint level and a displacement of 14 mm, the inductance estimate of v had an average error of 0.41 °. The inductance estimate of the displacement in x had an average error of -1.27 mm. The IMU estimate of x had an average error of -14.1 mm.

Table 6.4: Average RMS of Estimation Error of Joint Deformation in the Lateral Displacement Tests

		Feedback Type	
Estimate of	Period	**IMU**	**Inductance**
x (mm)	Entire Test	12.10 (SD 0.38)	1.05 (SD 0.19)
	Final Condition	14.1 (SD 0.25)	1.27 (SD 0.15)
v (°)	Entire Test	Ground Truth	0.31 (SD 0.03)
	Final Condition	Ground Truth	0.41 (SD 0.07)

6.4.3 Feedback Control

The inductance sensors were tested in an orientation controller for the components of the rotation vector, u and v. The corresponding inputs for these components were ΔP_2 and ΔP_3, respectively (Eq. (6.14), $P_{base} = .2$ MPa). The pressure of the actuators was then controlled with electronic pressure regulators (Fig. 6.11). The controller gains were scaled by $a_p = 0.084\,{}^{\text{MPa}}/_{\text{rad}}$. a_p is the slope of a line regressed on the calibration data (0 kg data only) relating the outputs to the inputs (e.g. u to ΔP_2). The error e in each rotation component comes from the difference between the reference input ($_{des}$) and the estimated values ($_{est}$)

$$e_u = u_{\text{des}} - u_{\text{est}} \ , \ e_v = v_{\text{des}} - v_{\text{est}}. \tag{6.15}$$

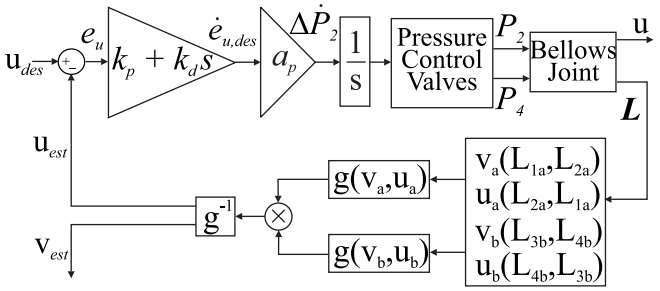

Figure 6.11: The feedback controller for the joint relied on the inductance-based estimates of the rotation components u and v. The performance of this controller was compared to one driven with feedback from the IMU.

The rate-of-change of the commanded pressure differences $\Delta\dot{P}$ depends on this error e and its time derivative $\dot{e}$

$$\Delta\dot{P}_2 = a_p\left(k_p e_u + k_d \dot{e}_u\right)\ ,\ \Delta\dot{P}_3 = a_p\left(k_p e_v + k_d \dot{e}_v\right). \tag{6.16}$$

The feedback was tested under two weight conditions 0 kg ($k_p = 2\,\mathrm{sec}^{-1}$, $k_d = 0$) and 9 kg ($k_p = 2\,\mathrm{sec}^{-1}$, $k_d = 0.1$). The estimates of $\dot{e}$ relied on a linear regression over the last 10 data points in time. The loop period of the LabVIEW-based controller was 15 ms. The reference input was a fixed, pseudo-random sequence of ten step changes in combinations of u and v. The levels of the steps were chosen to be feasible for the given weight condition (60°, 30° and 0° for 0 kg; 25°, 12.5° and 0° for 9 kg). The steps lasted for ten seconds each. The sequence of steps was repeated three times for each condition. The orientation recorded by the IMU was considered ground truth. For comparison, the controller was also tested with feedback from the IMU (instead of the inductance sensors). The same feedback gains and protocol were used in the IMU-controlled tests. The performance of the two feedback types was compared with a paired t-test (paired in each step).

The inductance feedback allowed the joint to track the reference trajectory with

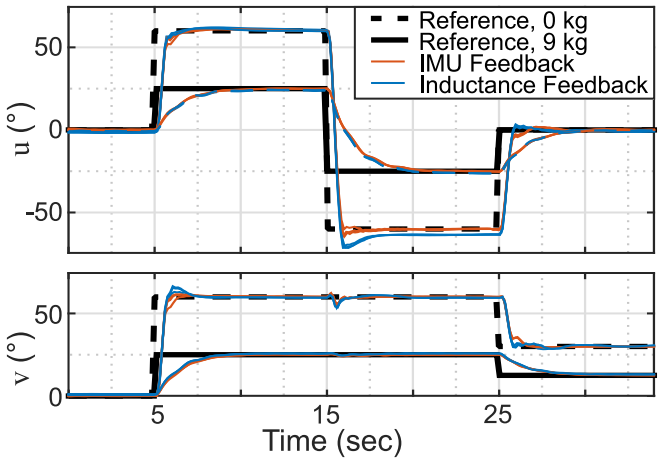

Figure 6.12: The data from the early period of the feedback control experiments. The dashed black line is the reference trajectory for the tests in the 0 kg weight condition. The solid black line corresponds to the 9 kg tests. The blue lines are the three inductance-feedback tests conducted in each weight condition. The tracking performance of the inductance feedback is comparable to that from the IMU (red lines).

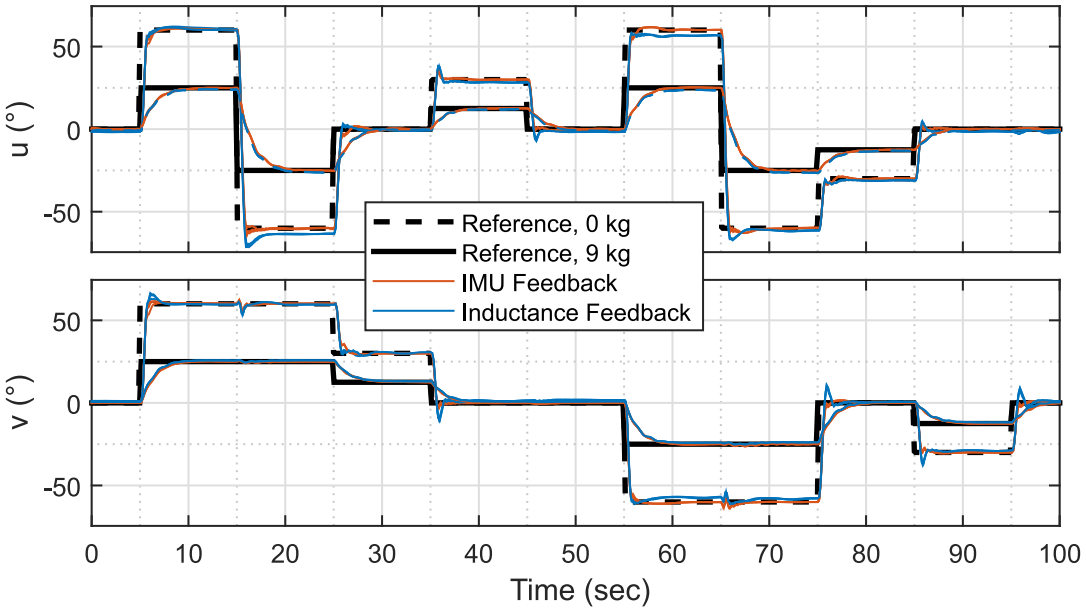

Figure 6.13: The data from the full length of the feedback control experiments. The dashed black line is the reference trajectory for the tests in the 0 kg weight condition. The solid black line corresponds to the 9 kg tests. The blue lines are the three inductance-feedback tests conducted in each weight condition. The tracking performance of the inductance feedback is comparable to that from the IMU (red lines).

similar performance to IMU feedback (Figs. 6.12 and 6.13, Table 6.5).

Table 6.5: Average RMS of Tracking Error (°) in Joint Orientation for Each Reference Step of Feedback Control Trials

Weight	Period	Feedback Type		t-test
		IMU	**Inductance**	p
0 kg	First 5 seconds	13.53 (SD 5.99)	13.79 (SD 6.02)	< 0.05
	Last 5 seconds	**2.48 (SD 1.55)**	**2.98 (SD 1.46)**	< 0.05
9 kg	First 5 seconds	8.18 (SD 3.70)	8.10 (SD 3.55)	$= 0.27$
	Last 5 seconds	**1.02 (SD 0.61)**	**1.30 (SD 0.55)**	< 0.05

6.5 Discussion

This chapter describes the development of a unique, inductance-based sensing system to measure and control the motion of bellows-driven continuum joints. This system is based on changes in mutual inductance between circular coils on the bellows. Verifying the calibration of the experimental sensing system on a separate data set resulted in an orientation error RMS of only 1.11 ° (Fig. 6.9). In contrast to an IMU, the inductance sensors presented in this work can measure joint motion that does not change the relative orientation between the ends of a joint. A lateral displacement of 14 mm was measured by the proposed sensing system with only 1.3 mm of error. The rapid and accurate inductance measurements enabled a feedback controller to orient a 9 kg weight on a manipulator arm with a steady-state error of only 1.3 ° (3 ° with no weight). The performance of the inductance-based feedback controller was similar to an IMU-based controller. The steady-state tracking error of the IMU feedback (which also served as ground truth) was only 0.5 ° smaller in the 0 kg condition and 0.3 ° smaller in the 9 kg condition.

Future work could explore the use of inductance measurements from redundant sensors. The inductance modeling suggests that two sensors on orthogonally located bellows can provide accurate measurements of the two rotation components (u and v).

Accordingly, the experimental sensing system relied on only two orthogonally located sensors in each half of the joint. Measuring the inductance from circuits on all the bellows in a section, however, could improve the signal-to-noise-ratio. Changes in the rotation component v_a, for example, create equal and opposite length changes in the corresponding sections of bellows 1 and 3. Accordingly, the sensitivity of a v_a sensor should approximately double when using the difference of L_{1a} and L_{3a}. Collecting data from redundant sensors on opposite sides of the joint could also allow the system to be accurate even if one side of the joint were in contact with a metal object (which can bias inductance measurements [6]). If multiple inductance-sensing circuits were used in close proximity (e.g. on separate halves of the same bellows), active strategies could be necessary to prevent cross-talk [178].

The inductance-based sensors developed in this chapter bring sensing and control to otherwise difficult-to-sense continuum joints. Unlike discrete joints, continuum joints have no fixed center of rotation on which to affix an encoder. Alternative sensors that have been proposed for continuum joints are often fragile or otherwise poorly-suited for harsh, real-world applications.

Because the continuum joint used in this work has a central cable that does not change length, a two-dimensional curvature sensor could also be used to measure the joint. One well-developed version of a suitable sensor was recently used on the FESTO "BionicMotionRobot" [sic] [78]. The sensor measures the shape of the central cable through a series of LED-phototransistor pairs [77]. Based on the datasheet [179], a sensor of this kind sized for the Pneubotics joint would have an standard deviation of the end-position error of about 0.2 mm. This characterization comes from small deviations from the nominal straight configuration. Compared to the large-deformation calibration of the inductance sensor presented in this work, the LED-based sensor appears to be about an order of magnitude more precise. No large-magnitude deformation data was available for the LED-based curvature sensor.

Additionally, the LED-based sensor has a minimum bend-radius of 10 cm and an outer diameter of about 1 cm [179]. Accordingly, it has limited usefulness for smaller-scale applications.

Self-sensing, bellows-driven continuum joints will enable robots that can create and control compliant yet forceful motions in harsh environments. These unique structures will provide inherently compliant actuation without backlash or stiction. Both the sensors and actuators will be made from lightweight and low-cost components. The flexible structure of the continuum joint will allow the robots to conform to external constraints. The absence of discrete mechanical joints in sensors or actuators will allow them to work in harsh environments where sliding surfaces would be vulnerable. The sensing technology developed in this chapter provides a critical step towards the full implementation of such robotic systems.

CHAPTER VII

Conclusions

This dissertation explores the design and use of inductance-based sensors for the estimation and control of soft robotic systems. This unique sensing strategy is advantageous because it allows designers of soft robotic systems to easily fabricate robust sensors from off-the-shelf materials that are low-cost, lightweight and well-suited for the conditions that soft systems can best exploit. Though the scope of this dissertation is broad–ranging from FREE actuators, McKibben muscles and bellows–in each case a solid contribution to the science has been made. In each application, this work provides design analyses, models, and experimental evaluations to provide understanding to future engineers and scientists who will use inductance sensing in soft robots. As this work demonstrates, inductance-based sensing is a promising technology for these otherwise difficult-to-measure actuators. By combining sensing and actuation into a single component, the ideas presented in this work provide a simple, compact and lightweight way to create and control motion in soft robotic systems. This will enable systems that can interactively engage with their environment and their human counterparts.

7.1 Overview and Contributions

The analyses of inductance-based sensors in Fiber Reinforced Elastomeric Enclosures (FREEs) is enabled by the closed-form kinematic model presented in Chapter II. These unique actuators can provide mechanically-programmable motion to soft systems. The new model presented in this work is one of the significant contributions of this dissertation. The introduction of η and the analytical relationship between the fiber angles given in Eq. (2.6) allows for a closed-form framework for kinematic analysis and design of FREE actuators. Previously published fiber-only models have relied on "instantaneous" kinematics [137] to incrementally update fiber angles. To solve for large deformations with instantaneous kinematics, the nonlinear equations had to be iteratively solved and composed. The model presented in this work provides analytic functions describing the actuator rotation, length, diameter and volume. All of these functions are parameterized by the kinematic state of the actuator given by the angle β. The simplicity of the presented model opens the door for new types of design analyses for FREE actuators (including those conducted in this work). As the understanding of FREEs grows, engineers will find new opportunities for these unique actuators to expand the functional ability of soft, fluid-driven systems.

Chapter III lays the theoretical groundwork for understanding the design and use of Smart Braid sensors in FREEs. The analyses of Chapter III show that Smart Braid sensors can be used to sense the motion of FREE actuators. This chapter develops a general inductance model for two-fiber-family Smart Braid FREEs. This simplified model captures the trends in the inductance change and the effect of design choices such as the number of wires, the electrical configuration (serial vs parallel), and the size of the actuator. The model was validated numerically and experimentally. These design factors are used to scale a numerically identified function $\chi(\eta, \beta)$. This dimensionless function depends only on the ratio η of the fiber lengths and the angle β of one of the fiber families. The inductance model provides insight into the design

choices for Smart Braid sensors. Smart Braid FREEs for which β is close to zero are not well suited to measure actuator motion. Nor are Smart Braid well suited for FREEs in which the fibers have the same chirality ($\beta > 0$) unless one fiber is much longer than the other (η close to zero). The quality factor of the circuit is increased with higher numbers of fibers and larger cross-sectional areas in the conductors. This must be done judiciously, however, because many large fibers can limit the range of motion of the actuator. The *absolute* sensitivity of the inductance to motion is greater when the wires are in a series configuration. Series or parallel wiring, on the other hand, has no effect on the *relative* inductance sensitivity (normalized by the inductance) nor the quality factor or the absolute change in the resonant frequency. A parallel configuration, however, is simpler for an automated manufacturing process.

The Smart Braid sensor was evaluated as a length sensor for a McKibben muscle actuator in Chapter IV. The model for Smart Braid inductance were able to characterize the sensitivity of the actuator to within 8 %. The Smart Braid provided measurements of the actuator contraction that were accurate to within about a millimeter in dynamic and loaded conditions. This was accomplished without any additional mechanical components. The electrically conductive circuit formed by the fibers was the only difference from a standard McKibben muscle. Despite this simplicity, the contraction can be accurately measured with only a linear calibration of the inductance measurements.

Chapter V shows how Smart Braid sensors can be used as feedback for motion control in soft robotic systems. Motion control was demonstrated in both a revolute system and a bending continuum manipulator. For the revolute joint, techniques were developed to compensate for compliance between actuators and points of motion output. These techniques extend to other actuator length-sensing technologies. The results demonstrate that Smart Braids can control the motion of soft robotic systems. In the revolute joint, the Smart Braid feedback resulted in stable angle control with a

steady-state RMS error of 1.5 °. In the continuum manipulator, Smart Braid feedback enabled tracking of the desired tip angle with a steady-state RMS error of 1.25 °.

Chapter VI describes the development of a unique, inductance-based sensing system to measure and control the motion of bellows-driven continuum joints. This system is based on changes in mutual inductance between circular coils on the bellows. The inductance modeling suggests that these sensors work best when the minor diameters of the bellows are separated by an axial distance that is much smaller than the diameter. Additionally, the modeling and experimentation suggests that two sensors on orthogonally located bellows can provide accurate measurements of the two rotation components. Verifying the calibration of the experimental sensing system on a separate data set resulted in an orientation error RMS of only 1.11 °. The inductance sensors were able to measure joint motion that would be unobservable to an IMU. A lateral displacement of 14 mm was measured with only 1.3 mm of error. The rapid and accurate inductance measurements enabled a feedback controller to orient a 9 kg weight on a manipulator arm with a steady-state error of only 1.3 °.

7.2 Limitations, Perspective and Future Opportunities

The work in this dissertation has limited scope. Future work is needed to provide solutions to known weaknesses in the proposed sensing method, to apply the ideas more broadly and to discover unknown weaknesses. The primary known weakness of the method include fabrication methods, fiber fatigue, connection compliance, cross-talk and interference from metal. Understanding these weaknesses can help designers know when inductance-based sensing is appropriate for their application and know how to design the sensing systems accordingly.

The fabrication of the Smart Braid sensors is quite complex. The current Smart Braid fabrication process relies on a 3D-printed template and requires several hours of manual labor. The fabrication of Smart Braids has thus far been limited to only

McKibben muscles. The symmetric structure of these actuators makes it easy to braid their fibers with an automated process. The automated process could be adapted to include conductive fibers [160]. FREEs, on the other hand, are typically made from layered families of thread-like fibers [136]. The fibrous fibers bond well with the elastomer that holds them in place. It is possible that the 3D-printed template method could be adapted to create braided Smart Braid FREEs. If a layered process were used, care would need to be taken to create good bonding between the wire insulation and the elastomer. When the Smart Braids are fabricated manually with a single fiber, there is no need to create electrical junctions between the helix ends. However, in an automated braiding or layered process, electrical junctions need to be formed.

The bellows-sensor fabrication process is simple and straightforward and could readily be integrated into the actuator fabrication process. The wire is simply wrapped around the minor diameters. The minor diameter serves as a "groove" that aligns and groups multiple turns of wire. A winding guide molded into the surface of the actuator would be helpful if the wires were to be wrapped uniformly around the bellows (not just in the minor diameters).

The stress and repeated flexing of the wires can lead to failure. This is particularly true when the fibers are used to transmit forces from the internal pressure. To avoid this, the Smart Braid feedback tests of Chapter V used an internal braid of plastic fibers to transmit the forces. The tinsel wire used in the bellows work (Chapter VI) is designed to have a high flex-life but is not necessarily well-suited to undergo high tensile stress. One promising wire option that has not been tested is highly flexible silver-coated stainless steel wire [180]. This wire is designed for use in jewelry (where repeated flexing and tensile stresses are common). The silver plating could provide the necessary conductivity and the stainless steel the necessary tensile strength.

The stress in McKibben muscle fibers has been modeled and can be used to in-

form the design of Smart Braid circuits. Currently, however, there are no models for the fiber stress in two-fiber-family FREEs. Initial work done by myself and others has indicated that the stress-induced resistance changes in the conductive fibers surrounding a McKibben muscle can be used to measure the internal pressure [3], [160]. More research is necessary to understand how this could be used in conjunction with inductance sensing or adapted for use in FREEs.

The experimental inductance-sensors tested in this work were primarily sensitive to the actuator length. Sensing the length of the actuators directly is powerful because it creates a "servomotor"-like actuator that is the source of both the actuation forces and the feedback. Care must be taken, however, when relating actuator length measurements to estimates of the system motion. Compliance between the sensor location and the point of motion output can bias estimates. External forces can induce strain inbetween these points that is not captured by the sensor. When the sensors are combined with the actuators, for instance, the load transmitted by the actuator to the output can introduce such strains and lead to errors in the estimate of the output position.

The inductance measurements can be affected by external electromagnetic signals. For instance, the signal from one sensor can excite a signal in another. When multiple sensors are used in close proximity, active strategies may be necessary to prevent cross-talk [178]. For instance, the sensors can be made with high quality factors that amplify the resonant frequency of the tank circuit compared to other frequencies. with the "narrow-band" response, the nearby sensors can be paired with different capacitors to create distinct resonant frequencies. Create a narrow-band response can also help reject noise from other nearby emitters. There is no biasing effect from DC magnetic fields that may be near the sensors [181].

The immediate proximity of metal to the sensors can pose challenges. The primary challenge of nearby metal is the bias it can introduce to variable-geometry inductance

sensing. Ferromagnetic materials such as iron, steel or ferrite can raise the sensor inductance. Highly conductive materials such as aluminum and copper can lower the inductance through the magnetic fields of the induced eddy currents. If the position of the metal is fixed relative to the sensor, there is no problem with bias. Though the metal may reduce the sensor quality factor, the effect of the metal can simply be calibrated away. The difficulty arises when the sensor is moving relative to the metal. The metal will cause a change in the sensor inductance without a change in geometry. This will fool the sensing system into believing motion has occurred when it has not.

One possible way to mitigate this effect is to monitor the drive currents of redundant sensors. Both the continuum manipulator and the bellows-driven joint could easily have redundant sensor measurements on the opposite sides of the device. If the nearby metal is conductive enough to have significant eddy-currents, then additional power is necessary to drive the sensor. The inductance-sensing chips used in the feedback control allow the system to monitor the driving current of the sensors [124]. By detecting unusual changes in current, the system could know when to discount the readings from a biased sensor. In the continuum structures, the redundant sensors are on opposite sides of the system. The proposed strategy could be effective because an incidental contact with biasing metal would, in most cases, have a much larger effect on the close sensor than the distant one. Other potential strategies include the use of fixed-geometry inductance sensors to monitor for nearby metal or the use of electromagnetic shielding.

Metal could also be used to enhance the inductance response of the sensors. Adding low-conductivity ferrous material to the core of the sensors could boost the overall inductance (and thus the magnitude of the inductance change). For example, it may be possible to add iron particles to the elastomer or ferrite cores to the bellows. Care would need to be taken not lower the quality of the sensor through the

inevitable "core losses" of the resonant energy.

It may also be possible to adapt the strategies proposed in this work for other applications. For example, the inductance model of Chapter III revealed that the highest sensitivity to length change comes from Smart Braids with very negative values of β. When used to reinforce an elastomeric tube as an actuator, such fibers lead to an extension motion. Suppose, however, that one wished to take advantage of the high sensitivity of a highly-negative-β Smart Braid and the strong contractile force of a contracting McKibben muscle. The high-sensitivity Smart Braid could be used over-top of different fibers that created the contractile motion (similar to the strategy used in Chapter V). This would create a sensor-actuator combination with a higher sensitivity to length change than those tested in this work. It could also be interesting to integrate inductive sensing into other soft structures such as elastomers or clothes to measure motion created from an external source (e.g. the human body). The sensing system for bellows was explored for bellows with circular cross-sections. In other work, I have also characterized the inductance response of inductance sensing for bending bellows [6].

It is difficult to make a direct comparison between the inductance-based sensing strategies proposed in this work and other soft sensing strategies under development. Most of the soft sensing technologies discussed in the introduction to this work are based on measuring strain through additives and modifications to elastomers. The advantage of these elastomer-based techniques is that the sensing systems can be integrated directly into the robot body without appreciably changing the system stiffness. The circuitry for the inductive sensing proposed in this work is designed to be incorporated into soft actuators so that the wires reinforce the system in desirable ways.

The inductance sensing strategy used in this work was used to measure large deformations of the actuators. There is also a great deal of interest in measuring

small tactile deformations in soft robot bodies. For tactile applications, I suspect that elastomer-based resistive, capacitive or optical methods would be better suited.

7.3 Closing

The sensing technology explored in this work will enable the creation of a new class of soft, self-sensing actuators based on inductance. This will enable robots that can create and control compliant yet forceful motions in harsh environments. These unique structures will provide inherently compliant actuation without backlash or stiction. Both the sensors and actuators will be made from lightweight and low-cost components. The flexible structures will allow the robots to conform to external constraints. The absence of discrete mechanical joints in sensors or actuators will allow them to work in harsh environments where sliding surfaces would be vulnerable. This work paves the way for soft robots where both the sensors and the actuators are made from compliant, lightweight and low-cost components. The sensing technology developed in this work provides a critical step towards the full implementation of such robotic systems.

It is only through sensing that soft systems can become true autonomous agents– sensing and reacting to their own, changing environment. Soft robotic systems show great promise in fields as diverse as materials handling, health care, human assistance, agriculture, energy and exploration. These machines will be fundamentally different than their rigid counterparts. This difference will make them uniquely suited to take on the important tasks that have eluded traditional robots. In the soft, natural environments where traditional robots fail, soft robots will excel. Because the flexibility of soft robotics emulates that of animals, soft robots are better suited to work with humans. Lightweight soft robotic manipulators could operate safely alongside human workers. In health care, soft robotic systems could be used to inspect internal organs [182]. Soft robotic orthoses could also provide assistance to the mobility impaired

[183].

Giving soft robots the ability to sense and react to their environment will further accelerate the pace of this growing field. This dissertation has laid the groundwork for inductance-based sensing. As the technology continues to develop, it will expand the applications and capabilities of soft robotic devices.

Bibliography

[1] W. Felt and C. D. Remy, "A closed-form kinematic model for fiber reinforced elastomeric enclosures," *Journal of Mechanisims and Robotics (Under Review)*, 2017.

[2] ——, "Modeling and design of "smart braid" inductance sensors for fiber-reinforced elastomeric enclosures," *In Preparation*, 2017.

[3] W. Felt and C. D. Remy, "Smart braid: Air muscles that measure force and displacement," in *Intelligent Robots and Systems (IROS 2014), 2014 IEEE/RSJ International Conference on*, IEEE, 2014, pp. 2821–2826.

[4] W. Felt, K. Y. Chin, and C. D. Remy, "Contraction sensing with smart braid mckibben muscles," *IEEE/ASME Transactions on Mechatronics*, vol. 21, no. 3, pp. 1201–1209, Jun. 2016, ISSN: 1083-4435. DOI: 10.1109/TMECH.2015.2493782.

[5] ——, "Smart braid feedback for the closed-loop control of soft robotic systems," *Soft Robotics*, 2017.

[6] W. Felt, M. Suen, and C. D. Remy, "Sensing the motion of bellows through changes in mutual inductance," in *Intelligent Robots and Systems (IROS 2016), 2016 IEEE/RSJ International Conference on*, IEEE, 2016.

[7] W. Felt, M. Telleria, T. F. Allen, G. Hein, J. B. Pompa, K. Albert, and C. D. Remy, "An inductance-based sensing system for bellows-driven continuum joints in soft robots," in *Submitted To Robotics Science and Systems XIII*, 2017.

[8] W. Felt and C. D. Remy, *Sensing method for fiber-driven motion systems*, 2015.

[9] Soft Robotics Inc. [Online]. Available: http://www.softroboticsinc.com/.

[10] H. K. Yap, P. M. Khin, T. H. Koh, Y. Sun, X. Liang, J. H. Lim, and C. H. Yeow, "A fully fabric-based bidirectional soft robotic glove for assistance and rehabilitation of hand impaired patients," *IEEE Robotics and Automation Letters*, vol. 2, no. 3, pp. 1383–1390, Jul. 2017, ISSN: 2377-3766. DOI: 10.1109/LRA.2017.2669366.

[11] ROAM Robotics. [Online]. Available: https://roamrobotics.com/.

[12] R. Pfeifer, M. Lungarella, and F. Iida, "The challenges ahead for bio-inspired'soft'robotics," *Communications of the ACM*, vol. 55, no. 11, pp. 76–87, 2012.

[13] S. Kim, C. Laschi, and B. Trimmer, "Soft robotics: A bioinspired evolution in robotics," *Trends in biotechnology*, vol. 31, no. 5, pp. 287–294, 2013.

[14] D. Rus and M. T. Tolley, "Design, fabrication and control of soft robots," *Nature*, vol. 521, no. 7553, pp. 467–475, 2015.

[15] S. Sanan, "Soft inflatable robots for safe physical human interaction," PhD thesis, Carnegie Mellon University, 2013.

[16] *Soft robotics soft adaptive gripper*, 2015. [Online]. Available: http://www.roboticsbusinessreview.com/article/soft_robotics_soft_adaptive_gripper.

[17] K. C. Galloway, K. P. Becker, B. Phillips, J. Kirby, S. Licht, D. Tchernov, R. J. Wood, and D. F. Gruber, "Soft robotic grippers for biological sampling on deep reefs," *Soft Robotics*, Jan. 2016, ISSN: 2169-5172. DOI: 10.1089/soro.2015.0019. [Online]. Available: http://dx.doi.org/10.1089/soro.2015.0019.

[18] Sunfolding. [Online]. Available: http://www.sunfolding.com/.

[19] C. Laschi and M. Cianchetti, "Soft robotics: New perspectives for robot bodyware and control," *Frontiers in bioengineering and biotechnology*, vol. 2, 2014.

[20] OCTOPUS Integrating Project, 2009. [Online]. Available: http://www.octopus-project.eu/.

[21] RoboSoft Collaborative Action, 2013. [Online]. Available: http://www.robosoftca.eu/.

[22] Soft Manipulation (SoMa) Project, 2013. [Online]. Available: http://soma-project.eu/.

[23] Soft Robotics Toolkit. [Online]. Available: http://softroboticstoolkit.com/.

[24] Otherlab. [Online]. Available: https://otherlab.com/.

[25] R. F. Shepherd, F. Ilievski, W. Choi, S. A. Morin, A. A. Stokes, A. D. Mazzeo, X. Chen, M. Wang, and G. M. Whitesides, "Multigait soft robot," *Proceedings of the National Academy of Sciences*, vol. 108, no. 51, pp. 20 400–20 403, 2011.

[26] A. D. Marchese, C. D. Onal, and D. Rus, "Autonomous soft robotic fish capable of escape maneuvers using fluidic elastomer actuators," *Soft Robotics*, vol. 1, no. 1, pp. 75–87, 2014.

[27] P. Polygerinos, Z. Wang, K. C. Galloway, R. J. Wood, and C. J. Walsh, "Soft robotic glove for combined assistance and at-home rehabilitation," *Robotics and Autonomous Systems*, vol. 73, pp. 135–143, 2015, Wearable Robotics, ISSN: 0921-8890. DOI: http://dx.doi.org/10.1016/j.robot.2014.08.014. [Online]. Available: http://www.sciencedirect.com/science/article/pii/S0921889014001729.

[28] K. C. Galloway, K. P. Becker, B. Phillips, J. Kirby, S. Licht, D. Tchernov, R. J. Wood, and D. F. Gruber, "Soft robotic grippers for biological sampling on deep reefs," *Soft Robotics*, vol. 3, no. 1, pp. 23–33, 2016.

[29] RoboSoft Grand Challenge, 2016. [Online]. Available: http://www.robosoftca.eu/events/robosoft-grand-challenge.

[30] D. Trivedi, C. D. Rahn, W. M. Kier, and I. D. Walker, "Soft robotics: Biological inspiration, state of the art, and future research," *Applied Bionics and Biomechanics*, vol. 5, no. 3, pp. 99–117, 2008.

[31] G. Pratt and M. M. Williamson, "Series elastic actuators," in *Intelligent Robots and Systems 95.'Human Robot Interaction and Cooperative Robots', Proceedings. 1995 IEEE/RSJ International Conference on*, IEEE, vol. 1, 1995, pp. 399–406.

[32] G. Pratt and M. Williamson, *Elastic actuator for precise force control*, US Patent 5,650,704, Jul. 1997. [Online]. Available: http://www.google.com/patents/US5650704.

[33] C. Majidi, "Soft robotics: A perspectivecurrent trends and prospects for the future," *Soft Robotics*, vol. 1, no. 1, pp. 5–11, 2014.

[34] A. De Greef, P. Lambert, and A. Delchambre, "Towards flexible medical instruments: Review of flexible fluidic actuators," *Precision engineering*, vol. 33, no. 4, pp. 311–321, 2009.

[35] B. Mosadegh, P. Polygerinos, C. Keplinger, S. Wennstedt, R. F. Shepherd, U. Gupta, J. Shim, K. Bertoldi, C. J. Walsh, and G. M. Whitesides, "Pneumatic networks for soft robotics that actuate rapidly," *Advanced Functional Materials*, vol. 24, no. 15, pp. 2163–2170, 2014.

[36] J. Bishop-Moser and S. Kota, "Design and modeling of generalized fiber-reinforced pneumatic soft actuators," *Robotics, IEEE Transactions on*, vol. 31, no. 3, pp. 536–545, 2015.

[37] P. Polygerinos, Z. Wang, J. T. Overvelde, K. C. Galloway, R. J. Wood, K. Bertoldi, and C. J. Walsh, "Modeling of soft fiber-reinforced bending actuators," *Robotics, IEEE Transactions on*, 2015.

[38] F. Daerden and D. Lefeber, "Pneumatic artificial muscles: Actuators for robotics and automation," *European journal of mechanical and environmental engineering*, vol. 47, no. 1, pp. 11–21, 2002.

[39] S. Konishi, F. Kawai, and P. Cusin, "Thin flexible end-effector using pneumatic balloon actuator," *Sensors and Actuators A: Physical*, vol. 89, no. 1, pp. 28–35, 2001.

[40] A. J. Veale, I. A. Anderson, and S. Q. Xie, "The smart peano fluidic muscle: A low profile flexible orthosis actuator that feels pain," in *SPIE Smart Structures and Materials+ Nondestructive Evaluation and Health Monitoring*, International Society for Optics and Photonics, 2015, pp. 94351V–94351V.

[41] A. D. Marchese, K. Komorowski, C. D. Onal, and D. Rus, "Design and control of a soft and continuously deformable 2d robotic manipulation system," in *Robotics and Automation (ICRA), 2014 IEEE International Conference on*, IEEE, 2014, pp. 2189–2196.

[42] A. D. Marchese and D. Rus, "Design, kinematics, and control of a soft spatial fluidic elastomer manipulator," *The International Journal of Robotics Research*, 2015. DOI: 10.1177/0278364915587925.

[43] C. M. Best, J. P. Wilson, and M. D. Killpack, "Control of a pneumatically actuated, fully inflatable, fabric-based, humanoid robot," in *Humanoid Robots (Humanoids), 2015 IEEE-RAS 15th International Conference on*, IEEE, 2015, pp. 1133–1140.

[44] J. Ueda, D. Ming, and V. Krishnamoorthy, "Individual muscle control using an exoskeleton robot for muscle function testing," *Neural Systems and Rehabilitation Engineering, IEEE Transactions on*, vol. 18, no. 4, pp. 339–50, Aug. 2010, ISSN: 1558-0210. DOI: 10.1109/TNSRE.2010.2047116. [Online]. Available: http://www.ncbi.nlm.nih.gov/pubmed/20363684.

[45] G. S. Sawicki and D. P. Ferris, "A pneumatically powered knee-ankle-foot orthosis (kafo) with myoelectric activation and inhibition," *Journal of neuroengineering and rehabilitation*, vol. 6, no. 1, p. 23, Jan. 2009, ISSN: 1743-0003. DOI: 10.1186/1743-0003-6-23. [Online]. Available: http://www.pubmedcentral.nih.gov/articlerender.fcgi?artid=2717982%5C&tool=pmcentrez%5C&rendertype=abstract.

[46] M. Wehner, B. Quinlivan, P. M. Aubin, E. Martinez-Villalpando, M. Baumann, L. Stirling, K. Holt, R. Wood, and C. Walsh, "A lightweight soft exosuit for gait assistance," in *Robotics and Automation (ICRA), 2013 IEEE International Conference on*, IEEE, 2013, pp. 3362–3369.

[47] T. Ando, Y. Kobayashi, J. Okamoto, M. Takahashi, and M. G. Fujie, "Intelligent trunk corset to support rollover of cancer bone metastasis patients," *Mechatronics, IEEE/ASME Transactions on*, vol. 15, no. 2, pp. 181–190, 2010.

[48] A. Yates and J. Selan, *Positional tracking systems and methods*, US Patent 20,160,131,761, May 2016.

[49] T. Ochi, "A positioning system for mobile robots using symmetrical rotating laser beams," *Advanced Robotics*, vol. 4, no. 3, pp. 217–222, 1989.

[50] R. Xu, A. Asadian, A. S. Naidu, and R. V. Patel, "Position control of concentric-tube continuum robots using a modified jacobian-based approach," in *Robotics and Automation (ICRA), 2013 IEEE International Conference on*, IEEE, 2013, pp. 5813–5818.

[51] R. S. Penning, J. Jung, N. J. Ferrier, and M. R. Zinn, "An evaluation of closed-loop control options for continuum manipulators," in *Robotics and Automation (ICRA), 2012 IEEE International Conference on*, 2012, pp. 5392–5397. DOI: 10.1109/ICRA.2012.6224735.

[52] A. Yassin, Y. Nasser, M. Awad, A. Al-Dubai, R. Liu, C. Yuen, and R. Raulefs, "Recent advances in indoor localization: A survey on theoretical approaches and applications," *IEEE Communications Surveys & Tutorials*, 2016.

[53] Y. Gu, A. Lo, and I. Niemegeers, "A survey of indoor positioning systems for wireless personal networks," *IEEE Communications surveys & tutorials*, vol. 11, no. 1, pp. 13–32, 2009.

[54] E. R. Bachmann, I. Duman, U. Y. Usta, R. B. McGhee, X. P. Yun, and M. J. Zyda, "Orientation tracking for humans and robots using inertial sensors," in *Computational Intelligence in Robotics and Automation, 1999. CIRA '99. Proceedings. 1999 IEEE International Symposium on*, 1999, pp. 187–194. DOI: 10.1109/CIRA.1999.810047.

[55] M. T. Gillespie, C. M. Best, and M. D. Killpack, "Simultaneous position and stiffness control for an inflatable soft robot," in *2016 IEEE International Conference on Robotics and Automation (ICRA)*, May 2016, pp. 1095–1101. DOI: 10.1109/ICRA.2016.7487240.

[56] W. de Vries, H. Veeger, C. Baten, and F. van der Helm, "Magnetic distortion in motion labs, implications for validating inertial magnetic sensors," *Gait & Posture*, vol. 29, no. 4, pp. 535–541, 2009, ISSN: 0966-6362. DOI: http://dx.doi.org/10.1016/j.gaitpost.2008.12.004. [Online]. Available: http://www.sciencedirect.com/science/article/pii/S0966636208003858.

[57] E. R. Bachmann, X. Yun, and C. W. Peterson, "An investigation of the effects of magnetic variations on inertial/magnetic orientation sensors," in *Robotics and Automation, 2004. Proceedings. ICRA '04. 2004 IEEE International Conference on*, vol. 2, Apr. 2004, 1115–1122 Vol.2. DOI: 10.1109/ROBOT.2004.1307974.

[58] R. Niiyama, A. Nagakubo, and Y. Kuniyoshi, "Mowgli: A bipedal jumping and landing robot with an artificial musculoskeletal system," in *ICRA, 2007*, IEEE, 2007, pp. 2546–2551.

[59] B. Verrelst, R. Van Ham, B. Vanderborght, F. Daerden, D. Lefeber, and J. Vermeulen, "The pneumatic biped lucy actuated with pleated pneumatic artificial muscles," *Autonomous Robots*, vol. 18, no. 2, pp. 201–213, 2005.

[60] B. Tondu, S. Ippolito, J. Guiochet, and A. Daidie, "A seven-degrees-of-freedom robot-arm driven by pneumatic artificial muscles for humanoid robots," *The International Journal of Robotics Research*, vol. 24, no. 4, pp. 257–274, 2005.

[61] Z. Sun, G. Bao, Q. Yang, and Z. Wang, "Design of a novel force feedback dataglove based on pneumatic artificial muscles," in *Mechatronics and Automation, Proceedings of the 2006 IEEE International Conference on*, IEEE, 2006, pp. 968–972.

[62] C. K. Robinson, N. Wereley, and C. Kothera, "Control of a heavy-lift robotic manipulator with pneumatic artificial muscles," in *AIAA Structures, Structural Dynamics, and Materials Conference, Honolulu, HI*, 2012.

[63] T. Reininger, *Contractile unit having a position sensor means*, US Patent 7,104,182, Sep. 2006.

[64] ——, *Kontraktionseinheit mit positionssensoreinrichtung*, Patent Application DE10225245A1, Jun. 2002.

[65] T. Akagi, S. Dohta, Y. Kenmotsu, S. Jinno, and K.-i. Taniguchi, "Model based axial displacement measurement of rubber artificial muscle using inner diameter sensor," in *Proceedings of the 2nd International Conference on Intelligent Technologies and Engineering Systems (ICITES2013)*, Springer International Publishing, 2014, pp. 349–357.

[66] M. D. Grissom, V. Chitrakaran, D. Dienno, M. Csencits, M. Pritts, B. Jones, W. McMahan, D. Dawson, C. Rahn, and I. Walker, "Design and experimental testing of the octarm soft robot manipulator," in *Defense and Security Symposium*, International Society for Optics and Photonics, 2006, 62301F–62301F.

[67] Festo, *Bionic handling assistant*, 2010. [Online]. Available: `http://www.festo.com/cms/en_corp/9655_10218.htm`.

[68] R. Strommer, *Kontraktionseinheit*, Patent Application DE102005017696A1, Apr. 2005.

[69] E. Szelitzky, J. Kuklyte, D. Mândru, and N. OConnor, "Low cost angular displacement sensors for biomechanical applications-a review," *Journal of Biomedical Engineering and Technology*, vol. 2, no. 2, pp. 21–28, 2014.

[70] C. G. Askins, G. A. Miller, and E. J. Friebele, "Bend and twist sensing in a multiple-core optical fiber," in *Optical Fiber Communication Conference/National Fiber Optic Engineers Conference*, Optical Society of America, 2008, OMT3. [Online]. Available: `http://www.osapublishing.org/abstract.cfm?URI=OFC-2008-OMT3`.

[71] R. J. Roesthuis, S. Janssen, and S. Misra, "On using an array of fiber bragg grating sensors for closed-loop control of flexible minimally invasive surgical instruments," in *2013 IEEE/RSJ International Conference on Intelligent Robots and Systems*, Nov. 2013, pp. 2545–2551. DOI: `10.1109/IROS.2013.6696715`.

[72] M. K. Dobrzynski, R. Pericet-Camara, and D. Floreano, "Contactless deflection sensor for soft robots," in *Intelligent Robots and Systems (IROS), 2011 IEEE/RSJ International Conference on*, IEEE, 2011, pp. 1913–1918.

[73] S. Sareh, Y. Noh, M. Li, T. Ranzani, H. Liu, and K. Althoefer, "Macrobend optical sensing for pose measurement in soft robot arms," *Smart Materials and Structures*, vol. 24, no. 12, p. 125 024, 2015.

[74] S. Ozel, N. A. Keskin, D. Khea, and C. D. Onal, "A precise embedded curvature sensor module for soft-bodied robots," *Sensors and Actuators A: Physical*, vol. 236, pp. 349–356, 2015.

[75] Y. Shapiro, G. Ksa, and A. Wolf, "Shape tracking of planar hyper-flexible beams via embedded pvdf deflection sensors," *IEEE/ASME Transactions on Mechatronics*, vol. 19, no. 4, pp. 1260–1267, Aug. 2014, ISSN: 1083-4435.

[76] Z. Wang and S. Hirai, "A 3d printed soft gripper integrated with curvature sensor for studying soft grasping," in *System Integration (SII), 2016 IEEE/SICE International Symposium on*, IEEE, 2016, pp. 629–633.

[77] T. S. GmbH, *Innovative cable-like-shape-sensor*, Accessed April 2017. [Online]. Available: `http://www.tst-inno.de/en/SAC.html`.

[78] Festo, *Bionicmotionrobot*, Mar. 2017. [Online]. Available: `https://www.festo.com/group/en/cms/12747.htm`.

[79] G. Miron and J.-S. Plante, "Design of a durable air-muscle with integrated sensor for soft robotics," in *ASME 2015 International Design Engineering Technical Conferences and Computers and Information in Engineering Conference*, American Society of Mechanical Engineers, 2015, V009T07A088–V009T07A088.

[80] S. Wakimoto, K. Suzumori, and T. Kanda, "Development of intelligent mckibben actuator with built-in soft conductive rubber sensor," in *Solid-State Sensors, Actuators and Microsystems, 2005. Digest of Technical Papers. TRANSDUCERS'05. The 13th International Conference on*, IEEE, vol. 1, 2005, pp. 745–748.

[81] Y.-L. Park and R. J. Wood, "Smart pneumatic artificial muscle actuator with embedded microfluidic sensing," in *Sensors, 2013 IEEE*, IEEE, 2013, pp. 1–4.

[82] *Positionssensoreinrichtung für eine einen kontraktionsschlauch aufweisende kontraktionseinheit*, Patent DE202004014305U1, Sep. 2004.

[83] S. Kuriyama, M. Ding, Y. Kurita, T. Ogasawara, and J. Ueda, "Flexible sensor for mckibben pneumatic actuator," *Sensors, 2009 IEEE*, pp. 520–525, 2009.

[84] T. Reininger, *Contraction unit with position sensor device*, US Patent 6,807,894, Oct. 2004.

[85] C. To, T. Hellebrekers, and Y.-L. Park, "Highly stretchable optical sensors for pressure, strain, and curvature measurement," in *Intelligent Robots and Systems (IROS), 2015 IEEE/RSJ International Conference on*, Sep. 2015, pp. 5898–5903. DOI: `10.1109/IROS.2015.7354215`.

[86] H. Zhao, K. O'Brien, S. Li, and R. F. Shepherd, "Optoelectronically innervated soft prosthetic hand via stretchable optical waveguides," *Science Robotics*, vol. 1, no. 1, 2016. DOI: `10.1126/scirobotics.aai7529`. eprint: `http://robotics.sciencemag.org/content/1/1/eaai7529.full.pdf`. [Online]. Available: `http://robotics.sciencemag.org/content/1/1/eaai7529`.

[87] K. J. Loh, J. P. Lynch, B. Shim, and N. Kotov, "Tailoring piezoresistive sensitivity of multilayer carbon nanotube composite strain sensors," *Journal of Intelligent Material Systems and Structures*, vol. 19, no. 7, pp. 747–764, 2008.

[88] M.-A. Lacasse, V. Duchaine, and C. Gosselin, "Characterization of the electrical resistance of carbon-black-filled silicone: Application to a flexible and stretchable robot skin," in *Robotics and Automation (ICRA), 2010 IEEE International Conference on*, IEEE, 2010, pp. 4842–4848.

[89] J. Zhu, S. Wei, J. Ryu, and Z. Guo, "Strain-sensing elastomer/carbon nanofiber metacomposites," *The Journal of Physical Chemistry C*, vol. 115, no. 27, pp. 13 215–13 222, 2011.

[90] U. Culha, S. G. Nurzaman, F. Clemens, and F. Iida, "Svas3: Strain vector aided sensorization of soft structures," *Sensors*, vol. 14, no. 7, pp. 12 748–12 770, 2014.

[91] J. T. Muth, D. M. Vogt, R. L. Truby, Y. Mengüç, D. B. Kolesky, R. J. Wood, and J. A. Lewis, "Embedded 3d printing of strain sensors within highly stretchable elastomers," *Advanced Materials*, vol. 26, no. 36, pp. 6307–6312, 2014.

[92] P. Wang and T. Ding, "Creep of electrical resistance under uniaxial pressures for carbon blacksilicone rubber composite," English, *Journal of Materials Science*, vol. 45, no. 13, pp. 3595–3601, 2010, ISSN: 0022-2461. DOI: 10.1007/s10853-010-4405-8. [Online]. Available: http://dx.doi.org/10.1007/s10853-010-4405-8.

[93] N. Stbler, J. Fritzsche, and M. Klppel, "Mechanical and electrical analysis of carbon black networking in elastomers under strain," *Polymer Engineering & Science*, vol. 51, no. 6, pp. 1206–1217, 2011, ISSN: 1548-2634. DOI: 10.1002/pen.21888. [Online]. Available: http://dx.doi.org/10.1002/pen.21888.

[94] J. Bergstrm and M. Boyce, "Constitutive modeling of the large strain time-dependent behavior of elastomers," *Journal of the Mechanics and Physics of Solids*, vol. 46, no. 5, pp. 931–954, 1998, ISSN: 0022-5096. DOI: http://dx.doi.org/10.1016/S0022-5096(97)00075-6. [Online]. Available: http://www.sciencedirect.com/science/article/pii/S0022509697000756.

[95] S. Hirai, "Measuring mckibben actuator shrinkage using fiber sensor," in *Robot and Human Interactive Communication (RO-MAN), 2015 24th IEEE International Symposium on*, IEEE, 2015, pp. 628–633.

[96] J. Zhao and A. Abbas, "A low-cost soft coiled sensor for soft robots," in *ASME 2016 Dynamic Systems and Control Conference*, American Society of Mechanical Engineers, 2016, V002T26A006–V002T26A006.

[97] T. Giffney, M. Xie, A. Yong, A. Wong, P. Mousset, A. McDaid, and K. Aw, "Soft pneumatic bending actuator with integrated carbon nanotube displacement sensor," *Robotics*, vol. 5, no. 1, p. 7, 2016.

[98] K. Kure, T. Kanda, K. Suzumori, and S. Wakimoto, "Intelligent fma using flexible displacement sensor with paste injection," in *Robotics and Automation, 2006. ICRA 2006. Proceedings 2006 IEEE International Conference on*, IEEE, 2006, pp. 1012–1017.

[99] D. M. Vogt, Y.-L. Park, and R. J. Wood, "Design and characterization of a soft multi-axis force sensor using embedded microfluidic channels," *Sensors Journal, IEEE*, vol. 13, no. 10, pp. 4056–4064, 2013.

[100] R. J. Whitney, "The measurement of volume changes in human limbs," *The Journal of Physiology*, vol. 121, no. 1, pp. 1–27, 1953, ISSN: 1469-7793. DOI: 10.1113/jphysiol.1953.sp004926. [Online]. Available: http://dx.doi.org/10.1113/jphysiol.1953.sp004926.

[101] J.-B. Chossat, Y.-L. Park, R. J. Wood, and V. Duchaine, "A soft strain sensor based on ionic and metal liquids," *Sensors Journal, IEEE*, vol. 13, no. 9, pp. 3405–3414, 2013.

[102] N. Farrow and N. Correll, "A soft pneumatic actuator that can sense grasp and touch," in *Intelligent Robots and Systems (IROS), 2015 IEEE/RSJ International Conference on*, IEEE, 2015, pp. 2317–2323.

[103] J. Morrow, H. S. Shin, C. Phillips-Grafflin, S. H. Jang, J. Torrey, R. Larkins, S. Dang, Y. L. Park, and D. Berenson, "Improving soft pneumatic actuator fingers through integration of soft sensors, position and force control, and rigid fingernails," in *2016 IEEE International Conference on Robotics and Automation (ICRA)*, May 2016, pp. 5024–5031. DOI: 10.1109/ICRA.2016.7487707.

[104] D. Y. Choi, M. H. Kim, Y. Oh, S.-H. Jung, J. H. Jung, H. J. Sung, H.-W. Lee, and H. M. Lee, "Highly stretchable, hysteresis-free ionic liquid-based strain sensor for precise human motion monitoring," *ACS Applied Materials & Interfaces*, 2016.

[105] M. D. Dickey, R. C. Chiechi, R. J. Larsen, E. A. Weiss, D. A. Weitz, and G. M. Whitesides, "Eutectic gallium-indium (egain): A liquid metal alloy for the formation of stable structures in microchannels at room temperature," *Advanced Functional Materials*, vol. 18, no. 7, pp. 1097–1104, 2008.

[106] J. Vila, P. Gines, J. Pico, C. Franjo, E. Jimenez, L. Varela, and O. Cabeza, "Temperature dependence of the electrical conductivity in emim-based ionic liquids: Evidence of vogel–tamman–fulcher behavior," *Fluid Phase Equilibria*, vol. 242, no. 2, pp. 141–146, 2006.

[107] H. O. Michaud, L. Dejace, S. de Mulatier, and S. P. Lacour, "Design and functional evaluation of an epidermal strain sensing system for hand tracking," in *2016 IEEE/RSJ International Conference on Intelligent Robots and Systems (IROS)*, Oct. 2016, pp. 3186–3191. DOI: 10.1109/IROS.2016.7759492.

[108] A. Frutiger, J. T. Muth, D. M. Vogt, Y. Mengüç, A. Campo, A. D. Valentine, C. J. Walsh, and J. A. Lewis, "Capacitive soft strain sensors via multicore–shell fiber printing," *Advanced Materials*, vol. 27, no. 15, pp. 2440–2446, 2015.

[109] H. S. Shin, A. Charalambides, I. Penskiy, and S. Bergbreiter, "A soft microfabricated capacitive sensor for high dynamic range strain sensing," in *2016 IEEE/RSJ International Conference on Intelligent Robots and Systems (IROS)*, Oct. 2016, pp. 5572–5578. DOI: 10.1109/IROS.2016.7759819.

[110] A. J. Veale, I. A. Anderson, and S. Q. Xie, "Dielectric elastomer strain and pressure sensing enable reactive fluidic artificial muscles," in *SPIE Smart Structures and Materials+ Nondestructive Evaluation and Health Monitoring*, International Society for Optics and Photonics, 2016, 97982A–97982A.

[111] T. McKay, B. OBrien, E. Calius, and I. Anderson, "Self-priming dielectric elastomer generators," *Smart Materials and Structures*, vol. 19, no. 5, p. 055 025, 2010.

[112] S. J. A. Koh, C. Keplinger, T. Li, S. Bauer, and Z. Suo, "Dielectric elastomer generators: How much energy can be converted?" *Mechatronics, IEEE/ASME Transactions on*, vol. 16, no. 1, pp. 33–41, 2011.

[113] I. A. Anderson, T. A. Gisby, T. G. McKay, B. M. OBrien, and E. P. Calius, "Multi-functional dielectric elastomer artificial muscles for soft and smart machines," *Journal of Applied Physics*, vol. 112, no. 4, p. 041 101, 2012.

[114] A. York and S. Seelecke, "Towards self-sensing of deap actuators: Capacitive sensing experimental analysis," in *ASME 2010 Conference on Smart Materials, Adaptive Structures and Intelligent Systems*, American Society of Mechanical Engineers, 2010, pp. 307–314.

[115] C. Jean-Mistral, A. Sylvestre, S. Basrour, and J. Chaillout, "Dielectric properties of polyacrylate thick films used in sensors and actuators," *Smart materials and structures*, vol. 19, no. 7, p. 075 019, 2010.

[116] StretchSense, *Stretchsense evaluation kit datasheet*, Jun. 2015. [Online]. Available: `http://stretchsense.com/wp-content/uploads/2015/06/Stretch-Sensor-Datasheet.pdf`.

[117] P. P. Regtien, *Sensors for mechatronics*. Elsevier, 2012.

[118] M. De Volder, J. Coosemans, R. Puers, and D. Reynaerts, "Characterization and control of a pneumatic microactuator with an integrated inductive position sensor," *Sensors and Actuators A: Physical*, vol. 141, no. 1, pp. 192–200, 2008.

[119] W. Y. Du, *Resistive, Capacitive, Inductive, and Magnetic Sensor Technologies*. CRC Press, 2014.

[120] J. M. Rebello, F. Kojima, and T. Chady, *Electromagnetic Nondestructive Evaluation (XVI)*. IOS Press, 2013, vol. 38.

[121] B. Beihoff, "A survey of torque transduction methodologies for industrial applications," in *Pulp and Paper Industry Technical Conference, 1996., Conference Record of 1996 Annual*, IEEE, 1996, pp. 220–229.

[122] M. A. Peshkin and W. A. Lorenz, *Method and apparatus for force sensors*, US Patent 6,868,746, Mar. 2005.

[123] R&D Magazine, *An industry first*, 2014. [Online]. Available: `http://www.rdmag.com/award-winners/2014/08/industry-first`.

[124] Texas Instruments, *Ldc1000 inductance-to-digital converter, datasheet (rev. b)*, 2015. [Online]. Available: `http://www.ti.com/lit/ds/symlink/ldc1000.pdf`.

[125] Q.-A. Huang, L. Dong, and L.-F. Wang, "Lc passive wireless sensors toward a wireless sensing platform: Status, prospects, and challenges," *Journal of Microelectromechanical Systems*, vol. 25, no. 5, pp. 822–841, 2016.

[126] O. Erin, N. Pol, L. Valle, and Y. L. Park, "Design of a bio-inspired pneumatic artificial muscle with self-contained sensing," in *2016 38th Annual International Conference of the IEEE Engineering in Medicine and Biology Society (EMBC)*, Aug. 2016, pp. 2115–2119. DOI: 10.1109/EMBC.2016.7591146.

[127] R. Rahimi, M. Ochoa, W. Yu, and B. Ziaie, "A sewing-enabled stitch-and-transfer method for robust, ultra-stretchable, conductive interconnects," *Journal of Micromechanics and Microengineering*, vol. 24, no. 9, p. 095 018, 2014.

[128] E. D. Schneider and H.-J. Diekmann, *Luftfeder mit einem einen elektrischen leiter aufweisenden luftfederbalg*, Patent Application DE4413559A1, Apr. 1994. [Online]. Available: https://patents.google.com/patent/DE4413559A1/en.

[129] S. Reck, T. Pehmuller, and C. Bank, *Pneumatic spring provided with a level measuring device*, US Patent 7,837,181, Nov. 2010. [Online]. Available: https://www.google.com/patents/US7837181.

[130] H. Behrends, *Air spring having two end members and a distance sensor mounted therebetween*, US Patent 6,375,168, Apr. 2002. [Online]. Available: https://www.google.com/patents/US6375168.

[131] C. Bank, T. Pehmueller, and S. Reck, *Luftfeder mit niveaumesseinrichtung*, Patent Application WO2004109150A1, Apr. 2004. [Online]. Available: https://patents.google.com/patent/WO2004109150A1/en.

[132] L. May, *Non-contact power supply for height sensor with single cable*, US Patent App. 14/248,708, Oct. 2014. [Online]. Available: http://www.google.com/patents/US20140306388.

[133] TORQUE AND MORE GMBH, *Smart air springs*. [Online]. Available: http://www.tam-sensors.com/technology/smart-air-springs/.

[134] M. Agerholm and A. Lord, "The artificial muscle of mckibben," *The Lancet*, vol. 277, no. 7178, pp. 660–661, 1961, Originally published as Volume 1, Issue 7178, ISSN: 0140-6736. DOI: http://dx.doi.org/10.1016/S0140-6736(61)91676-2. [Online]. Available: //www.sciencedirect.com/science/article/pii/S0140673661916762.

[135] G. Andrikopoulos, G. Nikolakopoulos, and S. Manesis, "A survey on applications of pneumatic artificial muscles," in *Control Automation (MED), 2011 19th Mediterranean Conference on*, Jun. 2011, pp. 1439–1446. DOI: 10.1109/MED.2011.5982983.

[136] J. L. Bishop-Moser, "Design of generalized fiber-reinforced elasto-fluidic systems," PhD thesis, University of Michigan, 2014.

[137] G. Krishnan, J. Bishop-Moser, C. Kim, and S. Kota, "Kinematics of a generalized class of pneumatic artificial muscles," *Journal of Mechanisms and Robotics*, vol. 7, no. 4, p. 041 014, 2015.

[138] F. Connolly, P. Polygerinos, C. J. Walsh, and K. Bertoldi, "Mechanical programming of soft actuators by varying fiber angle," *Soft Robotics*, vol. 2, no. 1, pp. 26–32, 2015.

[139] F. Connolly, C. J. Walsh, and K. Bertoldi, "Automatic design of fiber-reinforced soft actuators for trajectory matching," *Proceedings of the National Academy of Sciences*, vol. 114, no. 1, pp. 51–56, 2017. DOI: 10.1073/pnas.1615140114. eprint: http://www.pnas.org/content/114/1/51.full.pdf. [Online]. Available: http://www.pnas.org/content/114/1/51.abstract.

[140] A. Sedal, D. Bruder, J. Bishop-Moser, R. Vasudevan, and S. Kota, "A constitutive model for torsional loads on fluid-driven soft robots," in *ASME 2017 International Design Engineering Technical Conferences and Computers and Information in Engineering Conference*, American Society of Mechanical Engineers, 2017.

[141] G. Singh and G. Krishnan, "A constrained maximization formulation to analyze deformation of fiber reinforced elastomeric actuators," *Smart Materials and Structures*, vol. 26, no. 6, p. 065 024, 2017.

[142] C.-P. Chou and B. Hannaford, "Measurement and modeling of mckibben pneumatic artificial muscles," *IEEE Transactions on robotics and automation*, vol. 12, no. 1, pp. 90–102, 1996.

[143] G. Singh and G. Krishnan, "An isoperimetric formulation to predict deformation behavior of pneumatic fiber reinforced elastomeric actuators," in *2015 IEEE/RSJ International Conference on Intelligent Robots and Systems (IROS)*, Sep. 2015, pp. 1738–1743. DOI: 10.1109/IROS.2015.7353602.

[144] S. Davis and D. G. Caldwell, "Braid effects on contractile range and friction modeling in pneumatic muscle actuators," *The International Journal of Robotics Research*, vol. 25, no. 4, pp. 359–369, 2006. DOI: 10.1177/0278364906063227. eprint: http://dx.doi.org/10.1177/0278364906063227. [Online]. Available: http://dx.doi.org/10.1177/0278364906063227.

[145] M. D. Gilbertson, G. McDonald, G. Korinek, J. D. V. de Ven, and T. M. Kowalewski, "Serially actuated locomotion for soft robots in tube-like environments," *IEEE Robotics and Automation Letters*, vol. 2, no. 2, pp. 1140–1147, Apr. 2017, ISSN: 2377-3766. DOI: 10.1109/LRA.2017.2662060.

[146] T. Nakamura and H. Shinohara, "Position and force control based on mathematical models of pneumatic artificial muscles reinforced by straight glass fibers," in *Robotics and Automation, 2007 IEEE International Conference on*, IEEE, 2007, pp. 4361–4366.

[147] S. Kota, "Shape-shifting things to come," *Scientific American*, vol. 310, no. 5, pp. 58–65, 2014.

[148] M. Kamon, M. J. Tsuk, and J. K. White, "Fasthenry: A multipole-accelerated 3-d inductance extraction program," *IEEE Transactions on Microwave theory and techniques*, vol. 42, no. 9, pp. 1750–1758, 1994.

[149] E. B. Rosa, "The self and mutual inductances of linear conductors," 1908.

[150] W. Felt, *Self-inductance of smart braid fiber reinforced elastomeric enclosures*, 2017. [Online]. Available: `https://www.mathworks.com/matlabcentral/fileexchange/62507-self-inductance-of-smart-braid-fiber-reinforced-elastomeric-enclosures`.

[151] National Instruments, *Capacitance/inductance measurements*, 2011. [Online]. Available: `http://www.ni.com/tutorial/3078/en/`.

[152] ——, *Ni flexdmm measurement capabilities*, 2011. [Online]. Available: `http://www.ni.com/white-paper/3713/en/`.

[153] Oberhauser, Chris at Texas Instruments, *Ldc sensor design*, 2014. [Online]. Available: `http://www.ti.com/lit/an/snoa930/snoa930.pdf`.

[154] D. Caldwell, N. Tsagarakis, and G. Medrano-Cerda, "Bio-mimetic actuators: Polymeric pseudo muscular actuators and pneumatic muscle actuators for biological emulation," *Mechatronics*, vol. 10, no. 4, pp. 499–530, 2000.

[155] Festo, *Fluidic muscle*, 2007. [Online]. Available: `http://www.festo.com/cms/en_corp/9790.htm`.

[156] R. Niiyama, S. Nishikawa, and Y. Kuniyoshi, "Athlete robot with applied human muscle activation patterns for bipedal running," in *Humanoid Robots (Humanoids), 2010 10th IEEE-RAS International Conference on*, IEEE, 2010, pp. 498–503.

[157] X. Shen, "Nonlinear model-based control of pneumatic artificial muscle servo systems," *Control Engineering Practice*, vol. 18, no. 3, pp. 311–317, 2010.

[158] D. G. Caldwell, G. A. Medrano-Cerda, and M. Goodwin, "Control of pneumatic muscle actuators," *Control Systems, IEEE*, vol. 15, no. 1, pp. 40–48, 1995.

[159] K. E. Gordon, G. S. Sawicki, and D. P. Ferris, "Mechanical performance of artificial pneumatic muscles to power an ankle–foot orthosis," *Journal of biomechanics*, vol. 39, no. 10, pp. 1832–1841, 2006.

[160] S. Wakimoto, J. Misumi, and K. Suzumori, "New concept and fundamental experiments of a smart pneumatic artificial muscle with a conductive fiber," *Sensors and Actuators A: Physical*, vol. 250, pp. 48–54, 2016, ISSN: 0924-4247. DOI: `http://dx.doi.org/10.1016/j.sna.2016.08.004`. [Online]. Available: `//www.sciencedirect.com/science/article/pii/S092442471630379X`.

[161] Y. Shapiro, K. Gabor, and A. Wolf, "Modeling a hyperflexible planar bending actuator as an inextensible euler–bernoulli beam for use in flexible robots," *Soft Robotics*, vol. 2, no. 2, pp. 71–79, 2015.

[162] H. Schulte, "The characteristics of the mckibben artificial muscle," *The application of external power in prosthetics and orthotics*, vol. 874, pp. 94–115, 1961.

[163] M. B. Pritts and C. D. Rahn, "Design of an artificial muscle continuum robot," in *Robotics and Automation, 2004. Proceedings. ICRA '04. 2004 IEEE International Conference on*, vol. 5, Apr. 2004, 4742–4746 Vol.5. DOI: 10.1109/ROBOT.2004.1302467.

[164] A. Bartow, A. Kapadia, and I. Walker, "A novel continuum trunk robot based on contractor muscles," in *Proceedings of the 12th WSEAS International Conference on Signal Processing, Robotics, and Automation*, 2013, pp. 181–186.

[165] B. Tondu and P. Lopez, "Modeling and control of mckibben artificial muscle robot actuators," *Control Systems, IEEE*, vol. 20, no. 2, pp. 15–38, 2000.

[166] Texas Instruments, *Ldc1000 inductance-to-digital converter, compare*, 2015. [Online]. Available: http://www.ti.com/product/LDC1000/compare.

[167] S. Lambeck and C. Busch, "Exact linearization control for a pneumatic proportional pressure control valve," in *Control and Automation (ICCA), 2010 8th IEEE International Conference on*, IEEE, 2010, pp. 22–27.

[168] A. McCormack and K. Godfrey, "Rule-based autotuning based on frequency domain identification," *Control Systems Technology, IEEE Transactions on*, vol. 6, no. 1, pp. 43–61, Jan. 1998, ISSN: 1063-6536. DOI: 10.1109/87.654876.

[169] R. J. Webster and B. A. Jones, "Design and kinematic modeling of constant curvature continuum robots: A review," *The International Journal of Robotics Research*, 2010. DOI: 10.1177/0278364910368147.

[170] K. Antonelli and G. Immega, "An extensible robotic tentacle," *Industrial Robot: An International Journal*, vol. 24, no. 6, pp. 423–427, 1997. DOI: 10.1108/01439919710192545. [Online]. Available: http://dx.doi.org/10.1108/01439919710192545.

[171] G. Granosik and J. Borenstein, "Integrated joint actuator for serpentine robots," *Mechatronics, IEEE/ASME Transactions on*, vol. 10, no. 5, pp. 473–481, Oct. 2005, ISSN: 1083-4435. DOI: 10.1109/TMECH.2005.856222.

[172] I. Gaiser, R. Wiegand, O. Ivlev, A. Andres, H. Breitwieser, S. Schulz, and G. Bretthauer, "Compliant robotics and automation with flexible fluidic actuators and inflatable structures," 2012.

[173] M. Cianchetti, T. Ranzani, G. Gerboni, I. D. Falco, C. Laschi, and A. Menciassi, "Stiff-flop surgical manipulator: Mechanical design and experimental characterization of the single module," in *2013 IEEE/RSJ International Conference on Intelligent Robots and Systems*, Nov. 2013, pp. 3576–3581. DOI: 10.1109/IROS.2013.6696866.

[174] A. Marchese, K. Komorowski, C. Onal, and D. Rus, "Design and control of a soft and continuously deformable 2d robotic manipulation system," in *Robotics and Automation (ICRA), 2014 IEEE International Conference on*, May 2014, pp. 2189–2196. DOI: 10.1109/ICRA.2014.6907161.

[175] T. F. Allen, G. Hein, and K. Albert, "Constant-curvature continuum manipulator kinematics," *Under Review*,

[176] F. E. Neumann, "Allgemeine gesetze der induzierten elektrischen strme," 1845, pp. 1–87.

[177] E. Oberg, F. D. Jones, H. L. Horton, and H. H. Ryffel, *Machinery's Handbook (29th Edition) & Guide to Machinery's Handbook*. Industrial Press, 2012, p. 263, ISBN: 978-0-8311-2901-9.

[178] Texas Instruments, *Application report: using multiple sensors with ldc1000*, 2014. [Online]. Available: http://www.ti.com/lit/an/snoa924/snoa924.pdf.

[179] T. S. GmbH, *Technische spezifikationen kabelartiger formsensor*, Accessed June 2017. [Online]. Available: http://www.tst-inno.de/pdf/Technische-Spezifikationen-kabelartiger-Formsensor.pdf.

[180] F. M. Gems and Beads, *Beading wire, accu-flex, nylon and silver-plated stainless steel*, Accessed June 2017. [Online]. Available: http://www.firemountaingems.com/.

[181] B. Kasemsadeh, *Inductive sensing: Are narrow-band lc sensors immune to dc magnetic fields?* Accessed June 2017. [Online]. Available: https://e2e.ti.com/blogs_/b/analogwire/archive/2016/03/14/inductive-sensing-are-narrow-band-lc-sensors-immune-to-dc-magnetic-fields.

[182] K. Suzumori, T. Hama, and T. Kanda, "New pneumatic rubber actuators to assist colonoscope insertion," in *Robotics and Automation, 2006. ICRA 2006. Proceedings 2006 IEEE International Conference on*, May 2006, pp. 1824–1829. DOI: 10.1109/ROBOT.2006.1641971.

[183] Otherlab Orthotics. [Online]. Available: http://www.orthotics.otherlab.com/.